論文 / 著書情報
Article / Book Information

題目(和文)	ステップ乳化とDLD法の統合による液滴および粒子処理の高度化
Title(English)	Integration of step emulsification and deterministic lateral displacement for advanced droplet and particle processing
著者(和文)	季広沖
Author(English)	JI Guangchong
出典(和文)	学位:博士(工学), 学位授与機関:東京科学大学, 報告番号:甲第8号, 授与年月日:2024年12月31日, 学位の種別:課程博士, 審査員:西迫 貴志,吉田 和弘,進士 忠彦,柳田 保子,石田 忠
Citation(English)	Degree:Doctor (Engineering), Conferring organization: Institute of Science Tokyo, Report number:甲第8号, Conferred date:2024/12/31, Degree Type:Course doctor, Examiner:,,,,
学位種別(和文)	博士論文
Type(English)	Doctoral Thesis

東京科学大学

令和 **6** 年 **12** 月　博士論文

Integration of step emulsification and deterministic lateral displacement for advanced droplet and particle processing

指導教員：　西迫　貴志　准教授

工学院　機械系　機械コース

季広沖 **Guangchong JI**

20D18080

Table of Contents

Chapter 1. Introduction

Chapter 2. Separation of main and satellite droplets

Chapter 3. Post-formation fluorescent labeling of main droplets

Chapter 4. In-situ external gelation for alginate hydrogel particle synthesis

Chapter 5. Mitigation of droplet accumulation through pillar-assisted nozzle design

Chapter 6. Scalable droplet processing via module parallelization

Chapter 7. Conclusion and outlook

Appendix

Acknowledgments

Achievements

Chapter 1
Introduction

1.1 Microfluidic processing of droplets and particles

In recent years, the production of particles and droplets has become an essential process in the field of biomedical engineering, with widespread applications in controlled drug delivery, tissue engineering, biosensors, diagnostic devices, cellular analysis, and artificial cell fabrication[1]. Based on their size, these particles can be classified into nanoparticles and microparticles.

As an innovative solution, microfluidics has emerged as a powerful alternative, offering precise control over fluid manipulation[2]. This technology has shown significant advantages over traditional bulk methods, particularly in terms of producing particles with narrow size distributions, higher reproducibility, and improved encapsulation efficiency[1]. Additionally, microfluidics allows for easier scalability, making it a promising platform for industrial applications[3].

Microfluidics-based droplet and particle production has gained increasing attention due to these benefits, which include lower batch-to-batch variation and better control over particle characteristics. This approach has been widely applied in various biomedical applications, such as single-cell analysis[4], 3D cell cultures[5], and organ-on-chip systems[6]. This technique has also led to further enhancement of the production of nanoparticles and microparticles[7–9].

In this thesis, a coupling DLD with step emulsification to produce droplets and particles is proposed. Firstly, single-module systems combining step emulsifiers and DLD arrays for droplet formation and separation are demonstrated. Additionally, the production of modified particles and hydrogel particles using this integrated approach is explored. Next, to address the issue of droplet clogging, an optimized design is presented. Finally, a scalable system using parallel modules of step emulsifiers and DLD micropillar arrays for the high-throughput production of satellite-free droplets is demonstrated.

1.2 Droplet microfluidics

1.2.1 Droplets in microfluidics and application

Droplet microfluidics involves the manipulation of discrete volumes of one liquid within another immiscible phase, allowing for controlled droplet formation at the microscale. This technique has gained significant attention due to its ability to produce droplets with precise sizes and shapes, efficiently isolate samples, and enable the compartmentalization of reagents with high accuracy[8]. As previously introduced, droplet-based microfluidic methods are advantageous for generating specific droplets used in individualized transport and analysis[9]. Over the past few decades, microfluidic technology has been widely adopted, demonstrating tremendous potential across various fields, including food processing, tissue engineering, bioanalysis, and chemical detection[10].

Droplet microfluidics, with its precise manipulation of microscale particles, has unlocked numerous applications in biomedical research[11]. It enables highly specialized analysis in fields such as genomics, epigenomics, transcriptomics, proteomics, and metabolomics. Traditional cell manipulation methods focus on bulk cell populations, providing an overview of collective behavior. In contrast, droplet microfluidics allows for single-cell encapsulation, facilitating high-precision analysis of individual cells, bacteria, and viruses[4]. In 2003, a breakthrough in single-cell genomics using droplet-based emulsion PCR was introduced[12]. Since then, several time-efficient methods for droplet-based gene amplification have been developed, including droplet PCR for detecting and quantifying rare sequence variants[13], single-copy gene amplification[14], and whole-genome amplification[15].

Over the past few decades, substantial progress has been made in developing various droplet generation techniques. Microfluidic devices employing shear stress-driven methods, such as co-flow (**Fig. 1.1a**), cross-flow (**Fig. 1.1b**), and flow-focusing (**Fig. 1.1c**), as well as interfacial tension-driven step emulsification (**Fig. 1.1d**), have been extensively studied[8].

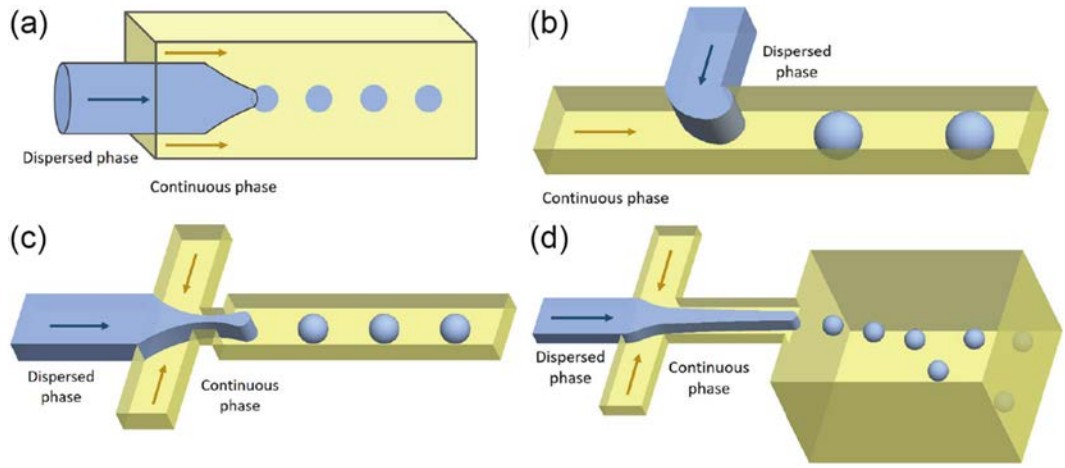

Fig. 1.1 Schematic illustrations of droplet formation using (a) co-flow, (b) cross-flow, (c) flow-focusing, and (d) step-emulsification methods.[8] (a–d) Reproduced with permission from The Royal Society of Chemistry.

1.2.2 Shear stress-driven methods for droplet processing

Co-flow droplet generation relies on the shear stress between two immiscible liquids to generate the droplets[16]. In this setup, the two liquids flow in parallel, with the dispersed phase moving through a smaller, inner pipe that is coaxially aligned within a larger outer pipe (**Fig. 1.1a**). The continuous phase flows in the space between the two pipes. Droplets form as the dispersed phase breaks up upon exiting the inner pipe.

Cross-flow droplet generation[17] shares similarities with co-flow in the shear stress between two immiscible liquids drives droplet formation. However, in this cross-flow generation, the continuous and dispersed phases meet at a junction where their respective channels intersect at a 90° angle, forming a T-junction (**Fig. 1.1b**).

In flow-focusing generation method[18], two immiscible fluid streams are focused toward the center of the channel as they pass through a constricted orifice. Typically, the dispersed phase flows through a central channel, while the continuous phase enters through two side channels at an angle (**Fig. 1.1c**). At the junction, the dispersed phase is squeezed and pinched off, forming droplets.

The effectiveness of shear stress-driven methods depends greatly on the properties of the liquids involved, such as flow rates, viscosity, and interfacial tension[8]. However, these methods

often result in the formation of satellite droplets – smaller droplets that break off from the main droplets – which are considered undesirable byproducts as they compromise the purity of the final product[19–21]. The detailed mechanisms behind satellite droplet formation will be discussed in **Chapter 2**.

1.2.3 Step emulsification

1.2.3.1 Mechanism

Step emulsification is a widely-used droplet generation technique based on interfacial tension, as opposed to shear-induced methods. In step emulsification, droplet formation is primarily influenced by the device geometry and the wetting properties of the nozzle. The device typically consists of channels with varying heights. As the dispersed phase flows through the shallow nozzle, a decrease in internal pressure occurs, leading to rapid expansion of the liquid at the tip, followed by necking and eventual droplet formation[22,23].

The detailed pinch-off process of droplets in step emulsification has been revealed[24–28]. Eggersdorfer et al. explained the breakup of droplets based on the pressure difference (ΔP) between the neck and the tongue-shaped tip of the dispersed phase (**Fig. 1.2**)[24]. The pressure difference is calculated as following:

$$\Delta P = P_n - P_t = \sigma(\kappa_n - \kappa_t) \quad (1\text{-}1)$$

where ΔP is the pressure difference, P_n is the internal pressure of the neck, P_t is the internal pressure of the tongue-shaped tip, κ_n is the curvature of the neck, and κ_t is the curvature of the tongue-shaped tip. With the increasing of the volume of the tongue-shaped tip, κ_t decreases, accompanied with the increase of ΔP, which leads to a faster transfer of the dispersed phase from the neck towards the tip. While this transfer out of the neck is faster than the supplement, the neck will shrink and finally break to form a droplet.

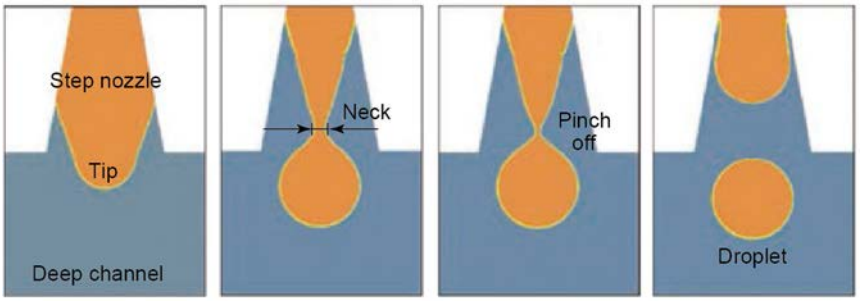

Fig. 1.2 Formation of a droplet in step emulsification[24]. Reproduced with permission from National Academy of Sciences, USA.

Previous studies have clearly pointed out the transition of two modes of droplet formation in step emulsification under the increasing flow rate of the dispersed phase[24,25]. Sugiura et al. found that below a critical flow rate, the size of the droplets was uniform (dripping), while larger droplets were formed with the flow rate over the critical value (jetting)[25]. A further analysis is demonstrated by Eggersdorfer et al.[24] Under the dripping regime of the flow rate, the amount of fluid out of the step emulsification nozzles (Q_{out}) was more than the amount into the nozzles (Q_{in}). However, with the increase of the flow rate, a balance of $Q_{in} = Q_{out}$ will be reached, leading to slower shrinkage of the neck and longer time for the pinch-off of droplets. The increase of time further caused more fluid into the tongue-shaped tip, resulting in larger droplets in jetting flow rate regime.

Since the formation of droplets in step emulsification is driven by the interfacial tension of the liquid, the size of the droplets is mainly determined by the geometry of the channel. Among the three dimensions of the microchannel, the height of the microchannel dominates the size of the droplets[26]; while the width and length of the microchannel pose minor influence on the diameter of the droplets[25]. In a subsequent study, the viscosities of the dispersed phase (η_d) and continuous phase (η_c) were proved to have minor influence on droplet size while the ratio (η_d / η_c) was sufficient high[27]. For a low ratio, the droplet would be larger, and even cannot form. In addition, the temperature was also found to have a slight effect on droplet size[28]. In each chapter of this thesis, only one type of the dispersed and continuous phases was used, and the experiment was implemented at room temperature. Thus, the influence of viscosity and temperature is negligible.

1.2.3.2 Geometries of step emulsification nozzles

Since this is a geometry-based droplet generation technique, the design of the nozzle structures in step emulsification has been extensively studied. Four main nozzle designs have been proposed: the terrace type (**Fig. 1.3a**), the through-hole type (**Fig. 1.3b**), the edge type (**Fig. 1.3c**), and the wedge type (**Fig. 1.3d**).

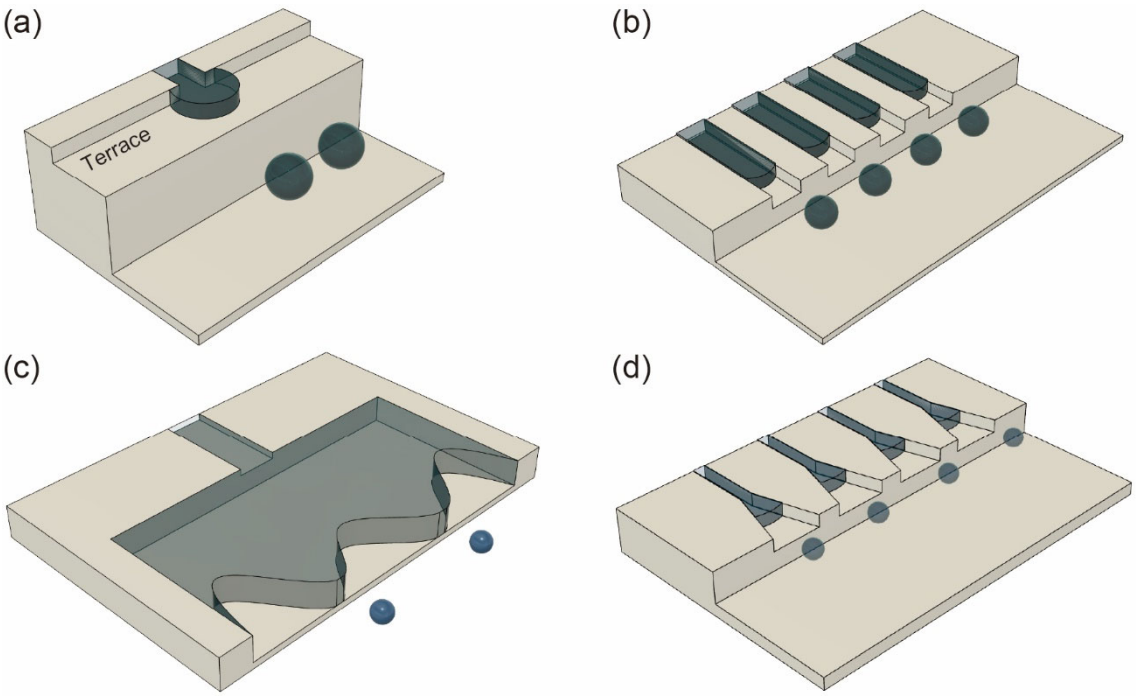

Fig. 1.3 Schematic illustrations of step emulsification devices with (a) terrace-type, (b) through-hole-type, (c) edge-type, and (d) wedge-type nozzles.

(1) Terrace-type step emulsification nozzle

The terrace-type nozzle features a terrace that has the same depth as the entrance channel of the dispersed phase and is located between the entrance channel and the deeper droplet formation channel. As the dispersed phase passes through the entrance channel and reaches the terrace, the liquid expands horizontally. When the expanding liquid reaches the edge of the terrace, three-dimensional expansion is triggered, leading to droplet formation. A step emulsification device featuring terrace-type nozzles, as proposed by Kawakatsu et al., is shown

in **Fig. 1.4a**[29].

(2) Through-hole-type step emulsification nozzle

The through-hole-type nozzle has a simpler structure, where the entrance channel directly connects to the deeper droplet formation channel. **Figure 1.4b** depicts a step emulsification device with through-hole-type nozzles[30]. Compared to the terrace-type nozzles, which have an entrance channel length of 20 μm[29], the through-hole-type nozzle eliminates the terrace but requires a longer entrance channel (~ 200 μm).

(3) Edge-type step emulsification nozzle

The edge-type step emulsification nozzle shares structural similarities with the terrace-type nozzle, featuring a wide, shallow channel connecting to a deeper channel. Unlike the terrace-type nozzle, which consists of both an entrance channel and a terrace, the edge-type nozzle only has a wide shallow channel for droplet formation. A unique feature of this design is that droplets form randomly along the edge of the wide shallow channel, allowing for the simultaneous formation of multiple droplets in a single channel. The formation of multiple droplets along the edge of a single plateau is illustrated in **Fig. 1.4c**[31].

(4) Wedge-type step emulsification nozzles

The wedge-type nozzle resembles the through-hole-type nozzle but with an increasing width at the end of the nozzle. This design leads to two-dimensional expansion of the dispersed phase at the wedge-shaped end, followed by three-dimensional expansion and subsequent droplet break-up at the nozzle edge. Previous study pointed that the ratio of the height and open width of the wedge-type nozzle must be in the range of 5.5–19 for producing monodisperse droplets[32]. A step emulsification device featuring an array of parallel wedge-shaped nozzles is shown in **Fig. 1.4d**[33].

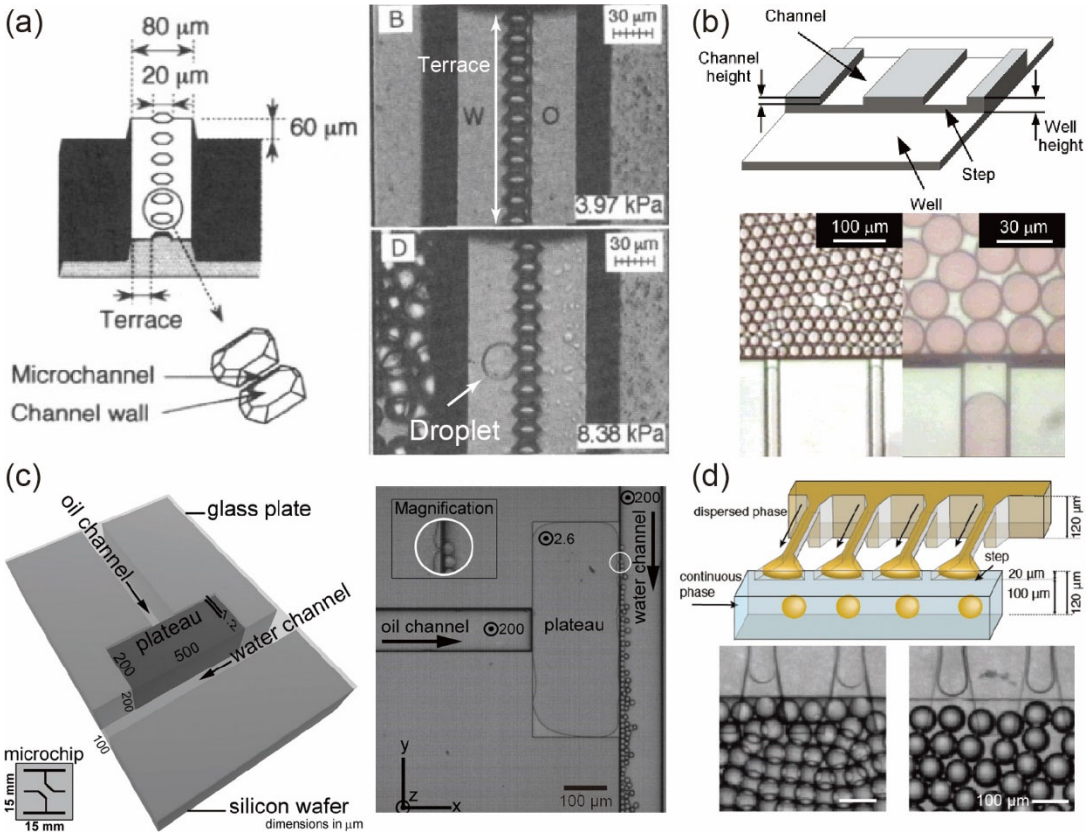

Fig. 1.4 Droplet formation via step emulsification devices with (a) terrace-type nozzles[29], (b) through-hole-type nozzles[30], (c) edge-type nozzles[31], and (d) wedge-type nozzles[33]. (a) Reproduce with permission[29]. Copyright 1997, Springer. (b) Reproduce with permission from American Chemical Society. (c) Reproduce with permission from The Royal Society of Chemistry. (d) Reproduce with permission from The Royal Society of Chemistry.

In this thesis, the wedge-type step emulsification nozzle was selected for droplet formation. However, as with shear-driven methods, step emulsification also faces challenges related to the generation of satellite droplets[24,34]. Therefore, separating satellite droplets is crucial for ensuring the purity of the final product.

1.2.3.3 Application

To date, various droplets and particles have been produced via various step emulsification devices have been reported, which include water and oil emulsions[29–33], double emulsions[35], compound-loaded droplets[36], microgel particles[37], and polymer microparticles[38]. Examples of the productions are listed in **Table 1-1**.

Table 1-1 Droplets and particles produced by step emulsification

Production	Ref.
Emulsions	29–33
Double emulsions	35
Compound loaded droplets	36
Microgels	37
Polymer microparticles	38

1.3 Deterministic lateral displacement

1.3.1 Mechanism of DLD

Deterministic lateral displacement (DLD) is a microfluidic particle separation technique first introduced in 2004[39–42]. Since its discovery, DLD has been widely applied for the size-based separation of various particles, including DNA fragments, exosomes, droplets, germs, blood cells, circulating tumor cells, and other bioparticles[40–42].

A typical DLD array consists of a microfluidic channel populated with regularly arranged micropillars. In this arrangement, each successive row of micropillars is shifted vertically by a fixed distance, forming an inclination angle with respect to the flow. This structure creates a periodic flow pattern where the fluid flowing through each gap is divided into multiple streamlines (**Fig. 1.5**)[39].

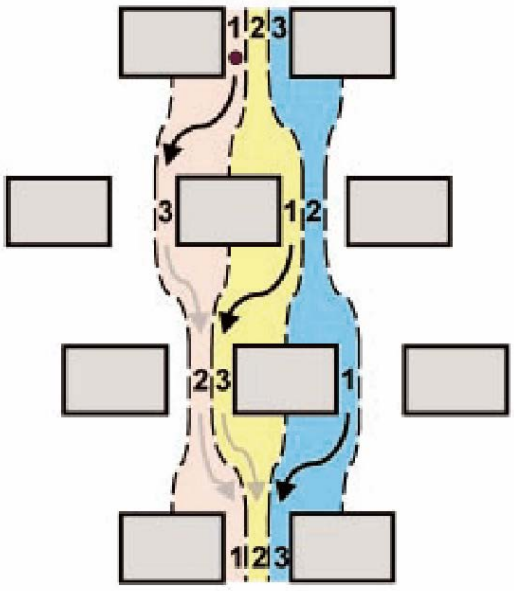

Fig. 1.5 DLD micropillars and the divided streamlines through the gaps[39]. Reproduced with permission from American Association for the Advancement of Science.

A part of an unbounded flow field with DLD micropillars is shown in **Fig. 1.6**. The direction of the flow is the y-axis, and the vertical direction is the x-axis. The flow between each gap of pillars is divided into *n* streams,

$$n = 1/\varepsilon \tag{1-2}$$

$$\varepsilon = \tan\theta \tag{1-3}$$

where θ is the shift angle of the adjacent micropillars. Each stream has equal flow flux. The space between each gap is also divided into three sections, section-1 at the up side of a pillar, section-2 at the center, and section-3 at the down side of a pillar. A stream, starting in section-1, would flow sequentially through section-3, and section-2, and finally back to section-1, the original position in the y-axis. For a particle in section-1, where the stream would flow into section-3 at next pillar, if the particle has a radius larger than the width of stream-1, it would escape from the stream and keep staying in section-1 at every pillars. This motion is called "displacement mode" (also referred to as "bump mode"). In contrast, if a particle in section-1 has a radius smaller than the width, it is dominated by the stream and flows sequentially through section-1-3-2-1. This moving is called as "zigzag mode".[39]

Based on the analysis above, the width of section-1 plays a critical role in the DLD separation. The size twice the width is called critical diameter (D_c),

$$D_c = 2\beta \tag{1-4}$$

where β is the width of section-1. For determining the value of D_c, a further analysis of the mechanism proposed by Inglis et al.[43] In the study, β is considered to be determined by the size of a gap between adjacent pillars, *G*, and the shift of pillars, ε. That is

$$D_c = 2\beta = 2\eta G\varepsilon \tag{1-5}$$

where η is a dimensionless coefficient. The flux through each gap can be expressed as

$$\int_0^{\beta} u(x)dx = \varepsilon \int_0^{G} u(x)dx \tag{1-6}$$

where $u(x)$ is the profile of the flow at the gap. For the laminar flow, by applying the parabolic profile,

$$u(x) = \left[\frac{G^2}{4} - \left(x - \frac{G}{2}\right)^2\right] \tag{1-7}$$

Solving the equation (1-6) by (1-7), ε can be expressed as

$$\varepsilon = \frac{3G\beta^2 - 2\beta^3}{G^3} \tag{1-8}$$

Thus, D_c (= 2β) can be determined by the equation above.

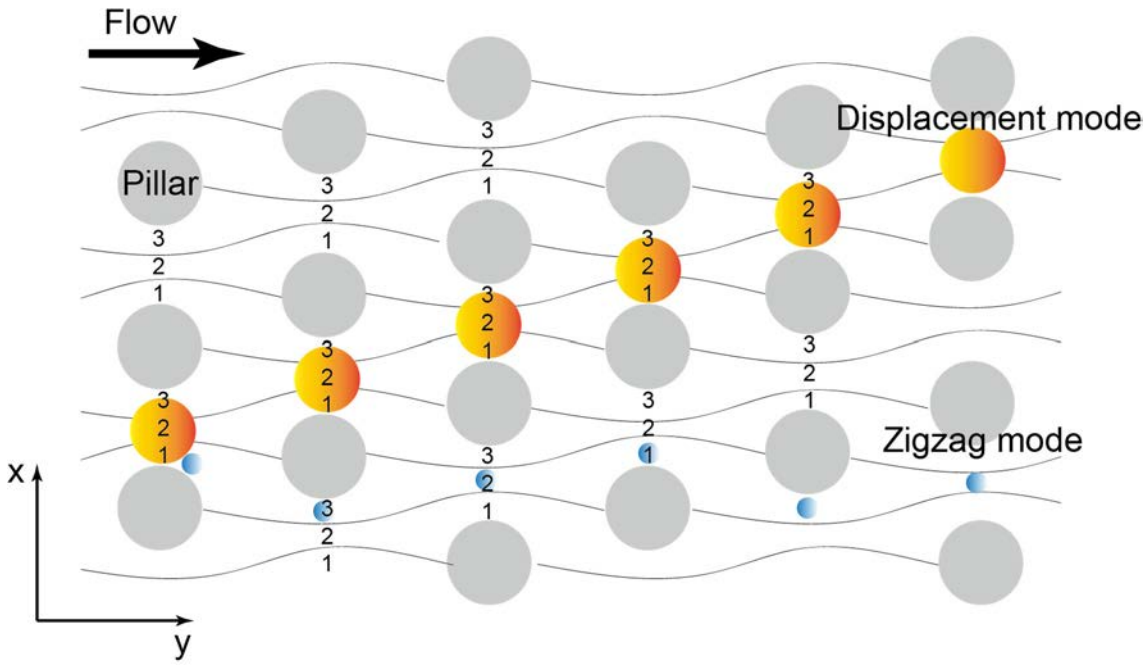

Fig. 1.6 Migration patterns of large and small particles in a DLD array.

In a following study, Davis et al. investigated particle separation in devices with varying row shift fractions and gap sizes, proposing the empirical formula to determine D_c value[44]:

$$D_c = 1.4G\varepsilon^{0.48} \tag{1-9}$$

Typically, a sharp transition in particle behavior occurs at D_c, which is a smaller value than the gap width G, making DLD suitable for high-resolution size-based separation with minimal clogging. Although Brownian motion can affect the separation of nanoparticles, microscale particles are generally unaffected. In practical applications, the number of periodic DLD arrays (referred to as the “section number”) often exceeds theoretical predictions to compensate for potential manufacturing defects, such as broken or missing pillars, without significantly affecting separation performance.

1.3.2 Boundary correction

Traditional DLD devices face efficiency challenges near the boundaries of the array due to aberrant fluid flow, which can diminish separation performance. At the microchannel boundaries, the disruption of periodic flow patterns may degrade or nullify separation effects **(Fig. 1.7a)**. Previous studies have demonstrated that effective particle separation in pressure-driven DLD devices can be maintained by using wide arrays far from any boundaries[45]. However, such designs often require complex sheath flow to prevent boundary effects, complicating the device structure. To address this, Davis et al. proposed modifying the boundary interfaces in DLD arrays to maintain a uniform flow pattern and ensure separation efficiency across the entire array (**Fig. 1.7b**)[45]. In an ideal array, the fluid flux over each post is represented by $\epsilon\Phi$, where Φ is the total fluid flux through the gap, and ϵ is the row shift fraction. To preserve this flux near the boundaries, corrections to the gap widths at the first and last rows are necessary. On the left boundary, the gap width in the *n*-th row is adjusted as:

$$g_{\mathrm{n}} = G\sqrt{n\epsilon} \tag{1-10}$$

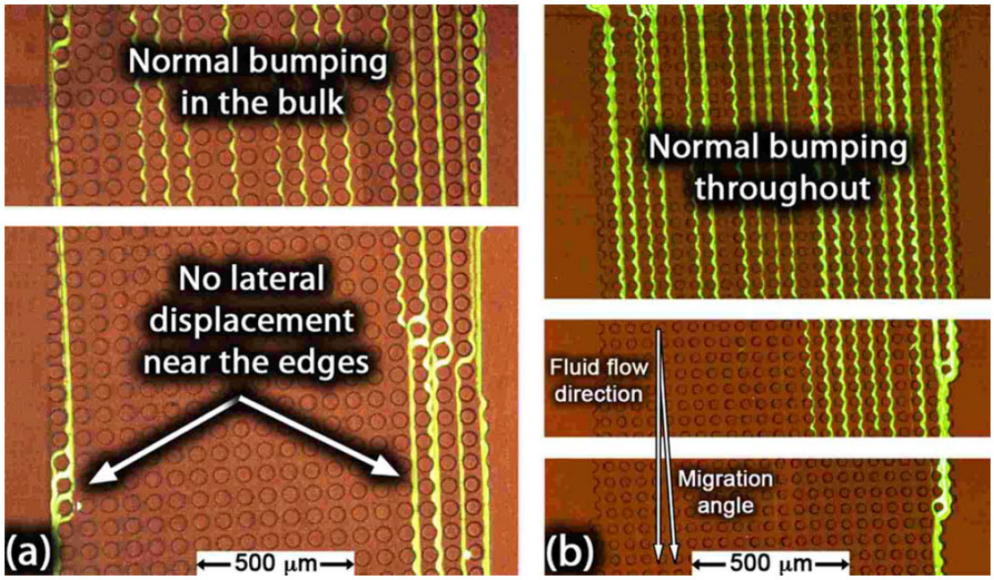

Fig. 1.7 Migration patterns of beads that are over 50% larger than the D_c in DLD arrays with (a) uncorrected and (b) corrected boundary[45]. (a) The D_c of DLD array is 6.5 μm, the diameter of beads is 10.0 μm, 56% above the D_c. (b) The D_c of DLD array is 5.8 μm, the diameter of beads is 8.4 μm, 45% above the D_c. Reproduced with permission from American Institute of Physics.

where n ranges from 1 to 1/ ϵ, and G is the standard gap width. On the right boundary, the gap width in the n-th row is corrected as

$$g_{\mathrm{n}} = G\sqrt{2 - n\epsilon} \tag{1-11}$$

The Equation (1-3) ensures that the gap is sufficiently wide to prevent particle clogging as they accumulate near the right boundary. These gap corrections preserve consistent flow patterns, allowing the finite array to perform similarly to an ideal, infinite array.

1.3.3 DLD application

To date, DLD has been applied in the separation of polymer and magnetic beads[46], droplets[47], and various bio-samples including blood cells[48], tumor cells[49], vesicles[50,51], microorganisms[52,53], and other bioparticles[54–58]. Examples of the separation are listed in **Table 1-2**.

Table 1-2 Samples separated by DLD.

Target	Ref.
Polymer and magnetic beads	46
Droplets	47
Blood cells	48
Tumor cells	49
Exosomes	50
Vesicles	51
Bacteria	52
Fungal spores	53
DNA	54
Stem cells	55
Skeletal progenitor cells	56
Cardiomyocytes	57
Microalgae	58

In addition to the DLD separators, a DLD device was proposed by Morton et al. for the lysis, labeling and washing of cells[59]. In this device, platelets with the size larger than the D_c value migrated serially across a buffer stream, a stream containing fluorescent surface-binding antigens, and a washing stream. With the migration, the platelets were treated by the antigens and rinsed in the washing stream (**Fig. 1.8a**). This device was further used for the extraction of chromosomes from bacteria. By flowing *E. coli* bacteria across a stream of lysis solution, the chromosomes and other cell contents were released. Subsequently, the chromosomes with the size larger than D_c were separated from the small-sized cell contents (**Fig. 1.8a**).

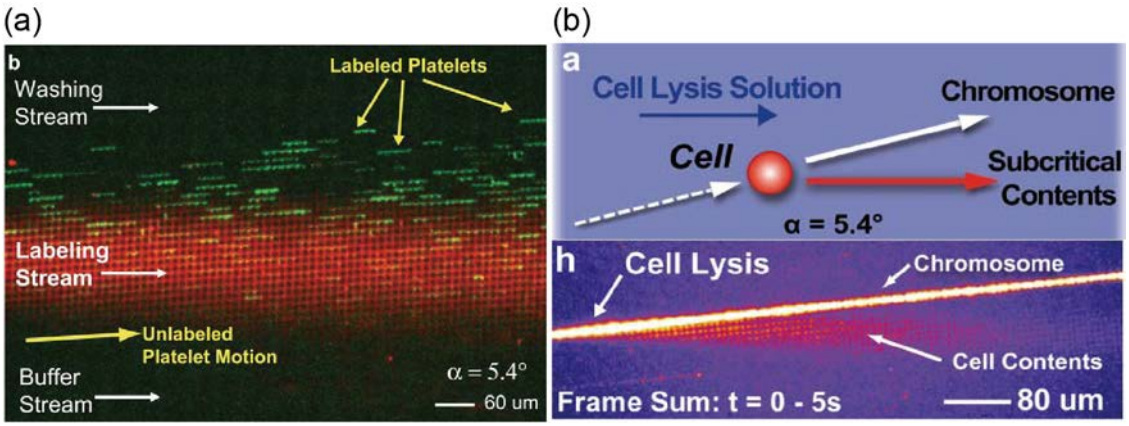

Fig. 1.8 (a) Fluorescent labeling and washing of platelets, and (b) lysis of bacteria in DLD array[59]. Reproduced with permission from The Royal Society of Chemistry.

Given the advantage of precise manipulation of the particles based on their sizes, DLD has been mostly used as separators and further as reactor for the modification of bioparticles. In this thesis, the manipulation of particles by DLD, which has never been reported, will be further used for the advanced processing of droplets and particles.

1.4 Objectives

As discussed above, deterministic lateral displacement (DLD) has been applied to produce satellite-free droplets for sheath-driven droplet-makers. However, the throughput of these systems can be improved, and the potential for coupling DLD with step emulsification, an interfacial tension-driven droplet generation technique suitable for mass production, remains unexplored.

In this thesis, the coupling of step emulsification and DLD in a single module for the production of satellite-free droplets is demonstrated for the first time (**Chapter 2**). This coupled system will then be employed to produce satellite-free, fluorescence-modified monomer droplets, which are subsequently used to generate polymeric microspheres (**Chapter 3**). Additionally, the system is applied to produce alginate hydrogel particles (**Chapter 4**). To address the issue of droplet clogging between DLD pillars, a new design featuring parallel step emulsifiers and a DLD micropillar array is introduced (**Chapter 5**). Finally, a scaled-up system with 10 modules of coupled step emulsification and DLD is presented to achieve higher throughput of satellite-free droplets (**Chapter 6**).

1.5 Outline of thesis

Chapter 1. Introduction

Provides an overview of prior research on microfluidic step emulsification and droplet separation using DLD devices and introduces the context for this study.

Chapter 2. Separation of main and satellite droplets

Demonstrates the coupling of step emulsification and DLD for droplet formation, along with the separation performance of droplets within the DLD micropillar array.

Chapter 3. Post-formation fluorescent labeling of main droplets

Explores the formation of droplets containing fluorescent nanoparticles within the water phase and their migration through the nanoparticle flow. The fluorescence properties of the satellite-free polymeric microspheres, produced via off-chip photopolymerization, are characterized.

Chapter 4. In-situ external gelation for alginate hydrogel particle synthesis

Describes the formation of Na-alginate droplets at the step emulsification nozzles. The migration of these droplets through the DLD array and their subsequent gelation via $CaCl_2$ emulsion flow are investigated, with an evaluation of the resulting Ca-alginate hydrogel particles.

Chapter 5. Mitigation of droplet accumulation through pillar-assisted nozzle design

Introduces a new design with parallel step emulsification nozzles and DLD micropillars. The formation of droplets at the nozzles and their migration through the DLD array are described to address clogging issues.

Chapter 6. Scalable droplet processing via module parallelization

Demonstrates a scaled-up device featuring 10 parallel modules coupling step emulsification and DLD. The liquid distribution through the inlet chamber and its effect on the 10 modules is evaluated via CFD simulation and experimental results. Droplet formation and migration

through the DLD array are presented.

Chapter 7. Conclusion and outlook

Summarizes the key findings of the thesis and discusses future directions for research.

The connection between these chapters is shown in **Fig. 1.8**.

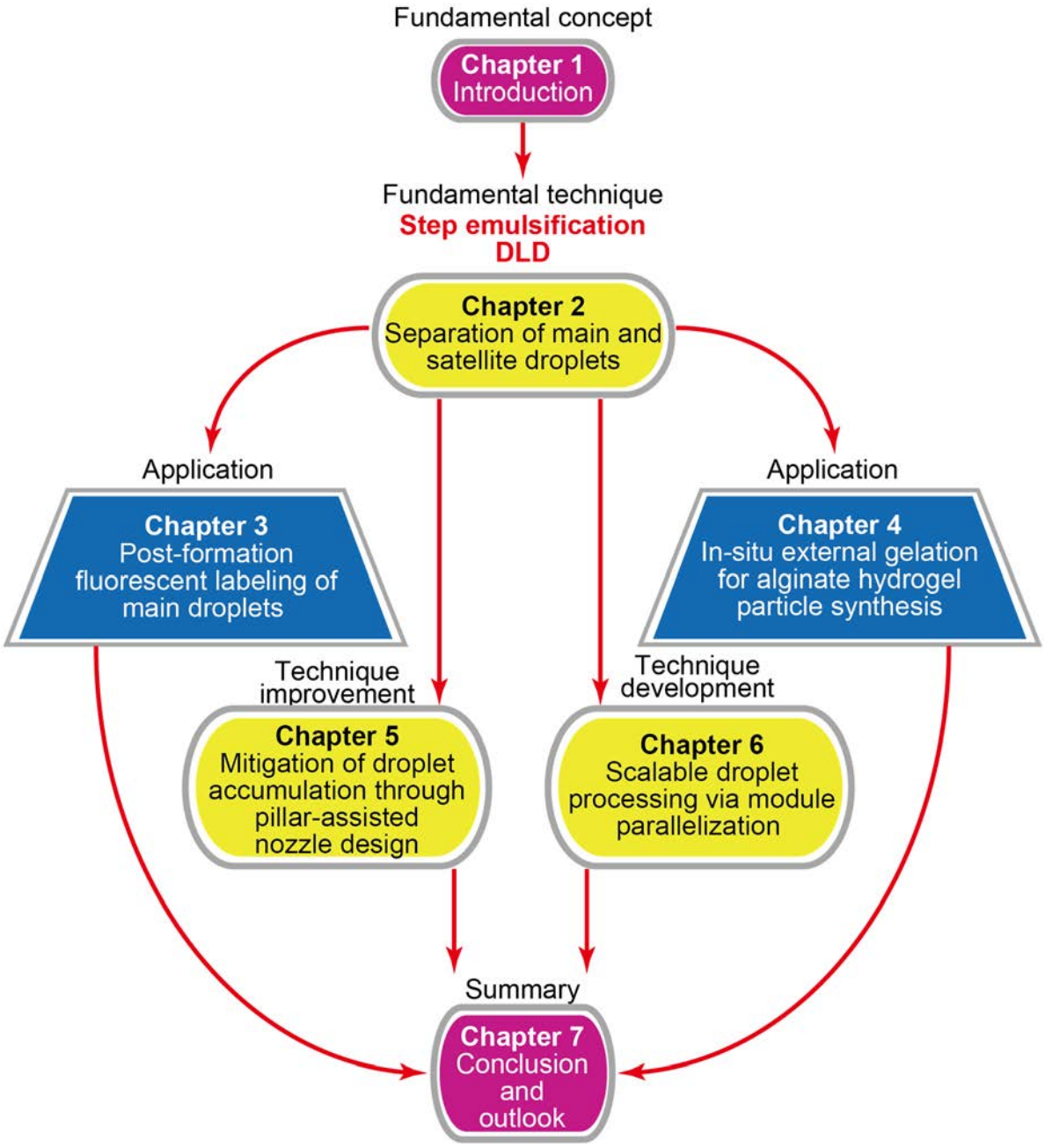

Fig. 1.8 Connection between the chapters of the thesis.

References

[1] W. Zheng, R. Xie, X. Liang, Q. Liang. Fabrication of biomaterials and biostructures based on microfluidic manipulation. *Small*, **2022**, 18, 2105867.

[2] Z. Liu, F. Fontana, A. Python, J. T. Hirvonen, H. A. Santos. Microfluidics for production of particles: mechanism, methodology, and applications. *Small*, **2020**, 16, 1904673.

[3] S. Neethirajan, I. Kobayashi, M. Nakajima, D. Wu, S. Nandagopal, F. Lin. Microfluidics for food, agriculture and biosystems industries. *Lab Chip*, **2011**, 11, 1574–1586.

[4] K. Matuła, F. Rivello, W. T. Huck. Single-cell analysis using droplet microfluidics. *Adv. Biosyst.*, **2020**, 4, 1900188.

[5] V. Van Duinen, S. J. Trietsch, J. Joore, P. Vulto, T. Hankemeier. Microfluidic 3D cell culture: from tools to tissue models. *Curr. Opin. Biotechnol.*, **2015**, 35, 118–126.

[6] S. N. Bhatia, D. E. Ingber. Microfluidic organs-on-chips. *Nat. Biotechnol.*, **2014**, 32, 760–772.

[7] J. Wang, Y. Li, X. Wang, J. Wang, H. Tian, P. Zhao, Y. Tian, Y. Gu, L. Wang, C. Wang. Droplet microfluidics for the production of microparticles and nanoparticles. *Micromachines*, **2017**, 8, 22.

[8] L. Nan, H. Zhang, D. A. Weitz, H. C. Shum. Development and future of droplet microfluidics *Lab Chip*, **2024**, 24, 1135–1153.

[9] S. Y. Teh, R. Lin, L. H. Hung, A. P. Lee. Droplet microfluidics. *Lab Chip*, **2008**, 8, 198–220.

[10] T. S. Kaminski, O. Scheler, P. Garstecki. Droplet microfluidics for microbiology: techniques, applications and challenges. *Lab Chip*, **2016**, 16, 2168–2187.

[11] Z. Chen, S. Kheiri, E. W. Young, E. Kumacheva. Trends in droplet microfluidics: From droplet generation to biomedical applications. *Langmuir*, **2022**, 38, 6233–6248.

[12] M. Nakano, J. Komatsu, S. I. Matsuura, K. Takashima, S. Katsura, A. Mizuno. Single-molecule PCR using water-in-oil emulsion. *J. Biotechnol.*, **2003**, 102, 117–124.

[13] Z. Zhu, W. Zhang, X. Leng, M. Zhang, Z. Guan, J. Lu, C. J. Yang. Highly sensitive and quantitative detection of rare pathogens through agarose droplet microfluidic emulsion

PCR at the single-cell level. *Lab Chip*, **2012**, 12, 3907–3913.

[14] X. Leng, W. Zhang, C. Wang, L. Cui, C. J. Yang. Agarose droplet microfluidics for highly parallel and efficient single molecule emulsion PCR. *Lab Chip*, **2010**, 10, 2841–2843.

[15] M. Hosokawa, Y. Nishikawa, M. Kogawa, H. Takeyama. Massively parallel whole genome amplification for single-cell sequencing using droplet microfluidics. *Sci. Rep.*, **2017**, 7, 5199.

[16] P. B. Umbanhowar, V. Prasad, D. A. Weitz. Monodisperse emulsion generation via drop break off in a coflowing stream. *Langmuir*, **2000**, 16, 347–351.

[17] T. Thorsen, R. W. Roberts, F. H. Arnold, S. R. Quake. Dynamic pattern formation in a vesicle-generating microfluidic device. *Phys. Rev. Lett.*, **2001**, 86, 4163.

[18] Y. Liu, N. Tottori, T. Nisisako. Microfluidic synthesis of highly spherical calcium alginate hydrogels based on external gelation using an emulsion reactant. *Sens. Actuators B: Chem.*, **2019**, 283, 802–809.

[19] V. Cristini, T. C. Tan. Theory and numerical simulation of droplet dynamics in complex flows—a review. *Lab Chip*, **2004**, 4, 257–264.

[20] Y. Zhang, G. Hu, Y. Liu, J. Wang, G. Yang, D. Li. Suppression and utilization of satellite droplets for inkjet printing: a review. *Processes*, **2022**, 10, 932.

[21] X. Sun, C. Zhu, T. Fu, Y. Ma, H. Z. Li. Dynamics of droplet breakup and formation of satellite droplets in a microfluidic T-junction. *Chem. Eng. Sci.*, **2018**, 188, 158–169.

[22] Z. Shi, X. Lai, C. Sun, X. Zhang, L. Zhang, Z. Pu, D. Li. Step emulsification in microfluidic droplet generation: mechanisms and structures. *Chem. Comm.*, **2020**, 56, 9056–9066.

[23] Z. Liu, C. Duan, S. Jiang, C. Zhu, Y. Ma, T. Fu. Microfluidic step emulsification techniques based on spontaneous transformation mechanism: A review. *J. Ind. and Eng. Chem.*, **2020**, 92, 18–40.

[24] M. L. Eggersdorfer, H. Seybold, A. Ofner, D. A. Weitz, A. R. Studart. Wetting controls of droplet formation in step emulsification. *Proc. Natl. Acad. Sci. USA.*, **2018**, 115, 9479–9484.

[25] S. Sugiura, M. Nakajima, M. Seki. Effect of channel structure on microchannel emulsification. *Langmuir*, **2002**, 18, 5708–5712.

[26] T. Kawakatsu, G. Trägårdh, Y. Kikuchi, M. Nakajima, H. Komori, T. Yonemoto. Effect of microchannel structure on droplet size during crossflow microchannel emulsification. *J. Surfactants and Deterg.*, **2000**, 3, 295–302.

[27] K. van Dijke, I. Kobayashi, K. Schroën, K. Uemura, M. Nakajima, R. Boom. Effect of viscosities of dispersed and continuous phases in microchannel oil-in-water emulsification. *Microfluid. Nanofluidics*, **2010**, 9, 77–85.

[28] K. Butron Fujiu, I. Kobayashi, K. Uemura, M. Nakajima. Temperature effect on microchannel oil-in-water emulsification. *Microfluid. Nanofluidics*, **2011**, 10, 773-783.

[29] T. Kawakatsu, Y. Kikuchi, M. Nakajima. Regular-sized cell creation in microchannel emulsification by visual microprocessing method. *J. Am. Oil Chem. Soc.*, **1997**,74, 317–321.

[30] I. Kobayashi, K. Uemura, M. Nakajima. Controlled generation of monodisperse discoid droplets using microchannel arrays. *Langmuir*, **2006**, 22, 10893–10897.

[31] K. van Dijke, R. de Ruiter, K. Schroën, R. Boom. The mechanism of droplet formation in microfluidic EDGE systems. *Soft Matt.*, **2010**, 6, 321–330.

[32] E. Amstad, M. Chemama, M. Eggersdorfer, L. R. Arriaga, M. P. Brenner, D. A. Weitz. Robust scalable high throughput production of monodisperse drops. *Lab Chip*, **2016**, 16, 4163–4172.

[33] A. Ofner, D. G. Moore, P. A. Rühs, P. Schwendimann, M. Eggersdorfer, E. Amstad, D. A. Weitz, A. R. Studart. High-throughput step emulsification for the production of functional materials using a glass microfluidic device. *Macromol. Chem. Phys.*, **2017**, 218, 1600472.

[34] X. Liu, S. Jiang, C. Zhu, Y. Ma, T. Fu. Formation of viscoelastic droplets in a step-emulsification microdevice. *AIChE J.*, **2022**, 68, e17780.

[35] S. Souilem, I. Kobayashi, M. A. Neves, S. Sayadi, S. Ichikawa, M. Nakajima. Preparation of monodisperse food-grade oleuropein-loaded W/O/W emulsions using microchannel emulsification and evaluation of their storage stability. *Food Bioprocess Technol.*, **2014**, 7, 2014–2027.

[36] M. A. Neves, H. S. Ribeiro, K. B. Fujiu, I. Kobayashi, M. Nakajima. Formulation of controlled size PUFA-loaded oil-in-water emulsions by microchannel emulsification using β-carotene-rich palm oil. *Ind. Eng. Chem. Res.*, **2008**, 47, 6405–6411.

[37] A. M. Chuah, T. Kuroiwa, I. Kobayashi, X. Zhang, M. Nakajima. Preparation of uniformly sized alginate microspheres using the novel combined methods of microchannel emulsification and external gelation. *Colloids Surf. A: Physicochem. Eng. Asp.*, **2009**, 351, 9–17.

[38] S. Sugiura, M. Nakajima, H. Itou, M. Seki. Synthesis of polymeric microspheres with narrow size distributions employing microchannel emulsification. *Macromol. Rapid Commun.*, **2001**, 22, 773–778.

[39] L. R. Huang, E. C. Cox, R. H. Austin, J. C. Sturm. Continuous particle separation through deterministic lateral displacement. *Science*, **2004**, 304, 987–990.

[40] J. McGrath, M. Jimenez, H. Bridle. Deterministic lateral displacement for particle separation: a review. *Lab Chip*, **2014**, 14, 4139–4158.

[41] T. Salafi, Y. Zhang, Y. Zhang. A review on deterministic lateral displacement for particle separation and detection. *Nano-Micro Lett.*, **2019**, 11, 1–33.

[42] A. Hochstetter, R. Vernekar, R. H. Austin, H. Becker, J. P. Beech, D. A. Fedosov, G. Gommper, S. Kim, J. T. Smith, G. Stolovitzky, J. O. Tegenfeldt, B. H. Wunsch, K. K. Zeming, T. Krüge, D. W. Inglis. Deterministic lateral displacement: Challenges and perspectives. *ACS Nano*, **2020**, 14, 10784–10795.

[43] D. W. Inglis, J. A. Davis, R. H. Austin, J. C. Sturm. Critical particle size for fractionation by deterministic lateral displacement. *Lab Chip*, **2006**, 6, 655–658.

[44] J. A. Davis. Microfluidic separation of blood components through deterministic lateral displacement. PhD thesis, Princeton University, USA, September, **2008**.

[45] D. W. Inglis. Efficient microfluidic particle separation arrays. *Appl. Phys. Lett.*, **2009**, 94, 013510.

[46] H. Zhang, J. Zeng, D. Han, J. Deng, N. Hu, X. Zheng, J. Yang. Deterministic lateral displacement-based separation of magnetic beads and its applications of antibody recognition. *Sensors*, **2020**, 20, 2846.

[47] N. Tottori, T. Nisisako. High-throughput production of satellite-free droplets through a parallelized microfluidic deterministic lateral displacement device. *Sen. Actuators B: Chemical*, **2018**, 260, 918–926.

[48] D. Holmes, G. Whyte, J. Bailey, N. Vergara-Irigaray, A. Ekpenyong, J. Guck, T. Duke.

Separation of blood cells with differing deformability using deterministic lateral displacement. *Interface focus*, **2014**, 4, 20140011.

[49] Z. Liu, Y. Huang, W. Liang, J. Bai, H. Feng, Z. Fang, G. Tian, Y. Zhu, H. Zhang, Y. Wang, A. Liu, Y. Chen. Cascaded filter deterministic lateral displacement microchips for isolation and molecular analysis of circulating tumor cells and fusion cells. *Lab Chip*, **2021**, 21, 2881–2891.

[50] D. Wang, Y. Yang, N. Wang, H. Guo, S. Feng, Y. Luo, J. Zhao. A Novel Microfluidic Strategy for Efficient Exosome Separation via Thermally Oxidized Non-Uniform Deterministic Lateral Displacement (DLD) Arrays and Dielectrophoresis (DEP) Synergy. *Biosensors*, **2024**, 14, 174.

[51] A. J. Laki, L. Botzheim, K. Iván, T. Szabó, V. Tamási, E. Buzás, P. Civera. Microvesicle fractionation using deterministic lateral displacement effect. International Conference on Nano/Micro Engineered and Molecular Systems (NEMS), **2014**, April, 490–493.

[52] E. Pariset, C. Parent, Y. Fouillet, B. François, N. Verplanck, F. Revol-Cavalier, A. Thuaire, V. Agache. Separation of biological particles in a modular platform of cascaded deterministic lateral displacement modules. *Sci. Rep.*, **2018**, 8, 17762.

[53] D. W. Inglis, N. Herman, G. Vesey. Highly accurate deterministic lateral displacement device and its application to purification of fungal spores. *Biomicrofluidics*, **2010**, 4, 024109.

[54] L. Nan, H. Zhang, D. A. Weitz, H. C. Shum. Development and future of droplet microfluidics *Lab Chip* **2024**, 24, 1135–1153.

[55] N. T. K. Zen, K. K. Zeming, K. L. Teo, M. Loberas, J. Lee, C. R. Goh, D. H. Yang, S. Oh, J. H. H. Po, S. M. Cool, H. W. Hou, J. Han. Scalable mesenchymal stem cell enrichment from bone marrow aspirate using deterministic lateral displacement (DLD) microfluidic sorting. *Lab Chip*, **2023**, 23, 4313–4323.

[56] M. Xavier, S. H. Holm, J. P. Beech, D. Spencer, J. O. Tegenfeldt, R. O. Oreffo, H. Morgan. Label-free enrichment of primary human skeletal progenitor cells using deterministic lateral displacement. *Lab Chip*, **2019**, 19, 513–523.

[57] B. Zhang, J. V. Green, S. K. Murthy, M. Radisic. Label-free enrichment of functional cardiomyocytes using microfluidic deterministic lateral flow displacement. *PloS One*,

2012, 7, e37619.

[58] L. Wang, G. Qian, K. Wang, Z. Wu, H. Yan, L. Shi, T. Zhou. High-throughput microalgae sorting based on the deterministic lateral displacement technique. *J. Chromatogr. A*, **2024**, 1730, 465126.

[59] K. J. Morton, K. Loutherback, D. W. Inglis, O. K. Tsui, J. C. Sturm, S. Y. Chou, R. H. Austin. Crossing microfluidic streamlines to lyse, label and wash cells. *Lab Chip*, **2008**, 8, 1448–1453.

Chapter 2

Separation of main and satellite droplets

2.1 Introduction

2.1.1 Satellite droplets

In droplet formation, the satellite droplets, which have a much smaller volume forming between the liquid drop and the liquid resource, are common undesired byproducts[1–4]. Breaking-off of a water droplet falling from a pipette is shown in **Fig. 2.1a**. The neck between the drop and the liquid resource exhibits a slender shape, whose end near the drop is steep, while the end near the liquid is flat. Then, with the recoiling of the neck, the end near the drop breaks off. Immediately after that, the end near the liquid resource becomes sharp and also breaks off. Thus, satellite droplets are formed[3]. The formation of satellite droplets is also confirmed in the microfluidic droplet formation. The formation process of droplets in the T-junction is taken as an example. In the rupturing process of the neck between the growing droplets and the liquid resource, the last stage of droplet formation driven by the capillary force, the thinnest part of the neck transfers from the center to the two ends, where the rupturing occurs. As a result, the liquid between the two rupturing points detaches both the new droplet and the liquid resource, which leads to the formation of satellite droplets (**Fig. 2.1b**)[4].

In step emulsification, similar to shear stress-driven methods, the neck just before breaking is also influenced by the Plateau–Rayleigh instability[5]. Although this instability can result in the formation of satellite droplets in step emulsification, it has been rarely addressed in the literature.

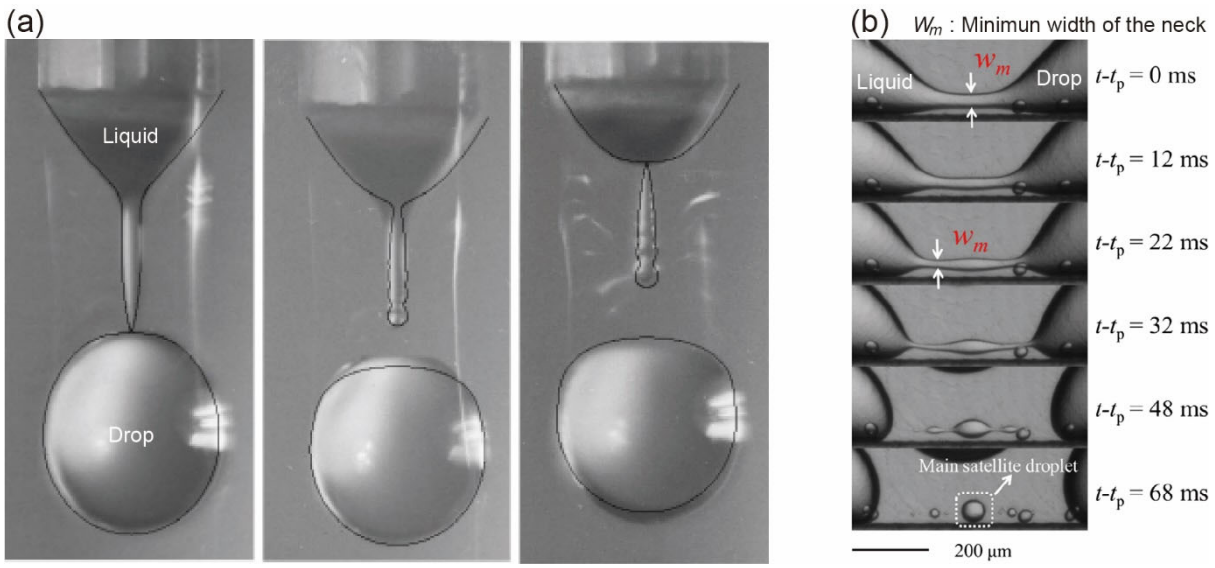

Fig. 2.1 (a) A sequence of the formation of droplets from a pipette[3]. (b)Time sequences of the rupturing process of a droplet formation in a T-junction[4]. The thinnest part of the neck transferred from the center to the ends, where the rupturing occurred and led to the formation of satellite droplets. (a) Reproduced with permission from Wiley-VCH Verlag. (b) Reproduced with permission from Elsevier.

2.1.2 Separation of satellite droplets

To date, the continuous separation of the main and satellite droplets has been reported in several studies. For instance, bifurcation geometries have been connected after T-shaped (**Fig. 2.2a**)[6,7] or flow-focusing[8] droplet generators to separate the main and satellite droplets. However, in these systems, the main and satellite droplets must be dominated by separate streamlines towards different collection channels or outlets. And while the droplets are mixed within a confined channel, the separation will become challenging. On the other hand, deterministic lateral displacement (DLD) methods[9–12], known for high-resolution size-based separation, have been integrated with shear stress-driven droplet generation to sort main and satellite droplets. Tottori et al. were the first to use a flow-focusing droplet generator combined with a single DLD region to separate ~61 μm main droplets from 1–30 μm satellite droplets (**Fig. 2.2b**)[13]. They later demonstrated the sorting of satellite droplets of different sizes using a device with multiple DLD regions. Furthermore, in another study, a single chip having eight parallel modules to produce satellite-free droplets was shown to enhance throughput (**Fig.**

2.2b)[14]. However, the application of DLD for satellite-free step emulsification has not been investigated so far.

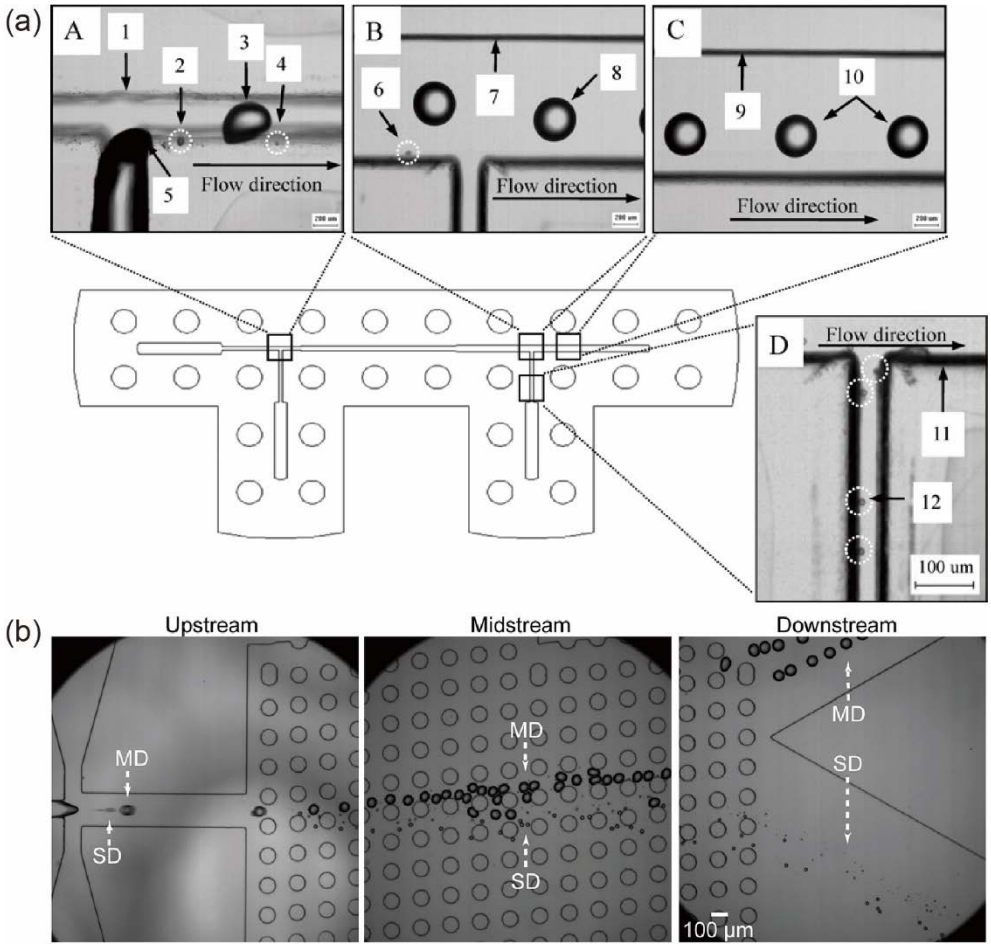

Fig. 2.2 (a) Separation of the satellite droplets from a T-junction via a branch channel in the downstream region[7]. The satellite droplets are denoted by the dashed white circles. (b) Separation of the main droplets (MD) and the satellite droplets (SD) via a DLD array[13]. (a) Reproduced with permission from The Royal Society of Chemistry. (b) Reproduced with permission from The Royal Society of Chemistry.

2.1.3 Objective

This chapter presents a microfluidic method that integrates step emulsification with DLD separation for the advanced processing of monodisperse, satellite-free droplets and particles. The device used in this study comprises 60 step-emulsification nozzles and a DLD micropillar array. The step-emulsification nozzles are positioned along the sidewall in the upstream region of the main channel, while the DLD array, consisting of periodically arranged micropillars, is

located downstream. The study begins by analyzing the break-off process at the nozzle exits, focusing on the formation of satellite droplets. It then examines the migration of both the main and satellite droplets through the DLD array, explaining how their distinct sizes cause them to follow different trajectories. Lastly, the chapter details the photopolymerization process used to transform the sorted main droplets into monodisperse polymeric microspheres.

2.1.4 Outline of this chapter

Section 2.1 Introduction

Provides an overview of previous studies on droplet generation, applications, step emulsification, and the DLD-based separation of satellite-free droplets.

Section 2.2 Materials and methods

Describes the microfluidic devices used, their fabrication, and the peripheral equipment employed in this chapter.

Section 2.3 Results and discussion

Presents the findings on droplet generation, separation, and photopolymerization of the main droplets. Additionally, the influence of flow rates of both the dispersed and continuous phases on droplet generation and separation is analyzed.

Section 2.4 Conclusion

Summarizes the key conclusions of the chapter.

2.2 Materials and methods

2.2.1 Device design and mechanism

A microfluidic device was designed that integrates step-emulsification nozzles with DLD micropillar arrays, as illustrated in **Fig. 2.3a**. The device features a symmetric layout on both sides of a central wall. In the upstream region, inlets for the water and oil liquids are located. Downstream of these inlets, 30 step-emulsification nozzles in two arrays (totaling 60 nozzles) perpendicular to the main channel are arranged. In the downstream region, a periodic array of DLD micropillars is positioned within the main channel, leading to two outlets for the separate collection of main and satellite droplets. For comparison, a device without pillars was also fabricated (**Fig. 2.3a**).

The step-emulsification nozzles are 1.3 mm in length and 16 μm in depth. They are arranged parallel to each other with a pitch of 240 μm, connecting the side channels to the main channel, which has a depth of 91 μm (**Fig. 2.3b**, **2.3c**). The nozzles with a triangular end open towards the main channel. To fully arraying the nozzles, the open angle was designed to be 9.8°, which was similar as the optimized value in previous study[15]. The nozzle width expands from 35 μm to 124 μm, resulting in the ratio of open width and height of 7.75, meeting the required value of 5.5–19 for producing monodisperse droplets. The nozzle length was designed to be 258 μm. (**Fig. 2.3d**).

Immediately following the main channel with the arrayed nozzles is the region containing the periodically arrayed DLD micropillars. This DLD array contains a rhombic unit cell where each pillar has a diameter of 100 μm and is separated from adjacent pillars by a gap of 80 μm, resulting in a pitch of 180 μm between adjacent pillars (**Fig. 2.3e**). The lateral shift between adjacent columns is 18 μm. The width of the gaps close to the DLD boundary were modified by the method introduced in **1.3.2**, **Chapter 1**[16]. The gap sizes along the wall with nozzles were modified as

$$G_{\mathrm{ns}} = G\sqrt{n\epsilon} = 80 \times \sqrt{0.1n} \tag{2-1}$$

And the gap sizes along the wall without nozzles were modified as

$$G_{\mathrm{nl}} = G\sqrt{2 - n\epsilon} = 80 \times \sqrt{2 - 0.1n} \tag{2-2}$$

where n is the number of the gap, which is 1–10 from the upstream to the downstream region; G_{ns} and G_{nl} are the gap size of n-th gap; G is the gap size of the DLD array, which is 80 μm; ε is the ratio of pillar shift. The modified gap sizes are shown in **Table 2-1**.

Table 2-1 Sizes of the gaps close to DLD boundary.

Gap #	G_{ns} (μm)	G_{nl} (μm)	Gap #	G_{ns} (μm)	G_{nl} (μm)
1	25	110	6	62	95
2	36	107	7	67	91
3	44	104	8	72	88
4	51	101	9	76	84
5	57	98	10	80	80

The height of the DLD pillars, which has minor effect on the separation performance, was designed to have a similar value of the pillar diameter (91 μm) for an easy fabrication of the PDMS chip. Each DLD region comprises 10 columns and 17 row gaps (**Fig. 2.3f**). This DLD region is repeated 28 times along the flow direction towards the outlets, guiding the main droplets across pillar arrays towards the central wall.

The critical diameter D_c, representing the cut-off value for particle separation in DLD, was estimated using the empirical formula[10,17]:

$$D_c = 1.4 \times G \times (\Delta\lambda/\lambda)^{0.48} \quad (2\text{-}3)$$

where G is the gap between the pillars (80 μm), λ is the lateral pitch between the pillars (180 μm), and $\Delta\lambda$ is the lateral shift between the pillars (18 μm). Accordingly, the D_c of our device was designed to be approximately 37 μm. Scanning electron microscopy (SEM) images of the PDMS chip showing the step-emulsification nozzles and DLD pillars are presented in **Figs. 2.3g** and **2.3h**.

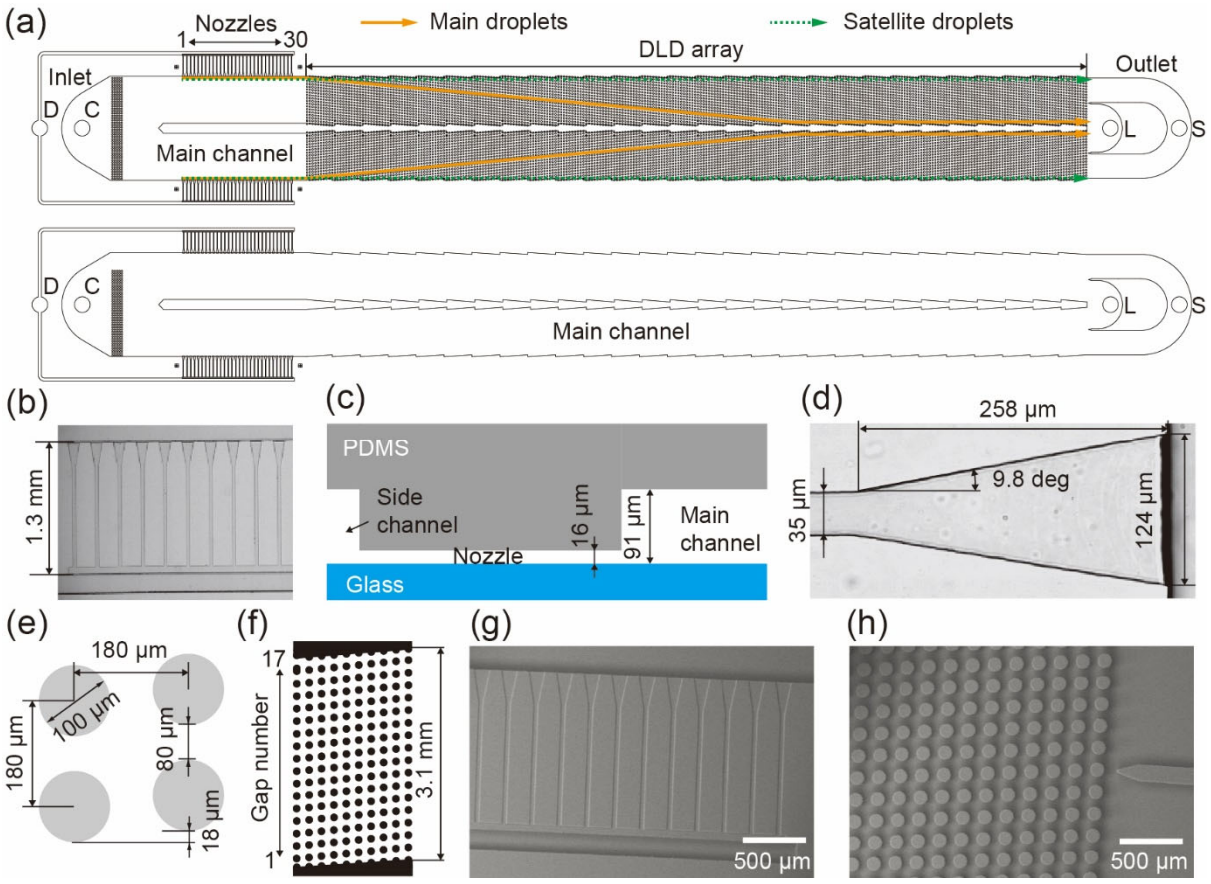

Fig. 2.3 A device integrating step emulsification nozzles and deterministic lateral displacement (DLD) pillars to sort main and satellite droplets. (a) Schematic top view of the device: (top) with DLD pillars and (bottom) without DLD pillars for comparison. (b) Photomicrograph of the arrayed nozzles. (c) Schematic cross-sectional view of a nozzle connecting the side channel to the main channel. (d) Photomicrograph of the triangular end of a nozzle. (e) Diagram of a rhombic unit cell of the DLD pillar array. (f) Illustration of a single DLD region comprising 10 columns of pillars. (g, h) SEM images of the (g) nozzles and (h) DLD pillars.

The dispersed and continuous phases are introduced separately through two inlets. The dispersed phase flows through side channels, each 200 μm wide, filling the arrayed nozzles. At the nozzle tips, monodisperse main droplets are generated in the dripping regime, accompanied by satellite droplets when the flow rates of both phases are appropriately controlled. The droplets subsequently flow along the sidewalls of the main channel and enter the downstream DLD section. Main droplets (diameter > D_c) are expected to flow laterally across the micropillar arrays at the shift angle, following the displacement mode. In contrast, satellite

droplets, smaller than D_c, are expected to follow the laminar flow without lateral displacement, moving in the zigzag mode (**Fig. 2.3a**).

2.2.2 Device fabrication

The PDMS devices were fabricated using standard soft lithography techniques[13], as illustrated in **Fig. 2.4**. The fabrication involved a two-step process for creating SU-8 molds. These molds were used to replicate both the step-emulsification nozzles (**Fig. 2.4a**) and the DLD pillars (**Fig. 2.4b**). Once the molds were completed, PDMS was poured over them to form the microfluidic chip, which was then bonded to a glass slide (**Fig. 2.4c**). After sealing, a water-soluble polymer agent (0.5 mL; SPRA-202, Tokyo Ohka Kogyo, Kanagawa, Japan) was introduced into the PDMS chip to modify its surface, making it hydrophilic. This modification reduced the contact angle of the PDMS surface from approximately 110.9° to around 3.2°, as shown in, **Figs. 2.5a** and **2.5b**. The details of the fabrication are shown in **Appendix A.1**.

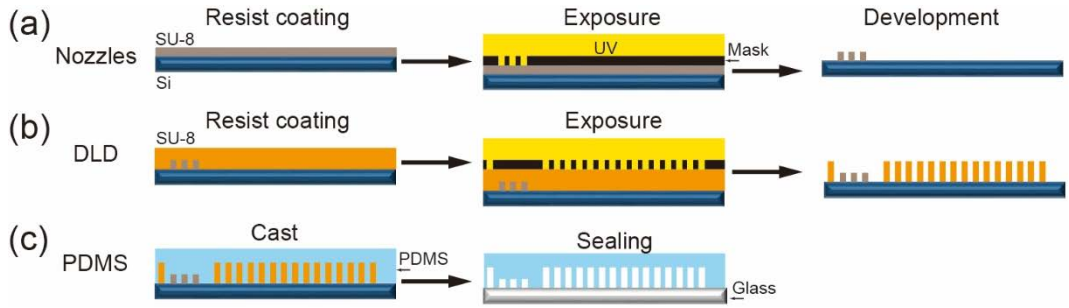

Fig. 2.4 Fabrication steps of the PDMS device using soft lithography. (a) Mold fabrication for the step emulsification section. (b) Mold fabrication for the DLD section. (c) Casting and bonding of the PDMS chip to a glass slide.

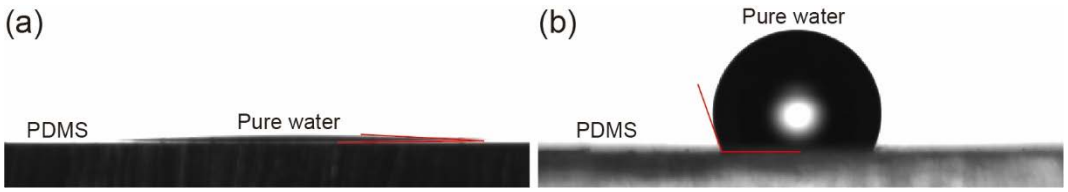

Fig. 2.5 Contact angle measurements of pure water on PDMS surfaces. (a) SPRA-202 coated PDMS surface, showing a contact angle of 3.2 ± 0.4° (n = 10). (b) Uncoated PDMS surface, showing a contact angle of 110.9 ± 2.8° (n = 10).

2.2.3 Chemicals

Chemicals used are listed in **Table 2-2**. A 2 wt% aqueous polyvinyl alcohol (PVA) solution was used as the continuous phase. A precursor, 1,6-Hexanediol diacrylate (HDDA) added by 1 wt% 2-hydroxy-2-methylpropiophenone, was used as the dispersed phase. The produced polymeric particles were washed sequentially by acetone, ethanol, and the pure water.

Table 2-2 Chemicals used.

Droplet formation	
Continuous phase	2 wt% aqueous PVA solution
Dispersed phase	HDDA
Polymeric particle production	
Washing liquid	Pure water Acetone Ethanol

2.2.4 Equipment

Syringe pumps were used to deliver the chemical solutions into the microfluidic device, as listed in **Table 2-3**. The droplet formation and migration were monitored using a microscope equipped with a high-speed video camera. The polymeric particles were examined using a scanning electron microscope under high vacuum mode at an accelerating voltage of 10 kV.

The droplets are counted via the images read by the software ImageJ (National Institute of Health, MD, USA). The details of the equipment are shown in **Appendix A.3**.

Table 2-3 List of equipment used.

Syringe Type	Contents
Gas-tight glass (volume: 1 mL) Plastic (volume: 50 mL)	PVA solution HDDA
Syringe pump	Legato 180 KDS 210

2.2.5 Preparation of polymeric microspheres

Polymeric particles were synthesized from the main droplets using UV light polymerization. The droplets were exposed to UV light for 30 seconds at a distance of approximately 15 cm. After UV exposure, the polymerized particles were collected and washed using a nylon mesh sheet. The microspheres were observed by a scanning electron microscope (FlexSEM 1000, Hitachi High-Tech, Tokyo, Japan) under high vacuum mode at an accelerating voltage of 10 Kv.

2.3 Results and discussion

2.3.1 Formation of droplets via step emulsification

In this study, the ability of step-emulsification nozzles to generate HDDA droplets with the PVA solution as the continuous phase was demonstrated. Under optimized flow conditions, droplet formation occurred consistently across all 60 nozzles. Specifically, with the flow rate of HDDA (Q_d) at 0.1 mL/h and the flow rate of PVA solution (Q_c) at 10.0 mL/h, uniform droplets were produced in the dripping regime (**Fig. 2.6a**). At the triangular ends of the nozzles, the HDDA/PVA interface periodically advanced towards the nozzle tips, where rapid growth and neck pinching of the droplets occurred, ultimately resulting in the detachment of the main droplets. These droplets were highly monodisperse, with a mean diameter (D_{avg}) of 60 μm and a coefficient of variation (CV) of 1.7% (n = 124). The generation rate per nozzle (F) was measured at 4.4 ± 0.3 droplets per second (n = 60). Notably, no droplet coalescence was observed near the nozzle outlets.

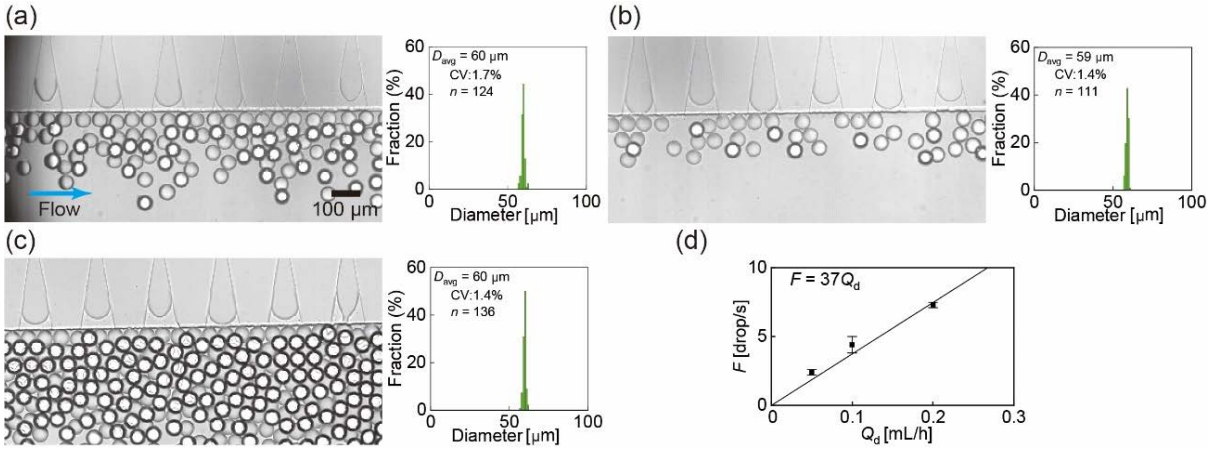

Fig. 2.6 Step emulsification at varying flow rates. (a-c) Droplet formation and size distribution at disperse phase flow rates (Q_d) of (a) 0.1, (b) 0.05, and (c) 0.2 mL/h, with the continuous phase flow rate (Q_c) held constant at 10.0 mL/h. (d) Effect of Q_d on the droplet break-off frequency per nozzle (F).

To investigate the influence of Q_d on droplet formation, we varied Q_d while keeping Q_c constant at 10.0 mL/h. When Q_d was reduced to 0.05 mL/h, the average droplet size and distribution remained unchanged ((D_{avg} = 59 μm and CV = 1.4%, n = 111), but the droplet production rate decreased to 2.3 ± 0.3 droplets per second (n = 60), leading to a lower droplet

density near the nozzles (**Fig. 2.6b**). Conversely, increasing Q_d to 0.2 mL/h did not significantly affect droplet size (D_{avg} = 60 μm and CV = 1.4%, n = 136), but F increased to 6.8 ± 0.7 droplets per second (n = 60), causing a higher droplet density (**Fig.2.6c**). These observations demonstrated the insensitivity of droplet size to variations in Q_d and the linear relationship between Q_d and F (**Fig. 2.6d**) is consistent with previous studies[18,19].

At Q_d values exceeding 0.2 mL/h, monodisperse droplets continued to form in the dripping regime; however, significant coalescence of closely packed droplets was observed before they reached the DLD region (**Fig.2.7a**). The density of the droplets was counted to be around 4220 drops/mm^3 for the formation of coalescence. This coalescence, attributed to the low fraction of PVA solution serving as the surfactant in droplet accumulation, was observed only in devices containing DLD pillars; no such coalescence occurred in the absence of pillars, even under identical flow conditions (**Fig. 2.7b**). The continuous phase flow rate (Q_c) also played a critical role in preventing droplet coalescence. At lower Q_c values, droplet packing density increased, leading to coalescence before the droplets could enter the DLD pillars (**Fig. 2.8a**). Increasing Q_c reduced the packing density and mitigated coalescence, a trend that was similarly observed in devices without DLD pillars (**Fig. 2.8b**). However, at higher Q_c, values, the number of nozzles operating in the dripping regime decreased due to the elevated pressure gradient in the main channel. Based on these findings, the upper limits for the flow rate parameters were determined to be Q_d = 0.2 mL/h and Q_c = 10.0 mL/h to avoid coalescence and maintain stable droplet formation.

High-speed imaging revealed the formation of satellite droplets during droplet detachment, driven by Plateau–Rayleigh instability (**Fig. 2.9a**). These satellite droplets, which were formed when the neck of the main droplet pinched off, had an average diameter of 3.1 μm with a CV of 25.9% (n = 94, **Fig. 2.9b**). The satellite droplets exhibited periodic back-and-forth motion near the nozzles, likely caused by the backflow of the continuous phase as the neck of the main droplet rapidly collapsed.

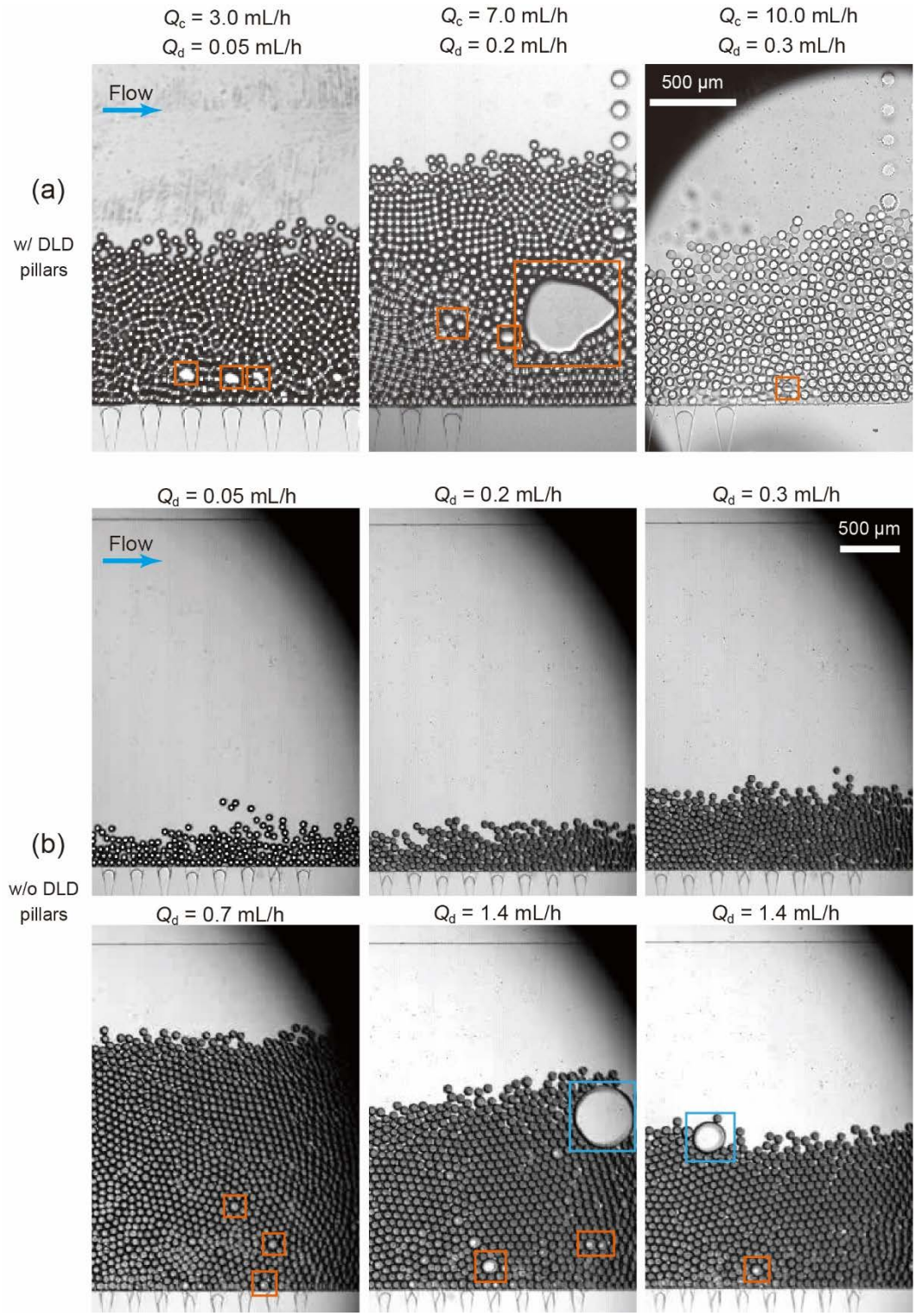

Fig. 2.7 Droplet accumulation and coalescence in devices (a) with and (b) without DLD micropillars under different flow conditions. The orange rectangles highlight coalesced droplets, and the light-blue rectangles indicate droplets generated in the jetting mode.

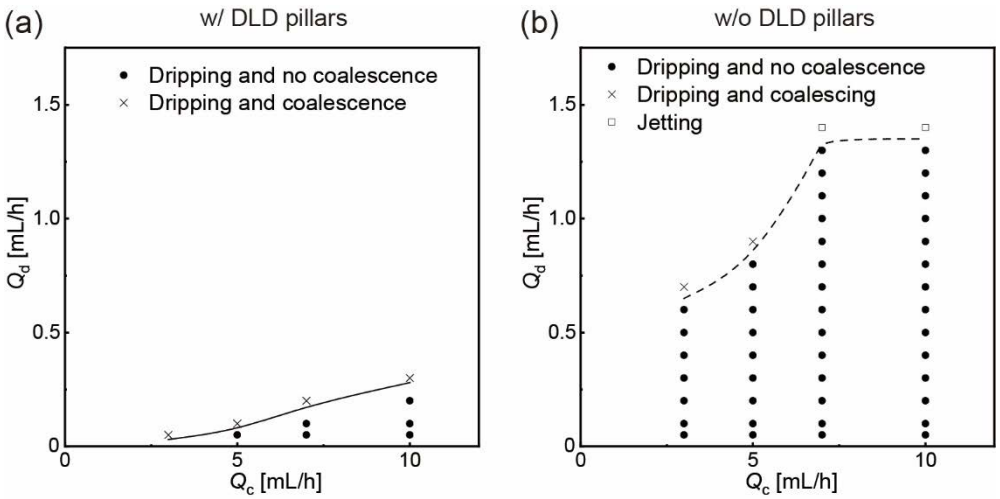

Fig. 2.8 The formation under varied flow conditions and coalescence of main droplets. (a) Diagram showing the flow conditions that allow monodisperse main droplets to form and enter the DLD region without coalescence. (b) Diagram showing the flow conditions for step emulsification in the dripping and jetting regimes in the absence of DLD pillars.

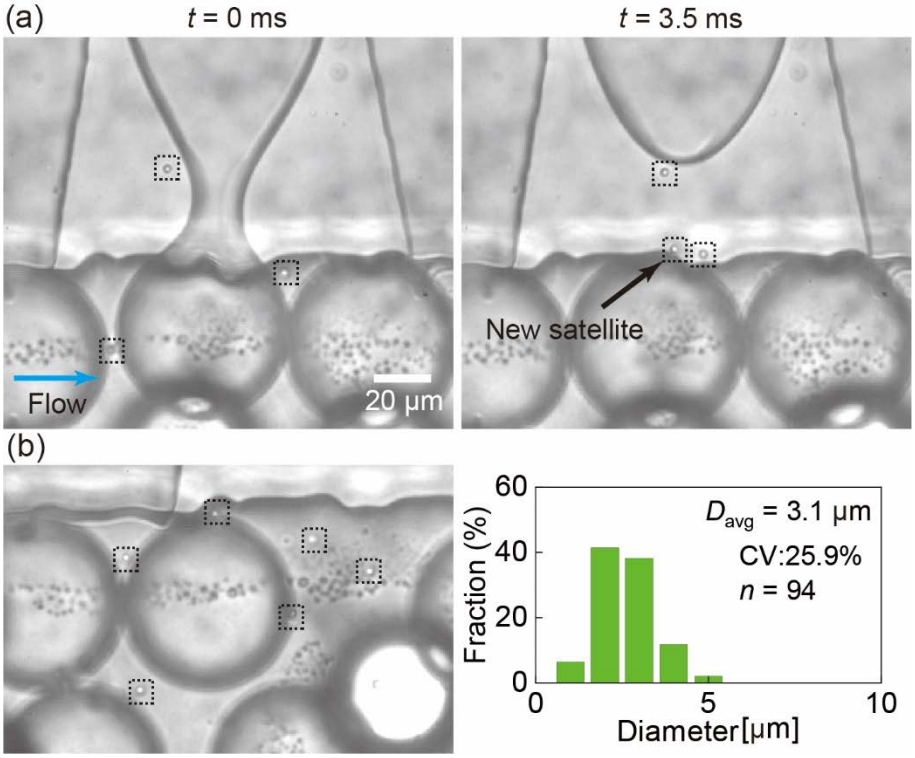

Fig. 2.9 Satellite droplet formation. (a) Time-lapse snapshots of satellite droplets (indicated by dashed squares) around a nozzle, captured at t = 0 ms (before detachment) and t = 3.5 ms (after detachment). (b) Satellite droplets around the nozzle tip and the size distribution at Q_d = 0.1 mL/h and Q_c = 10.0 mL/h.

2.3.2 Separation of main and satellite droplets via DLD pillars

In this study, the main and satellite droplets produced across the nozzles flowed into the DLD section and migrated along different paths through the pillars according to their sizes. **Figure 2.10** shows the migration of the main droplets at flow rates of Q_d = 0.1 mL/h and Q_c = 10.0 mL/h. Under these conditions, the Reynolds number was approximately 0.5, indicating laminar flow. After their generation, the main droplets (D_{avg} = 60 μm) flowed along the sidewall and entered the DLD section through the 80 μm wide gaps near the wall (**Fig. 2.10a**). Minimal accumulation of droplets was observed at the DLD entrance, and no droplet deformation or coalescence occurred. The main droplets migrated towards the central wall in displacement mode. As they moved through the midstream region, the droplets continued to follow the displacement mode, passing across slightly increased number of gaps (gaps 7–13, **Fig. 2.10b**) towards the central wall. In the downstream region, the main droplets were fully displaced, flowing through gaps 16–17 near the central wall and being efficiently collected at outlet-L, with no droplets observed at outlet-S (**Fig. 2.10c**). As expected, droplets larger than D_c of 37 μm followed the

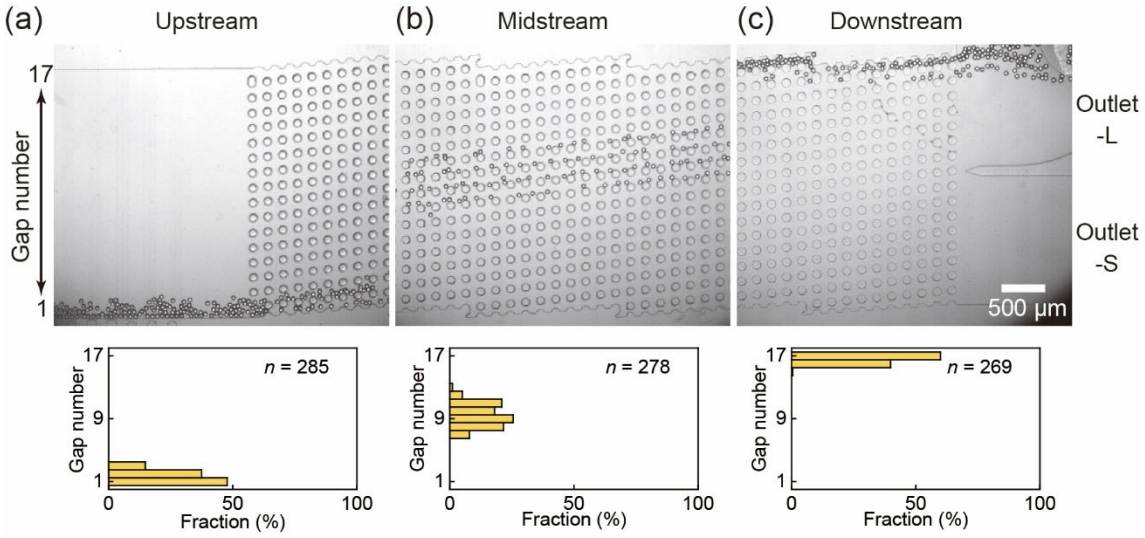

Fig. 2.10 Spatial distribution of main droplets across the DLD pillar array. (a) Main droplets flowing into the DLD section near the sidewall. (b) Main droplets migrating across the midstream region in displacement mode. (c) Fully displaced main droplets flowing into outlet-L. Flow rates: Q_d = 0.1 mL/h, Q_c = 10.0 mL/h.

displacement mode. During migration, some main droplets deviated slightly from their expected paths, likely due to interactions between closely spaced droplets, resulting in partial displacement.

The behavior of satellite droplets in the DLD region was also investigated. **Figure 2.11a** shows that the satellite droplets, which entered the DLD region alongside the main droplets, flowed near the sidewall (gaps 1–2). Unlike the main droplets, the satellite droplets, with an average diameter of 3.1 μm, followed a zigzag mode, maintaining their position near the sidewall throughout the midstream region (gap 1–2, **Fig. 2.11b**) In the downstream region, these satellite droplets continued in the zigzag mode and were collected at outlet-S (gaps 1–2, **Fig. 2.11c**). In addition, the fabricated micropillars were not in a perfect cylinder-shape. However, due to the large difference between the sizes of the main and satellite droplets, the separation performance was not affected by the fabrication defects.

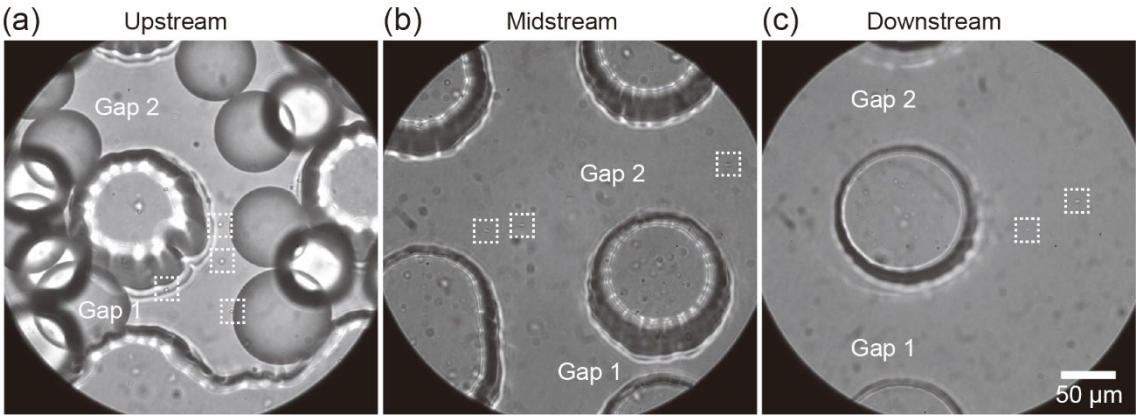

Fig. 2.11 Satellite droplets flowing through the DLD pillar array in zigzag mode. (a) Satellite droplets in the upstream region. (b) Satellite droplets in the midstream region. (c) Satellite droplets in the downstream region. Flow rates: Q_d = 0.1 mL/h, Q_c = 10.0 mL/h.

In the device with DLD pillars, the satellite droplets, being smaller than D_c, followed a distinct path from the main droplets, enabling complete separation. When the dispersed phase flow rate (Q_d) was increased to 0.2 mL/h while keeping Q_c constant at 10.0 mL/h, similar separation between main and satellite droplets was observed, despite the crowding main droplets (**Figs. 2.12** and **2.13**).

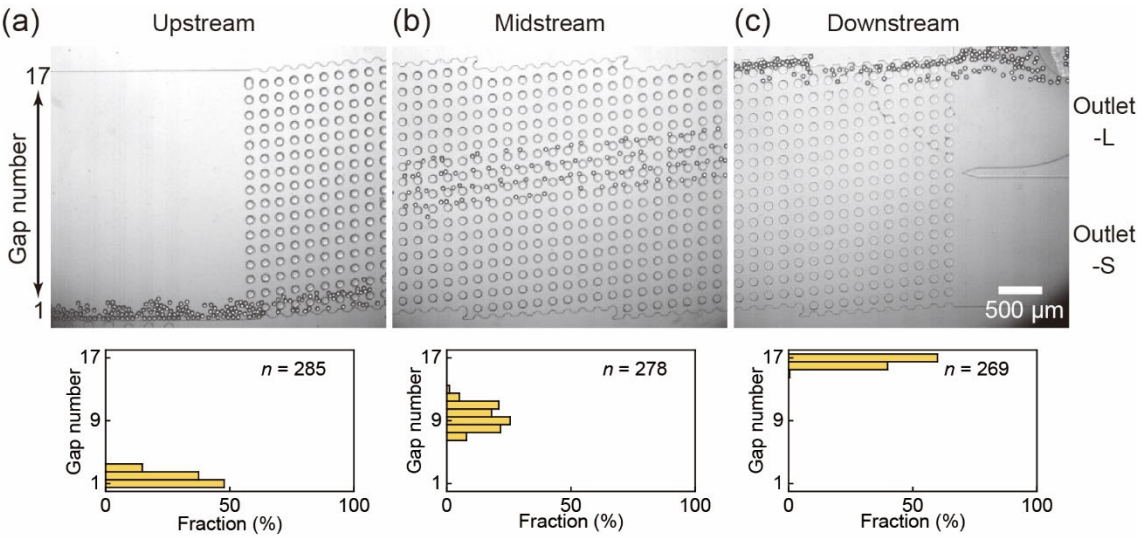

Fig. 2.12 Spatial distribution of main droplets flowing across the DLD pillar array at Q_d = 0.2 mL/h and Q_c = 10.0 mL/h. (a) Main droplets flowing into the DLD region near the sidewall. (b) Main droplets in the midstream region in displacement mode. (c) Fully displaced main droplets flowing into outlet-L.

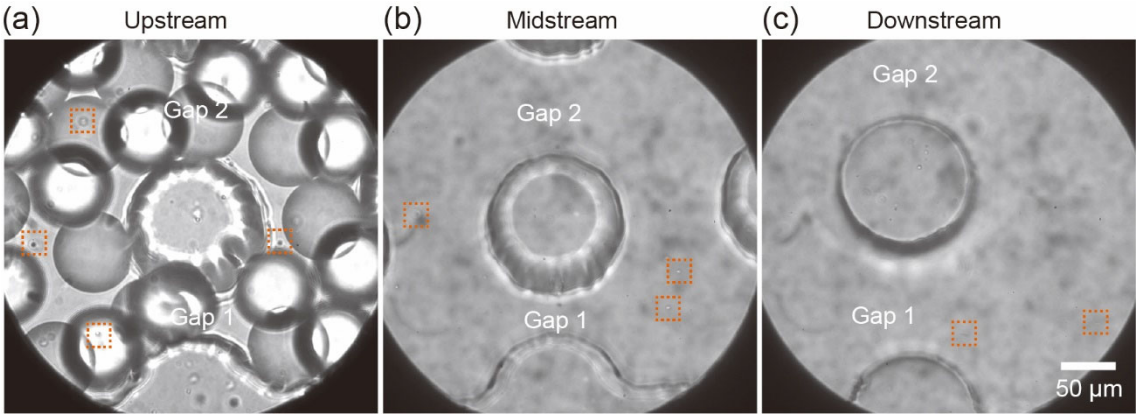

Fig. 2.13 Satellite droplets in the DLD pillars at Q_d = 0.2 mL/h and Q_c = 10.0 mL/h. (a-c) Satellite droplets (dashed squares) moving across the DLD array in zigzag mode in the (a) upstream, (b) midstream, and (c) downstream regions.

For comparison, we also evaluated droplet behavior in a device lacking DLD pillars. In this case, the main droplets, generated at the nozzles, flowed near the sidewall without any accumulation or obstruction, as there were no pillars to disrupt the flow (**Fig. 2.14a**). Some slight displacement of droplets from the sidewall was observed in the midstream region (**Fig. 2.14b**), likely due to localized flow disturbances caused by interactions with the sidewall and

other droplets. In the region before the outlets, main droplets continued to flow near the sidewall, maintaining a distance of 0–1.0 mm from the wall, and were collected at outlet-S (**Fig. 2.14c**). Satellite droplets, with a maximum distance of 0.3 mm from the sidewall, also entered outlet-S, as shown in magnified views of the upstream and downstream regions (**Fig. 2.15**). Similar patterns were observed with Q_d at 0.2 mL/h. These results show that a device without DLD pillars is unable to effectively separate main and satellite droplets.

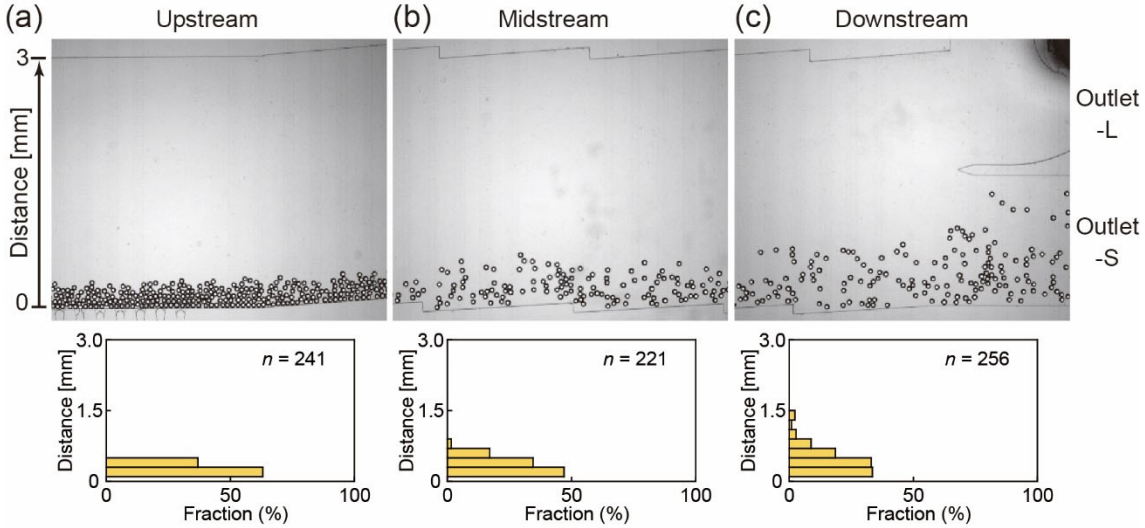

Fig. 2.14 Spatial distribution of main droplets in the no-pillar device. (a) Main droplets in the upstream region immediately after the nozzles. (b) Main droplets in the midstream region. (c) Main droplets in the downstream region near the outlets. Flow rates: Q_d = 0.1 mL/h, Q_c = 10.0 mL/h.

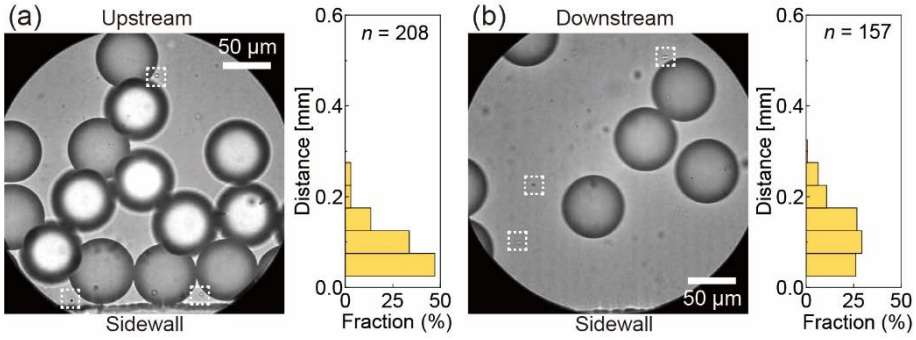

Fig. 2.15 Satellite droplets in the no-pillar device. (a) Satellite droplets (dashed squares) in the upstream region. (b) Satellite droplets in the downstream region, showing their distances from the sidewall. Flow rates: Q_d = 0.1 mL/h, Q_c = 10.0 mL/h.

2.3.3 Characterization of droplets and particles

The separated main droplets were collected in an off-chip petri dish for size analysis. The main droplets exhibited high monodispersity, with an average diameter of 58 μm and a coefficient of variation (CV) of 2.8% (n = 208, **Fig. 2.16a**). This diameter (58 μm) was slightly smaller than the droplets immediately after formation (60 μm), likely due to the partial solubility of HDDA in water (0.36 g/L at 20 °C). Some HDDA droplets may have dissolved into the continuous aqueous phase during migration through the microchannel and collection in the petri dish.

Photopolymerization of the main droplets was implemented under UV exposure of light. The resulting crosslinked polymeric microspheres had a mean diameter of 55 μm and a CV of 2.9% (**Fig. 2.16b**), maintaining the same high level of monodispersity as the precursor droplets. The polymer spheres exhibited a shrinkage ratio of approximately 5.5% compared to the initial droplet size after photopolymerization.

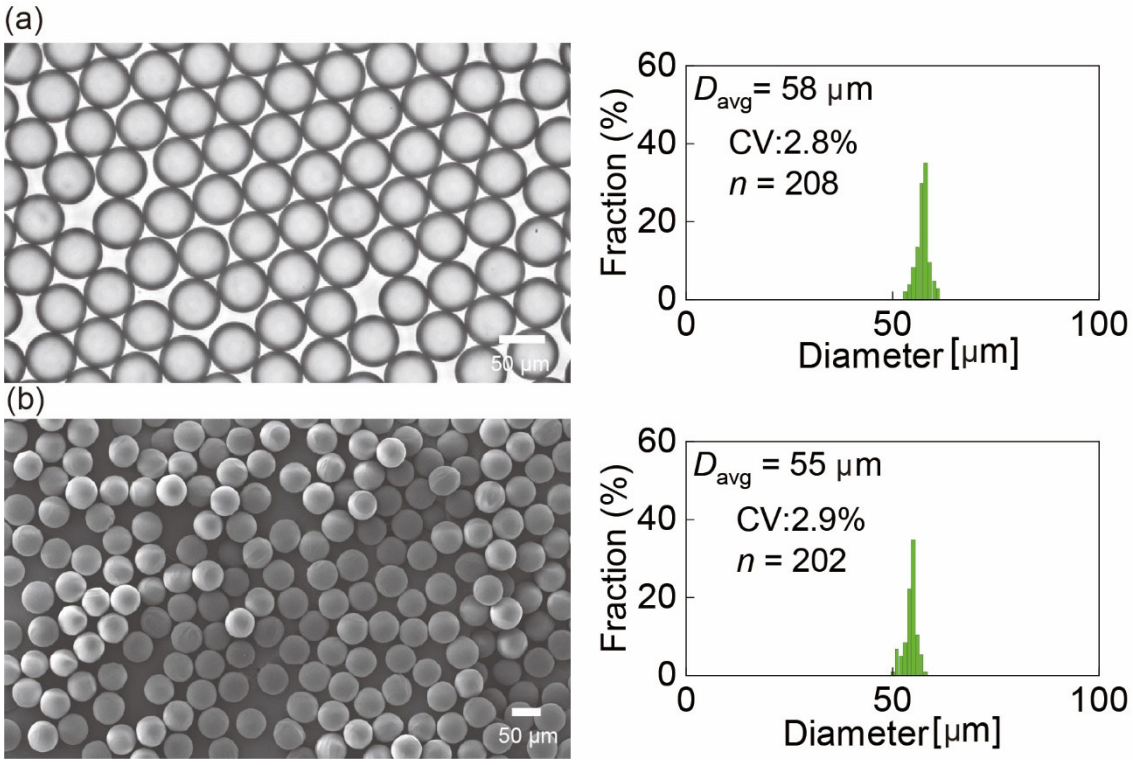

Fig. 2.16 (a) Main droplets collected from outlet-L, along with their diameter distribution. (b) SEM image of the microspheres and their diameter distribution.

2.3.4 Advantages, limitations, and scope of the device

The developed microfluidic device presents several advantages over the droplet-sorting devices that use shear stress-driven droplet generators and DLD pillars. First, this device is free from additional sheath fluid or flow-rate adjustments to pre-focus the droplet stream before it enters the DLD region. Since the droplets are produced at the sidewall nozzles, they enter the DLD region directly along the sidewall, simplifying both the design and operation compared to earlier systems[13,14,18,19]. Secondly, unlike sheathless devices that utilize flow-focusing droplet generators and DLD pillars[13,14] but are limited to using only half of the DLD region, this device makes full use of the entire DLD region. Thirdly, the number of step emulsification-based droplet generators can be easily scaled up to increase droplet throughput without requiring a larger device footprint, a limitation often encountered in shear-induced systems[13]. Finally, step emulsification is known for its robustness against flow fluctuations, making it a more stable method of droplet generation compared to shear-based approaches[20,21].

In addition to these advantages, this device holds potential for broader applications. For example, by configuring multiple DLD sections with different critical diameters (D_c), it may be possible to fractionate satellite droplets of varying sizes[13]. Furthermore, the system can be adapted to handle water-in-oil droplets by modifying the channel surface to be hydrophobic.

However, some limitations remain. Droplet accumulation and coalescence at the entrance of the DLD section affect the monodispersity and/or productivity. Two potential strategies to address this issue are under investigation. The first involves increasing the gap size of the DLD pillars by adjusting D_c to more closely match the size of the main droplets, which would require reducing the shift between pillar columns (Eq. 1). The second strategy is to position the DLD pillars upstream, directly in front of the nozzles, rather than in the downstream regions. However, this would necessitate careful control of the pressure gradient to prevent deactivation of the nozzles.

2.4 Conclusion

This study demonstrates the successful integration of deterministic lateral displacement (DLD) micropillar arrays with a cross-flowing step emulsifier for the advanced processing of monodisperse, satellite-free droplets and polymeric particles. The device's array of 60 nozzles reliably generated highly monodisperse main droplets (approximately 60 μm in diameter, with a coefficient of variation (CV) below 2%) as well as satellite droplets (around 3 μm in diameter). These droplets were subsequently separated and collected with 100% purity using downstream DLD micropillars with a critical diameter (D_c) of 37 μm. The main droplets were further processed to produce monodisperse polymeric microspheres through photopolymerization, free from any satellite droplet contamination. This novel device offers a promising solution for improving the purity of products in conventional step emulsification processes, with potential for wider applications in droplet microfluidics.

References

[1] Y. Zhang, G. Hu, Y. Liu, J. Wang, G. Yang, D. Li. Suppression and utilization of satellite droplets for inkjet printing: a review. *Processes*, **2022**, 10, 932.

[2] V. Cristini, T. C. Tan. Theory and numerical simulation of droplet dynamics in complex flows—a review. *Lab Chip*, **2004**, 4, 257–264.

[3] J. Eggers. Drop formation–an overview. *ZAMM-Z. Angew. Math. Mech.*, **2005**, 85, 400–410.

[4] X. Sun, C. Zhu, T. Fu, Y. Ma, H. Z. Li. Dynamics of droplet breakup and formation of satellite droplets in a microfluidic T-junction. *Chem. Eng. Sci.*, **2018**, 188, 158–169.

[5] M. L. Eggersdorfer, H. Seybold, A. Ofner, D. A. Weitz, A. R. Studart. Wetting controls of droplet formation in step emulsification. *Proc. Natl. Acad. Sci. USA*, **2018**, 115, 9479–9484.

[6] T. Nisisako, T. Torii, T. Higuchi. Separation of satellite droplets using branch microchannel configuration. *Proc. Micro Total Anal. Syst.* **2004**, 2, 312–314.

[7] C. H. Yang, Y. S. Lin, K. S. Huang, Y. C. Huang, E. C. Wang, J. Y. Jhong, C. Y. Kuo. Microfluidic emulsification and sorting assisted preparation of monodisperse chitosan microparticles. *Lab Chip*, **2009**, 9, 145–150.

[8] Y. C. Tan, A. P. Lee. Microfluidic separation of satellite droplets as the basis of a monodispersed micron and submicron emulsification system. *Lab Chip*, **2005**, 5, 1178–1183.

[9] L. R. Huang, E. C. Cox, R. H. Austin, J. C. Sturm. Continuous particle separation through deterministic lateral displacement. *Science*, **2004**, 304, 987–990.

[10] J. McGrath, M. Jimenez, H. Bridle. Deterministic lateral displacement for particle separation: A review. *Lab Chip*, **2014**, 14, 4139–4158.

[11] T. Salafi, Y. Zhang, Y. Zhang. A review on deterministic lateral displacement for particle separation and detection. *Nano-Micro Lett.*, **2019**, 11, 77.

[12] A. Hochstetter, R. Vernekar, R. H. Austin, H. Becker, J. P. Beech, D. A. Fedosov, G. Gompper, S. C. Kim, J. T. Smith, G. Stolovitzky. Deterministic lateral displacement:

Challenges and perspectives. *ACS Nano*, **2020**, 14, 10784–10795.

[13] N. Tottori, T. Hatsuzawa, T. Nisisako. Separation of main and satellite droplets in a deterministic lateral displacement microfluidic device. *RSC adv.*, **2017**, 7, 35516–35524.

[14] N. Tottori, T. Nisisako. High-throughput production of satellite-free droplets through a parallelized microfluidic deterministic lateral displacement device. *Sen. Actuators B: Chemical*, **2018**, 260, 918–926.

[15] E. Amstad, M. Chemama, M. Eggersdorfer, L. R. Arriaga, M. P. Brenner, D. A. Weitz. Robust scalable high throughput production of monodisperse drops. *Lab Chip*, **2016**, 16, 4163–4172.

[16] D. W. Inglis. Efficient microfluidic particle separation arrays. *Appl. Phys. Lett.*, **2009**, 94, 013510.

[17] J. A. Davis. Microfluidic separation of blood components through deterministic lateral displacement. PhD thesis, Princeton University, USA, September, **2008**.

[18] H. N. Joensson, M. Uhlén, H. A. Svahn. Droplet size based separation by deterministic lateral displacement—separating droplets by cell-induced shrinking. *Lab Chip*, **2011**, 11, 1305–1310.

[19] T. Jing, R. Ramji, M. E. Warkiani, J. Han, C. T. Lim, C. H. Chen. Jetting microfluidics with size-sorting capability for single-cell protease detection. *Biosens. Bioelectron.*, **2015**, 66, 19–23.

[20] Z. Shi, X. Lai, C. Sun, X. Zhang, L. Zhang, Z. Pu, D. Li. Step emulsification in microfluidic droplet generation: mechanisms and structures. *Chem. Comm.*, **2020**, 56, 9056–9066.

[21] Z. Liu, C. Duan, S. Jiang, C. Zhu, Y. Ma, T. Fu. Microfluidic step emulsification techniques based on spontaneous transformation mechanism: A review. *J. Ind. and Eng. Chem.*, **2020**, 92, 18–40.

Chapter 3

Post-formation fluorescent labeling of main droplets

3.1 Introduction

3.1.1 Functional materials in microfluidics

In **Chapter 1**, the formation of droplets using various microfluidic methods was briefly introduced, with a focus on droplet generation via step emulsification nozzles in single modules in the previous chapter was demonstrated. Beyond droplet formation, the production of functional materials is a critical application of microfluidics, offering the ability to engineer specific functionalities through diverse materials and structures (**Fig. 3.1**)[1]. Functional material, which has great potentials in practical applications, have been widely applied in fields such as drug delivery, cell culture, micromachine components, photonic crystals, and energy materials[1–4].

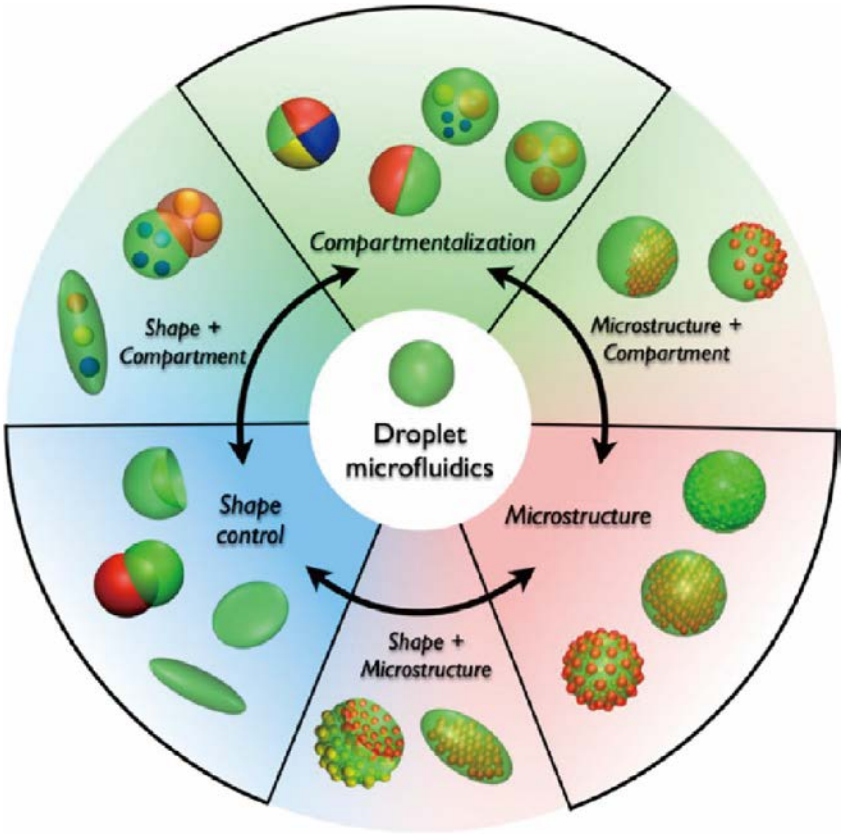

Fig. 3.1 Functional microparticles with various compounds and structures[1]. Reproduced with permission from American Chemical Society.

3.1.2 Functional materials from step emulsification

While **Chapter 2** touched upon the production of droplets, production of functional materials via step emulsification has also gained significant attention[5–18]. Nakajima's group, who pioneered the step emulsification in 1997[19], produced gelatin particles using a silicon-based step emulsification device[5]. This group further developed a production of alginate microspheres using arrayed step emulsification nozzles and external gelation[6]. A further production of alginate-based functional particles has also been demonstrated by Bitar et al., who produced cell-loaded alginate hydrogel microparticles via a step emulsification and inner gelation process[7]. They used a 3D printed sheet with through holes serving as the step emulsifiers, which was sandwiched by two parts for introducing liquids. A mixture of an aqueous alginate solution, a suspension containing mammalian cells, and a $CaCO_3$ suspension was utilized as the dispersed phase; while an acidified mineral oil was used as the continuous phase. Droplets formed at the through holes were collected and remained in the collection vessel for sufficient gelation (**Fig. 3.2a**).

Significant progress has also been made in drug-loaded productions via step emulsification. This technique commonly uses the liquid, in which the drugs dissolve, as the dispersed phase. For example, Neves et al. from Nakajima's group proposed a production of bioactive molecules-loaded emulsions via step emulsification nozzles[12]. As shown in **Fig. 3.2b**, the oil-in-water droplets with uniform sizes formed at the nozzles, which is similar as the introduced droplet formation via through holes in **Chapter 1**. In addition to this example, more productions of drug-loaded emulsions with various compounds have been reported[13–15].

While the production of particles and emulsions with diverse materials has been greatly investigated, step emulsification has also been used to produce droplets with complex structures such as the double emulsions[16–18]. For example, the production of double emulsions can be easily achieved by using a pre-homogenized water-in-oil emulsion as the dispersed phase[16]. However, this method has low controllability over the core number in the double emulsions. Eggersdorfer et al. demonstrated a production of double emulsions using two serially connected step emulsification components[17]. As shown in **Fig. 3.2c**, a device having

step emulsification nozzles in both the up- and downstream regions was designed. The first step emulsification part produced the water-in-oil emulsions, which were guided towards the second step emulsification part and served as the dispersed phase. Subsequently, the water-in-oil-in-water double emulsions were produced. In this production, by adjusting the ratio of the inner and middle flows, the fractions of the emulsions with no core, single core, and double or more cores can be precisely controlled. An optimized ratio of the inner and middle flows was found to be 1:2 with the fraction of single core double emulsions over 90%. Further experiments of this study pointed out that the volume and shell thickness of the double emulsions can be simply controlled by adjusting the height of the two step emulsification nozzles. Such a production of double emulsions via tandem step emulsification nozzles has also been reported by Ofner et al.[18].

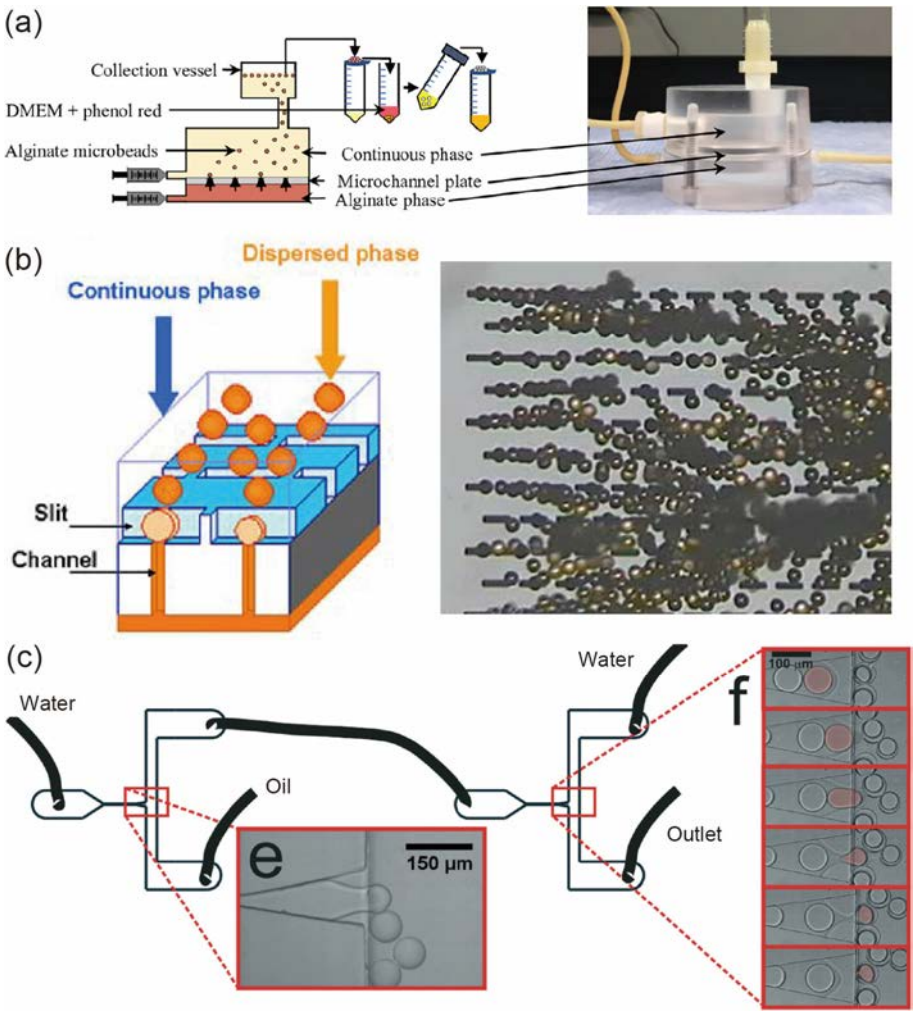

Fig. 3.2 Production of particles and emulsions via step emulsification nozzles. (a) Cell-loaded alginate microparticles[7]. (b) Bioactive molecules-loaded emulsions[12]. And (c) double emulsions[17]. (a) Reproduced with permission from Wiley. (b) Reproduced with permission from Springer. (c) Reproduced with permission from The Royal Society of Chemistry.

3.1.3 Objective

In this chapter, the advanced processing of the fluorescent-modified polymer particle is demonstrated. The process begins with the formation of monomer droplets using step-emulsification nozzle arrays located in the upstream region. These droplets then pass through DLD micropillar arrays in the downstream region, where they encounter streams of fluorescent nanoparticles and a pure PVA solution. As the main droplets migrate through the nanoparticle and PVA streams, they undergo bumping within the DLD arrays, leading to their functionalization. The step-emulsification nozzles, positioned alongside the main channel, are

coupled with the DLD micropillar arrays in parallel, which are located within the main channel. This setup allows the ends of the nozzles to align with the DLD region. The formation of both main and satellite droplets at the step-emulsification nozzles was initially investigated. Subsequently, the size-dependent migration paths of the main and satellite droplets through the DLD micropillar array were observed. Finally, the presence of fluorescence in the modified polymeric particles confirmed successful functionalization within the DLD micropillar array.

3.1.4 Outline of this chapter

Section 3.1 Introduction

An overview of the production of functional particles using microfluidics.

Section 3.2 Materials and methods

Describes the microfluidic devices used in this chapter, their fabrication processes, and the peripheral equipment.

Section 3.3 Results and discussion

Presents the results of droplet generation and migration, followed by the demonstration of the produced fluorescent droplets and particles.

Section 3.4 Conclusion

Summarizes the key conclusions drawn in this chapter.

3.2 Materials and methods

3.2.1 Device design and mechanism

A microfluidic device incorporating step-emulsification nozzles and DLD micropillar arrays was developed, building on the device introduced in **Chapter 2** (**Fig. 3.3**). This device features 60 step-emulsification nozzles arranged in two arrays, with their ends connected to the main channel for generating monomer droplets (**Fig. 3.3a**). The nozzles have a height of 14 μm (**Fig. 3.3b**). Two DLD micropillar arrays, with a critical diameter (D_c) of 37 μm, are located in the downstream region to functionalize and separate the main droplets (**Fig. 3.3c**). The PDMS chip was fabricated using the SU-8 mold described in **Chapter 2**. The chip includes three inlets: one at the beginning of the main channel for introducing pure PVA solution, one at the side channel for HDDA, and a third near the main channel's inlet for introducing PVA solution containing nanoparticles. This nanoparticle inlet is positioned close to the main channel sidewall, ensuring that the nanoparticle-containing fluid flows along the sidewall. Two outlets (outlet-L and outlet-S) were created to collect the functionalized main droplets, and the smaller droplets or nanoparticles, respectively. Other parts of the device, including the step-emulsification nozzles and the DLD micropillar array, remain consistent with the device described in **Chapter 2**.

The mechanism of this device is illustrated in **Fig. 3.3a**. The dispersed phase, continuous phase, and nanoparticle fluid are infused separately through the three inlets. Similar to the droplet formation process described in **Chapter 2**, monodisperse main droplets are formed at the nozzle tips in a dripping regime, with satellite droplets detaching from the main droplets. These droplets then flow through the nanoparticle fluid stream and enter the DLD region downstream. In this stream, the droplets are functionalized by the surrounding fluorescent nanoparticles in the DLD array for the advanced processing of fluorescent microparticles. Within the DLD micropillar array, main droplets with diameters larger than D_c migrate laterally across the micropillars at a shift angle in the bump mode towards the sidewall. As they migrate, the main droplets exit the nanoparticle fluid stream and enter the pure continuous phase flow. In contrast, the smaller satellite droplets follow a zigzag path along the sidewall. In the downstream region, the sufficiently displaced main droplets are collected

via the outlet-L, while the satellite droplets and nanoparticle fluid are collected via outlet-S.

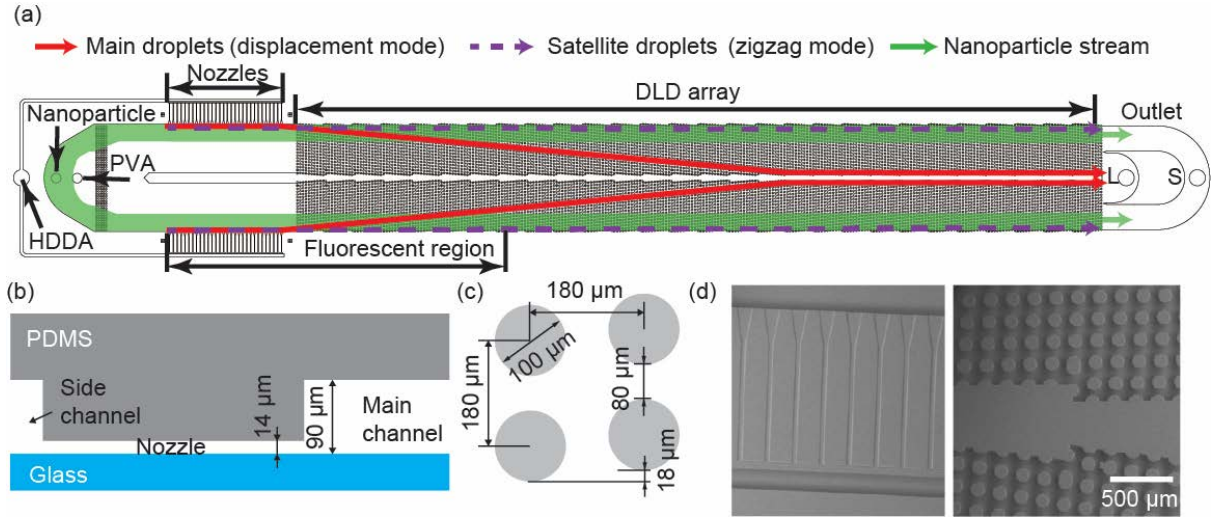

Fig. 3.3 (a) Schematic illustrations of the microfluidic device. Droplets formed at the nozzles are functionalized in the nanoparticle fluid stream. As they migrate through the DLD array, the main droplets enter the pure PVA solution stream and are collected via outlet-L, while the satellite droplets and nanoparticles are collected via outlet-S. Size parameters of (b) the step emulsification nozzle and (c) the DLD array. (d) SEM images of the step emulsification nozzles and the DLD micropillars in the PDMS device.

3.2.2 Device fabrication, chemicals, and experimental setup

The PDMS chip (**Fig. 3.3d**), chemicals, and equipment (including syringes and syringe pumps) used in this study were the same as those described in **Chapter 2**. In addition to the two inlets and outlets, an additional inlet was created to introduce the nanoparticle fluid. A 2 wt.% PVA solution containing 0.06 wt.% fluorescent nanoparticles (#24051-10, 300 nm; Polysciences, PA, USA) was loaded into a plastic syringe for use as the fluorescence fluid. A confocal laser scanning microscope (CLSM, LSM780, Carl Zeiss, Jena, Germany) was employed to observe the interior of the fluorescent monomer droplets. The collected fluorescent monomer droplets were photopolymerized following the same procedure as demonstrated in **Chapter 2**.

3.3 Results and discussion

3.3.1 Droplet formation in step emulsification nozzles

The initial experiment focused on the formation of main and satellite droplets at the ends of the step-emulsification nozzles. The flow rates for the HDDA, nanoparticle stream, and aqueous PVA solution were set at 0.1 mL/h, 2.0 mL/h, and 4.0 mL/h, respectively. Under these conditions, the main droplets were generated at a rate of 480 drops/s across 60 nozzles. High-speed camera footage (captured at 1000 fps) provided a magnified view of the droplet formation processing the nanoparticle fluid (**Fig. 3.4**). Similar to the results observed with pure PVA solution, the presence of nanoparticles did not disrupt droplet formation; both the main and satellite droplets successfully broke off from the HDDA fluid. As the HDDA fluid passed the nozzle edges, a tongue-shaped tip rapidly formed, with the neck between the tip and the bulk fluid narrowing, resulting in the production of monodisperse droplets. This process closely mirrored the droplet formation described in **Chapter 2**. During droplet formation, we observed a backflow of nanoparticles and fluid into the nozzle, a phenomenon not noted in **Chapter 2**. However, due to their small size and low volume fraction, these nanoparticles did not significantly impact the droplet formation process. In the downstream region before the DLD array, there was no evidence of dense accumulation or coalescence of droplets (**Fig. 3.5a**). Additionally, under fluorescence microscopy, the droplets were observed to continue flowing within the nanoparticle fluid stream as they approached the DLD array (**Fig. 3.5b**).

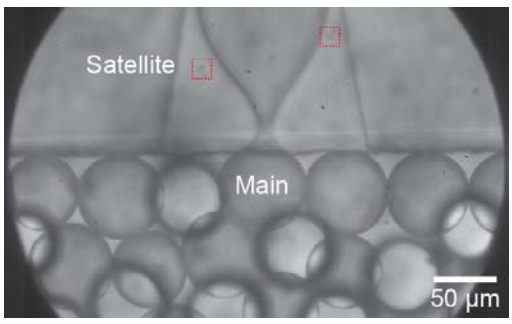

Fig. 3.4 Droplet formation at a step-emulsification nozzle. Monodisperse main and the satellite droplets (indicated by dashed squares) are produced within the nanoparticle fluid stream.

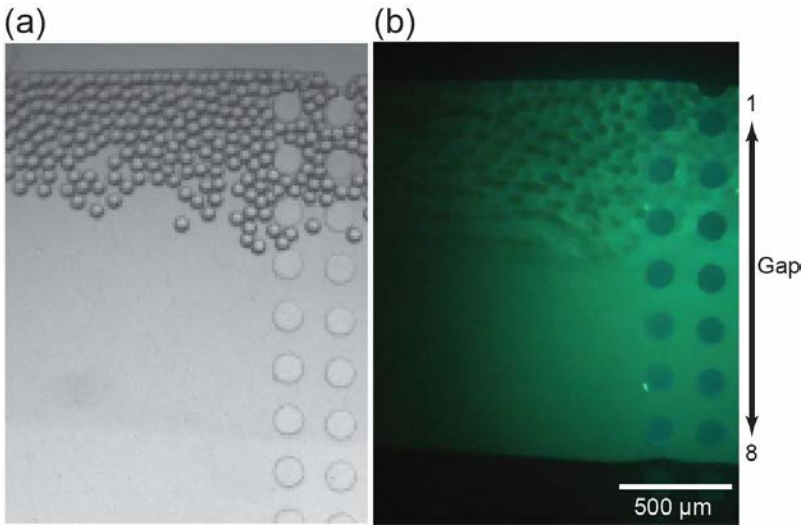

Fig. 3.5 Main droplets before entering the DLD array observed under (a) bright field and (b) fluorescence field. No coalescence of droplets was observed. The fluorescent nanoparticle fluid stream flows into the DLD array through DLD gaps 1–8.

3.3.2 Migration of main and satellite droplets

The main and satellite droplets generated at the nozzles enter the DLD region along the nanoparticle fluid stream and migrate separately through the pillars based on their sizes (**Fig. 3.6a**). At flow rates of 2 mL/h for the nanoparticle fluid and 4 mL/h for the pure PVA solution, the first set of gaps in the DLD array (gaps 1–8) are filled with the nanoparticle fluid, while the remaining gaps (gap 8-17) are filled with pure PVA solution. The Reynolds number under this flow condition is approximately 0.3, indicating laminar flow through the pillars, with no deformation of the droplets observed. The main droplets initially migrate towards the central wall in displacement mode. In the 13th DLD section, corresponding to the midstream region, the main droplets flow in bump mode through the increased gaps (gaps 6–16) towards the central wall (**Fig. 3.6b**). At the exit of the DLD array, corresponding to the downstream region, the main droplets are sufficiently displaced, flowing through gaps 15–17 near the central wall, and are collected via outlet-L with 100% efficiency; no main droplet is observed in outlet-S (**Fig. 3.6c**). This confirms that the main droplets produced by the step-emulsification nozzles, with diameters larger than D_c (37 μm), migrate through the pillars in bump mode as expected.

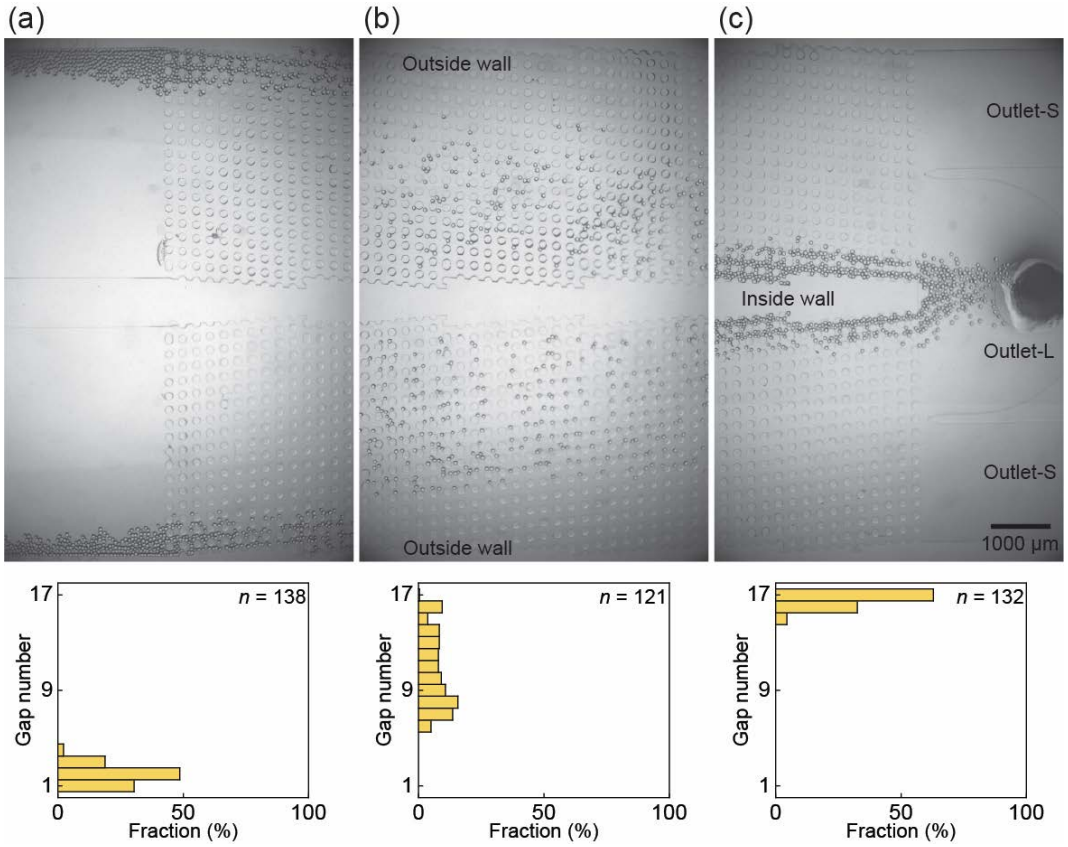

Fig. 3.6 Spatial distribution of main droplets flowing through the DLD pillar arrays. Droplets at the (a) entrance of DLD arrays, (b) 13th DLD section corresponding to the midstream, and (c) exit of the DLD arrays were counted.

Next, the migration of satellite droplets through the DLD arrays under bright field was investigated. In the upstream region, satellite droplets were observed entering the DLD region near the sidewall (gaps 1–2) alongside the main droplets (**Fig. 3.7a**). In the midstream region, unlike the main droplets, the satellite droplets maintained their vertical position relative to the flow, moving near the sidewall (gap 1–2, **Fig. 3.7b**) in zigzag mode. In the downstream region, the satellite droplets continued to flow near the sidewall (gaps 1–2, **Fig. 3.7c**) and were collected via outlet-S.

The migration performance under the fluorescence field was also recorded. In **Fig. 3.8**, the green fluorescent region of the main channel corresponds to the nanoparticle fluid stream, while the dark region corresponds to the pure PVA solution stream. The displacement of the main droplets from the fluorescent nanoparticle fluid into the pure PVA solution was observed. At the entrance of the DLD array, corresponding to the upstream region, the HDDA monomer

main droplets entered the DLD array within the fluorescent nanoparticle fluid (**Fig. 3.8a**). In the 14th DLD section, corresponding to the midstream region, the main droplets were displaced, and no main droplets were observed within the nanoparticle flow (**Fig. 3.8b**). At the exit of the DLD array, corresponding to the downstream region, the fluorescent main droplets were sufficiently displaced, flowing through gaps 15–17 near the central wall, and were collected via outlet-L, while the fluorescent nanoparticle fluid, devoid of main droplets, was collected via outlet-S (**Fig. 3.8c**).

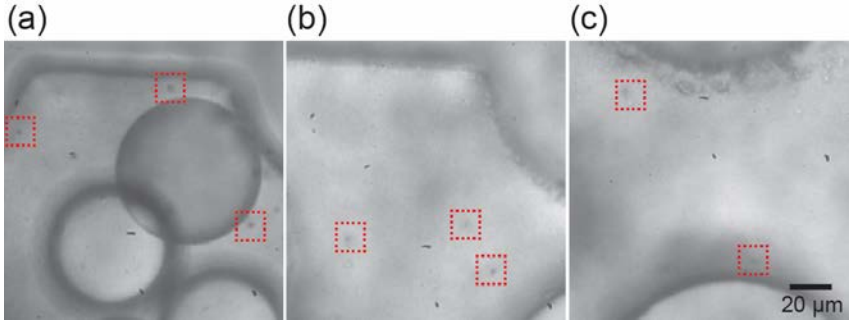

Fig. 3.7 Migration of the satellite droplets at the (a) entrance of DLD arrays, (b) 13th DLD section corresponding to the midstream, and (c) exit of the DLD arrays. Satellite droplets are indicated by red dashed squares.

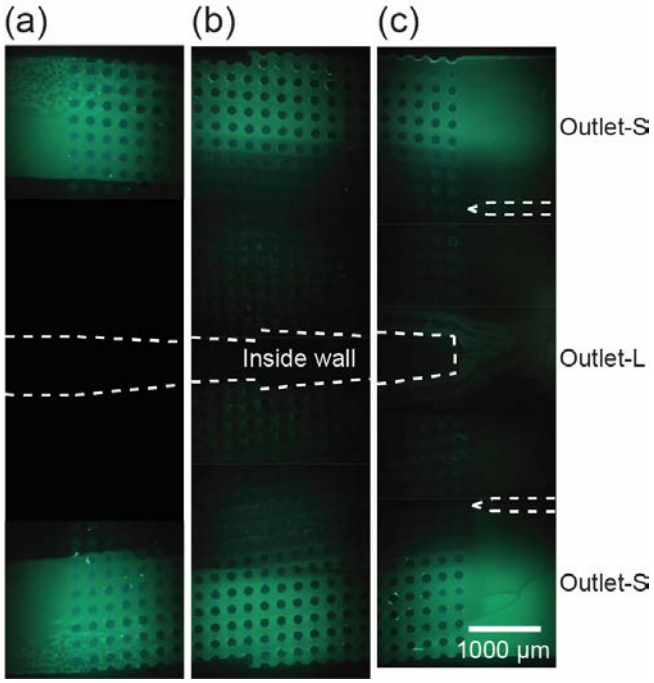

Fig. 3.8 Migration of the main droplets in the (a)upstream, (b) midstream, and (c) downstream regions under the fluorescence field. Fluorescent main droplets were collected via outlet-L.

3.3.3 Characterization of droplets and microspheres

The main droplets, functionalized by nanoparticles and separated from satellite droplets via the DLD array, were collected in an off-chip petri dish for size measurement. The collected main droplets were highly monodisperse, with a mean diameter of 50 μm and CV of 3.9% (n = 110, **Fig. 3.9a**). Under fluorescence microscopy, the droplets exhibited bright fluorescence consistent with the color of the nanoparticles, confirming successful on-chip functionalization within the microchannel. Further observation under a confocal laser scanning microscope (CLSM) revealed fluorescence across the entire cross-section of the droplet slice, indicating effective encapsulation of the nanoparticles within the monomer droplets (**Fig. 3.10a and b**). In addition, an observation using the scanning electronic microscope (SEM; FlexSEM 1000, Hitachi High-Tech, Tokyo, Japan) showed that the polymeric microspheres had smooth surfaces without adhesion of nanoparticles (**Fig. 3.10c**).

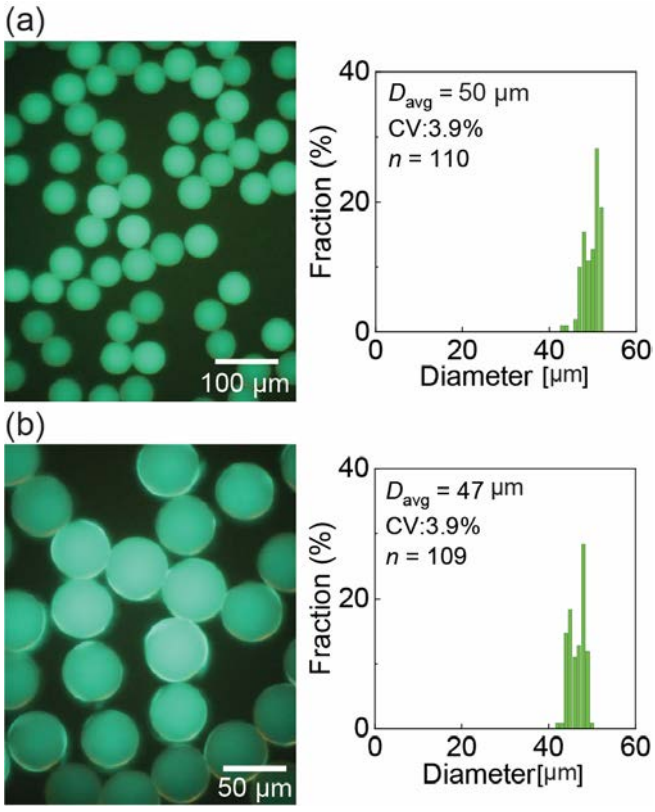

Fig. 3.9 Size distribution of the fluorescent (a) precursor droplets and (b) microspheres observed under fluorescence microscopy. The precursor droplets have a mean diameter of 50 μm, while the microspheres exhibit a slightly smaller mean diameter of 47 μm. Fluorescence was confirmed in both the droplets and microspheres.

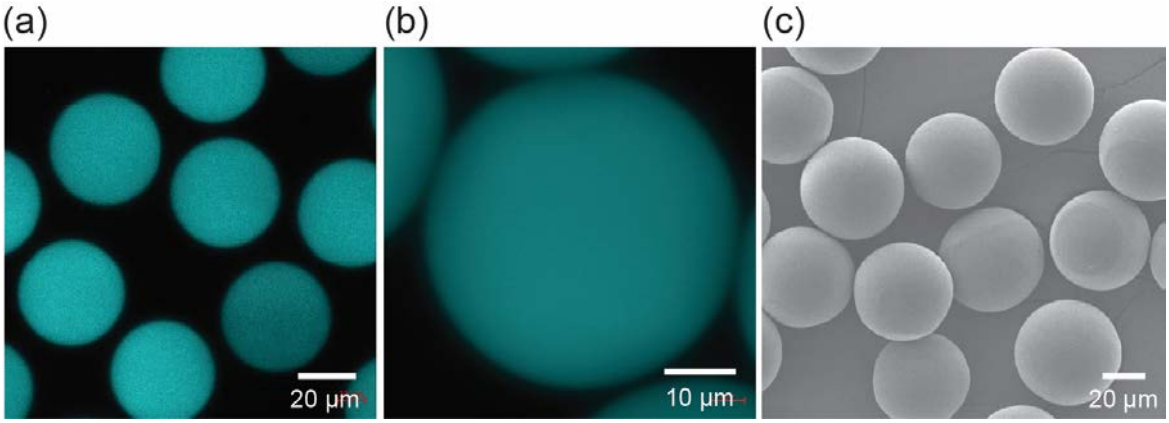

Fig. 3.10 (a) CLSM images of precursor droplets. (b) A magnified image of the droplet's central slice, showing fluorescence throughout, confirming nanoparticle encapsulation within the droplets. (c) SEM image of the HDDA microspheres.

These collected main droplets were subsequently exposed to UV light for photopolymerization. The resulting microspheres were then observed under both bright field and fluorescence microscopy. As shown in **Fig. 3.9b**, the crosslinked polymeric microspheres had a mean diameter of 47 μm and CV of 3.9% (n = 109), demonstrating a monodispersity similar to that of the precursor droplets. Additionally, the microspheres exhibited fluorescence, confirming the successful production of functionalized fluorescent microspheres via the DLD array.

3.3.4 Discussion

We demonstrated a straightforward method for the advanced processing of fluorescent functional microspheres using DLD micropillar arrays. In this study, the DLD arrays were utilized not only as a separator for sorting the main droplets but also as a chamber for the functionalization of precursor droplets. Unlike approaches that require an external washing process for the final product, pure precursor droplets without extra nanoparticles were produced in this study, enabling simpler operation. Additionally, as in the droplet production methods described in previous chapters, the main precursor droplets are effectively separated from the satellite droplets, further enhancing the purity of the final products.

However, one limitation of this method is that droplets produced at different positions

within the nozzle array have varying functionalization times, potentially leading to inconsistencies in the final products. To address this issue, the entrance for the nanoparticle fluid could be relocated to the region between the step-emulsification nozzles and the DLD array, ensuring more uniform functionalization.

This droplet functionalization approach has broad potential applications. By varying the materials or chemicals used for functionalization, it is possible to produce a wide range of functional particles. For example, replacing the nanoparticle with magnetic particles would allow for the production of magnetic polymeric microspheres.

3.4 Conclusion

This chapter presented a simple method for producing fluorescent polymeric microspheres using DLD micropillar arrays without the need for off-chip washing. A device having 60 step emulsification nozzles and a DLD micropillar array with a critical diameter D_c of 37 μm was developed. A fluid containing fluorescent nanoparticles flowed through a region near the sidewall, enabling on-chip functionalization of the precursor droplets. The droplets, with a mean diameter of approximately 50 μm, first passed through the nanoparticle fluid stream along the sidewall. Upon entering the DLD array, the main droplets migrated in displacement mode towards the center wall. As they progressed through the DLD array, the droplets moved out of the nanoparticle stream and into the pure PVA solution. In the downstream region, pure fluorescent precursor droplets were collected via outlet-L, while satellite droplets and excess fluorescent nanoparticles were collected via outlet-S. Photopolymerization produced polymeric microspheres, which exhibited the same fluorescence as the original nanoparticles. Additionally, CLSM imaging confirmed that the nanoparticles were encapsulated within the microspheres. This approach offers a simple and effective protocol for producing fluorescent microspheres, leveraging on-chip functionalization and separation within the DLD arrays.

References

[1] J. H. Kim, T. Y. Jeon, T. M. Choi, T. S. Shim, S. H. Kim, S. M. Yang. Droplet microfluidics for producing functional microparticles. *Langmuir*, **2014**, 30, 1473–1488.

[2] H. Xia, J. Li, J. Man, L. Man, S. Zhang, J. Li. Recent progress in preparation of functional microparticles based on microfluidic technique. *Mater. Today Commun*., **2021**, 29, 102740.

[3] R. Song, S. Cho, S. Shin, H. Kim, J. Lee. From shaping to functionalization of micro-droplets and particles. *Nanoscale Adv.*, **2021**, 3, 3395–3416.

[4] F. Long, Y. Guo, Z. Zhang, J. Wang, Y. Ren, Y. Cheng, G. Xu. Recent progress of droplet microfluidic emulsification based synthesis of functional microparticles. *Global Challenges*, **2023**, 7, 2300063.

[5] S. Iwamoto, K. Nakagawa, S. Sugiura, M. Nakajima. Preparation of gelatin microbeads with a narrow size distribution using microchannel emulsification. *Aaps Pharmscitech*, **2002**, 3, 72–76.

[6] A. M. Chuah, T. Kuroiwa, I. Kobayashi, X. Zhang, M. Nakajima. Preparation of uniformly sized alginate microspheres using the novel combined methods of microchannel emulsification and external gelation. *Colloids Surf. A Physicochem. Eng. Asp.*, **2009**, 351, 9–17.

[7] C. M. Bitar, K. E. Markwick, D. Treľová, Z. Kroneková, M. Pelach, C. M. Selerier, J. Dietrich, Z. Lacík, C. A. Hoesli. Development of a microchannel emulsification process for pancreatic beta cell encapsulation. *Biotechnol. Prog.*, **2019**, 35, e2851.

[8] F. Ikkai, S. Iwamoto, E. Adachi, M. Nakajima. New method of producing mono-sized polymer gel particles using microchannel emulsification and UV irradiation. *Colloid Polym. Sci.*, **2005**, 283, 1149–1153.

[9] A. M. Chuah, T. Kuroiwa, I. Kobayashi, M. Nakajima. Effect of chitosan on the stability and properties of modified lecithin stabilized oil-in-water monodisperse emulsion prepared by microchannel emulsification. *Food Hydrocoll.*, **2009**, 23, 600–610.

[10] D. S. Shin, F. K. Touani, D. G. Aboud, A. M. Kietzig, S. Lerouge, C. A. Hoesli.

Mammalian cell encapsulation in monodisperse chitosan beads using microchannel emulsification. *Colloids Surf. A Physicochem. Eng. Asp.*, **2023**, 661, 130807.

[11] A. Ofner, D. G. Moore, P. A. Rühs, P. Schwendimann, M. Eggersdorfer, E. Amstad, D. A. Weitz, A. R. Studart. High-throughput step emulsification for the production of functional materials using a glass microfluidic device. *Macromol. Chem. Phys.*, **2017**, 218, 1600472.

[12] M. A. Neves, H. S. Ribeiro, I. Kobayashi, M. Nakajima. Encapsulation of lipophilic bioactive molecules by microchannel emulsification. *Food Biophys.*, **2008**, 3, 126–131.

[13] M. A. Neves, H. S. Ribeiro, K. B. Fujiu, I. Kobayashi, M. Nakajima. Formulation of controlled size PUFA-loaded oil-in-water emulsions by microchannel emulsification using β-carotene-rich palm oil. *Ind. Eng. Chem. Res.*, **2008**, 47, 6405–6411.

[14] N. Khalid, I. Kobayashi, M. A. Neves, K. Uemura, M. Nakajima, H. Nabetani. Microchannel emulsification study on formulation and stability characterization of monodisperse oil-in-water emulsions encapsulating quercetin. *Food Chem.*, **2016**, 212, 27–34.

[15] N. Khalid, I. Kobayashi, Z. Wang, M. A. Neves, K. Uemura, M. Nakajima, H. Nabetani. Formulation characteristics of triacylglycerol oil-in-water emulsions loaded with ergocalciferol using microchannel emulsification. *RSC Adv.*, **2015**, 5, 97151–97162.

[16] S. Sugiura, M. Nakajima, K. Yamamoto, S. Iwamoto, T. Oda, M. Satake, M. Seki. Preparation characteristics of water-in-oil-in-water multiple emulsions using microchannel emulsification. *J. Colloid Interface Sci.*, **2004**, 270, 221–228.

[17] M. L. Eggersdorfer, W. Zheng, S. Nawar, C. Mercandetti, A. Ofner, I. Leibacher, S. Koehler, D. A. Weitz. Tandem emulsification for high-throughput production of double emulsions. *Lab Chip*, **2017**, 17, 936–942.

[18] A. Ofner, I. Mattich, M. Hagander, A. Dutto, H. Seybold, P. A. Rühs, A. R. Studart. Controlled massive encapsulation via tandem step emulsification in glass. *Adv. Funct. Mater.*, **2019**, 29, 1806821.

[19] T. Kawakatsu, Y. Kikuchi, M. Nakajima. Regular-sized cell creation in microchannel emulsification by visual microprocessing method. *J. Am. Oil Chem. Soc.*, **1997**, 74, 317–321.

Chapter 4

In-situ external gelation for alginate hydrogel particle synthesis

4.1 Introduction

4.1.1 Alginate hydrogels and applications

Alginate is a well-known natural anionic polymer typically extracted from brown algae such as *Laminaria hyperborea*, *Laminaria digitata*, *Laminaria japonica*, *Ascophyllum nodosum*, and *Macrocystis pyrifera*[1]. Alginate hydrogels can be produced via various chemical or physical cross-linking methods, including ionic cross-linking, covalent cross-linking, and thermal gelation[2]. Among these methods, ionic cross-linking is the most widely used, typically involving the preparation of hydrogels from an aqueous solution with divalent cations as the cross-linking agent. Alginate hydrogels are particularly valuable in biomedical applications due to their three-dimensional cross-linked networks with high water content, which resemble the structure of the macromolecular components in the human body[2]. Alginate has been widely employed in biomedical fields such as pharmaceutical industry[1,2], wound dressing[3,4], cell culture models[5,6], and as a carrier for tissue regeneration[7,8].

4.1.2 Production of alginate hydrogel particles

4.1.2.1 Conventional methods

Various methods have been applied in the production of alginate gels. These methods commonly feature the discrete alginate droplets before the gelation process[9].

Extrusion is a very typical method for the production of alginate hydrogel particles. This method only requires a quite simple operation, which involves pushing the syringe containing alginate solution and dripping the drop into a bath of gelation reagent (**Fig. 4.1a**)[10–12]. For a precise control over the extrusion, this method often takes advantage of centrifugal force, which can be provided by equipping the container of alginate solution with a spinning disk[13–15]. As

shown in **Fig. 4.1b**, a tube with a nozzle at the bottom contained the Na-alginate solution and was equipped on a rotor[13]. With the driven by the rotation, the Na-alginate through the nozzles formed into droplets, and were collected by another tube containing $CaCl_2$ solution for the gelation.

Atomization of alginate solution via spray nozzle is another approach for the production of alginate hydrogels[16–18]. A typical alginate atomization device has a nozzle with the alginate solution flowing inside, while the air flows outside[16]. When the alginate solution exits a nozzle, the air with high pressure causes the atomization of the alginate (**Fig. 4.1c**).

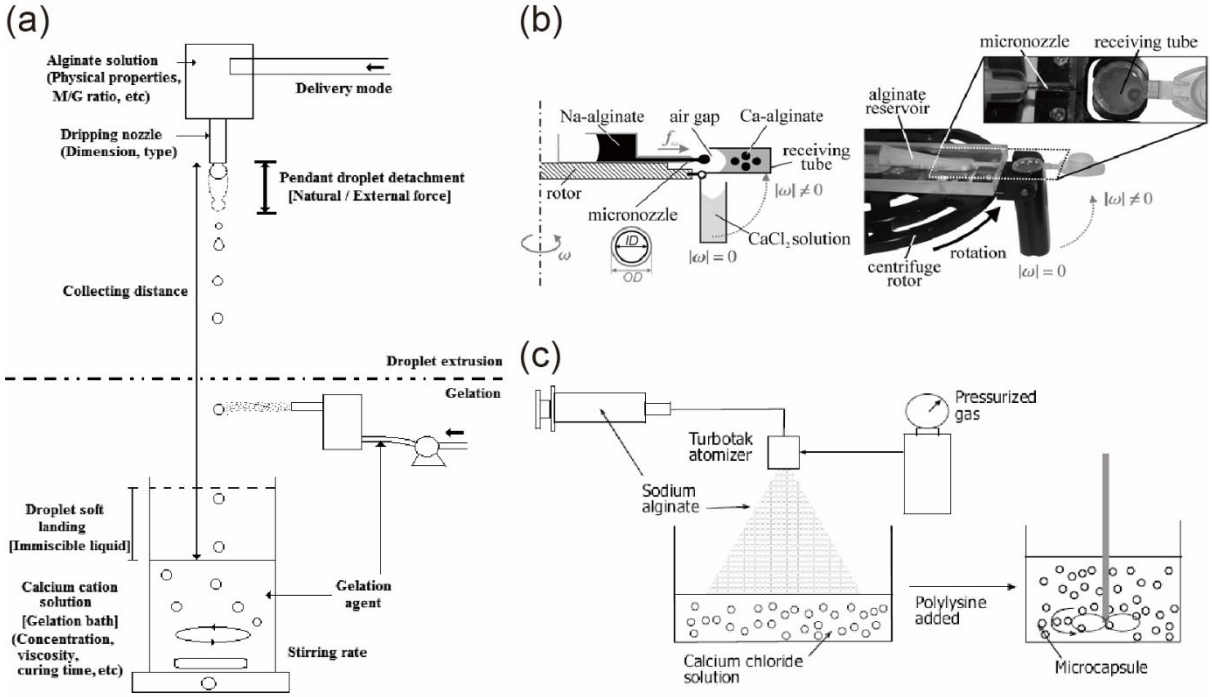

Fig. 4.1 Schematic illustration of production of alginate hydrogels by (a) extrusion[10], (b) centrifugal force[13], and (c) atomization[16]. (a) Reproduced with permission from Wiley-VCH Verlag. (b) Reproduced with permission from Taylor & Francis. (c) Reproduced with permission from Springer.

4.1.2.2 Microfluidic methods

Alginate hydrogel particles with microscale or nanoscale diameters can be produced via microfluidics, a process that has been extensively studied[19–22]. Droplet-based microfluidic methods, as introduced in **Chapter 1**, are first used to produce precursor droplets of the hydrogel particles, allowing for precise control over particle size[23–25]. The gelation of alginate

droplets is then performed to form the hydrogel particles, which can be achieved through either internal gelation[26–28] or external gelation[29–35].

(a) Internal gelation

Internal gelation of alginate gels in microfluidics refers to the methods, which produce precursor alginate droplets encapsulating the insoluble salts. By adjusting the liquid containing the alginate droplets, the ions are released and the gelation is performed in the droplets[26–28]. In particular, Bitar et al. proposed a production of alginate microcapsules by internal gelation via step emulsification (**Fig. 4.2a**)[28]. A mixture of aqueous Na-alginate solution, CaCO3 suspension, and cell suspension was used as the dispersed phase, while an oil mixed with glacial acetic acid was used as the continuous phase. Following the formation at the nozzles, the precursor droplets were collected in a vessel for gelation by the released ions.

(b) External gelation

External gelation refers to the method, of which the ions are supplied from outside of the precursor droplets[29–35]. For example, a production of alginate hydrogel particles by an external approach has been reported by Chuah et al., who used a step emulsification device to produce the Na-alginate precursor droplets (**Fig. 4.2b**)[32]. In this research, the alginate emulsions were formed via through holes of a step emulsification device, which was similar as the process introduced in **Chapter 1**. Next, a $CaCl_2$ solution was added into the alginate emulsions to trigger the gelation.

Besides the commonly used ion bath for external gelation, Tottori et al. proposed a deterministic lateral displacement (DLD)-based external gelation[33]. This approach utilized the lateral migration of particles across the DLD pillars, which has been demonstrated and applied in labeling cells by Morton et al.[34]. As shown in **Fig. 4.3**, the Na-alginate droplets formed at a cross-junction flowed across an emulsion stream containing divalent calcium ions (Ca^{2+}). In further studies, Tottori et al. proposed the on-chip dispersion medium exchange of the Ca-alginate suspension from the oil phase to the water phase[35–37].

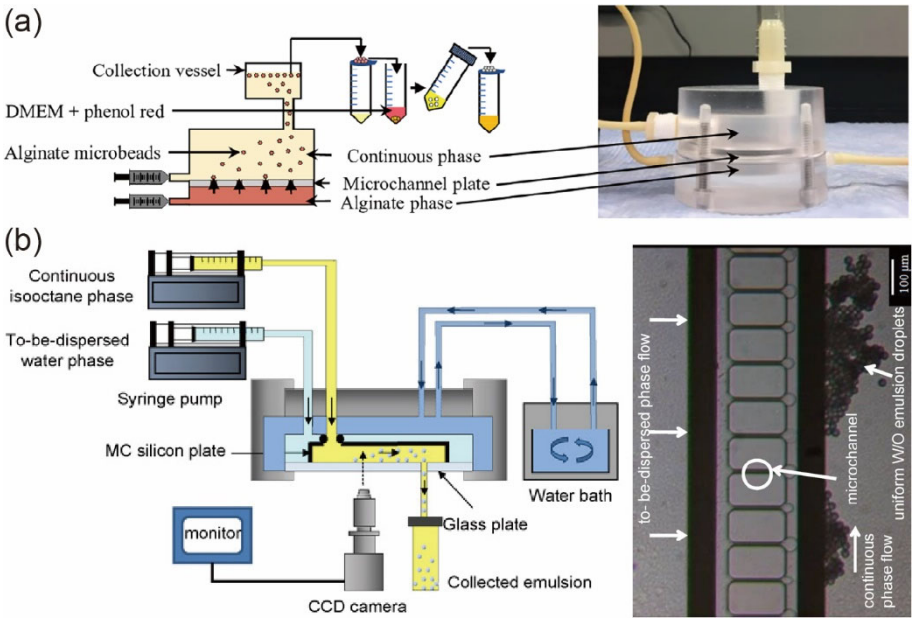

Fig. 4.2 Schematic illustration of production of alginate hydrogels via step emulsification by (a) internal gelation[28] and (b) external gelation[32]. (a) Reproduced with permission from Wiley. (b) Reproduced with permission from Elsevier.

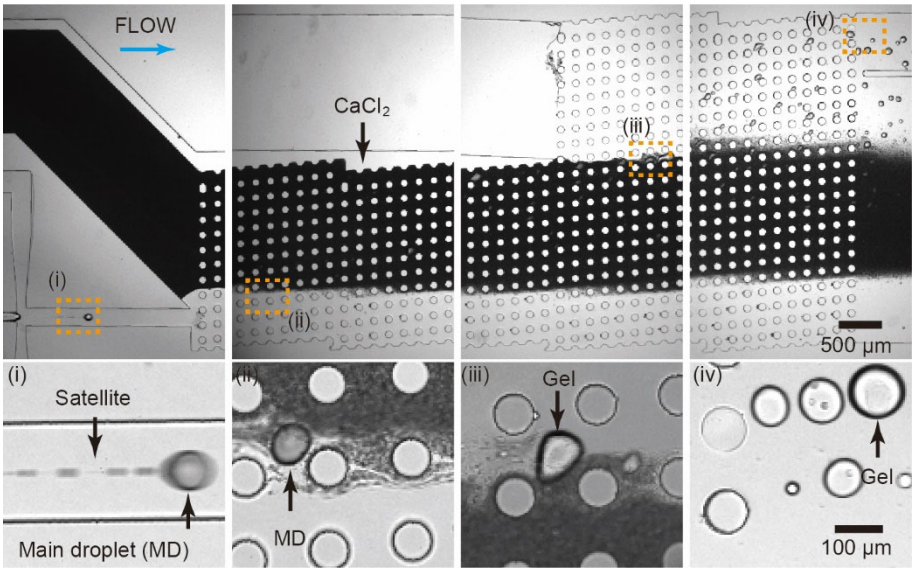

Fig. 4.3 Production of Ca-alginate hydrogel particles by external gelation in DLD array[33]. Reproduced with permission from Chemical and Biological Microsystems Society.

4.1.3 Objective

In this chapter, the advanced processing of Ca-alginate hydrogel particles via step-emulsification and DLD array is demonstrated. The step-emulsification nozzles in the upstream

region produce Na-alginate droplets, while the DLD micropillar arrays in the downstream region contain streams of the $CaCl_2$ emulsion for gelation and glycerol aqueous solution for solution exchange, which has never been reported by other group. As the Na-alginate droplets migrate through the DLD micropillars in bump mode, gelation occurs in the $CaCl_2$ emulsion, and the resulting Ca-alginate hydrogel particles flow into the glycerol aqueous solution in the DLD array, which has never been reported by other group. Finally, the hydrogel particles are collected and characterized.

4.1.4 Outline of this chapter

Section 4.1 Introduction

Introduces the applications of alginate hydrogels and their production via microfluidics.

Section 4.2 Materials and methods

Describes the microfluidic devices used in this chapter, their fabrication, and the peripheral equipment.

Section 4.3 Results and discussion

Presents the results of droplet generation and migration, followed by a demonstration of on-chip gelation.

Section 4.4 Conclusion

Summarizes the conclusions of this chapter.

4.2 Materials and methods

4.2.1 Device design and mechanism

A microfluidic device incorporating step-emulsification nozzles and DLD micropillar arrays was developed for the formation of Na-alginate droplets and on-chip gelation of Ca-alginate hydrogel particles (**Fig. 4.4a**). The device consists of three sections, a droplet generation section in the upstream region, a gelation region in the downstream, and a solution-exchange region adjacent to the gelation region. The droplet generation region features three step-emulsification nozzles connected to a straight channel for generating the Na-alginate droplets. The inner and opening widths of the step-emulsification nozzles are 35 μm and 175 μm, respectively, with nozzle and channel heights of 9 μm and 90 μm (**Fig. 4.4b**). Downstream, a DLD micropillar array with a critical diameter (D_c) of 37 μm is used for the gelation of the main droplets. The gap width and diameter of each micropillar are 80 μm and 100 μm, respectively, resulting in a pitch (λ) of 180 μm and a vertical shift ($\Delta\lambda$) of 18 μm (**Fig. 4.4c**). This DLD array comprises 10 columns with 18 micropillars each, repeated 20 times. Similar as the previous chapters, the gap sizes close to the DLD boundary were also midified as introduced in **Chapter 1**. The modified gap sizes are shown in **Table 4-1**, of which G_{ns} and G_{nl} are the gap size of n-th gap close to the walls with and without nozzles, respectively.

Table 4-1 Sizes of the gaps close to DLD boundary.

Gap #	G_{ns} (μm)	G_{nl} (μm)	Gap #	G_{ns} (μm)	G_{nl} (μm)
1	25	110	6	62	95
2	36	107	7	67	91
3	44	104	8	72	88
4	51	101	9	76	84
5	57	98	10	80	80

Three channels—one for the Na-alginate droplets, one for the $CaCl_2$ emulsion, and one for the oil phase—connect to the DLD array. The solution-exchange region contains a smaller DLD micropillar array with only 10 pillars per column and six repeats. An inlet before this DLD

array facilitates solution exchange. The two DLD arrays are aligned in parallel, separated by a wall (length: ~5.4 mm, width: 100 μm) to direct Ca-alginate hydrogel particles and the $CaCl_2$ emulsion to separate outlets.

The mechanism of this device is illustrated in **Fig. 4.4a**. The dispersed and continuous phases are separately infused into the droplet generation region, where Na-alginate droplets form at the three nozzles. These droplets then enter the downstream DLD region, where three streams—containing Na-alginate droplets, $CaCl_2$ emulsion, and pure oil flow—flow through the DLD micropillar array. Since the main alginate droplets are larger than the D_c of the DLD array, they migrate in bump mode, sequentially passing through the continuous phase, $CaCl_2$ emulsion, and pure oil streams. During migration through the $CaCl_2$ emulsion stream, small $CaCl_2$ droplets contact the alginate droplets, allowing Ca^{2+} ions to diffuse into the droplets and trigger the formation of Ca-alginate hydrogels. The width of the $CaCl_2$ emulsion stream, and thus the reaction time, can be controlled by adjusting the flow rates of the $CaCl_2$ emulsion and the oil. The Ca-alginate hydrogel particles migrate out of the gelation region into the solution-exchange region, where they are collected in the exchange solution via outlet-L.

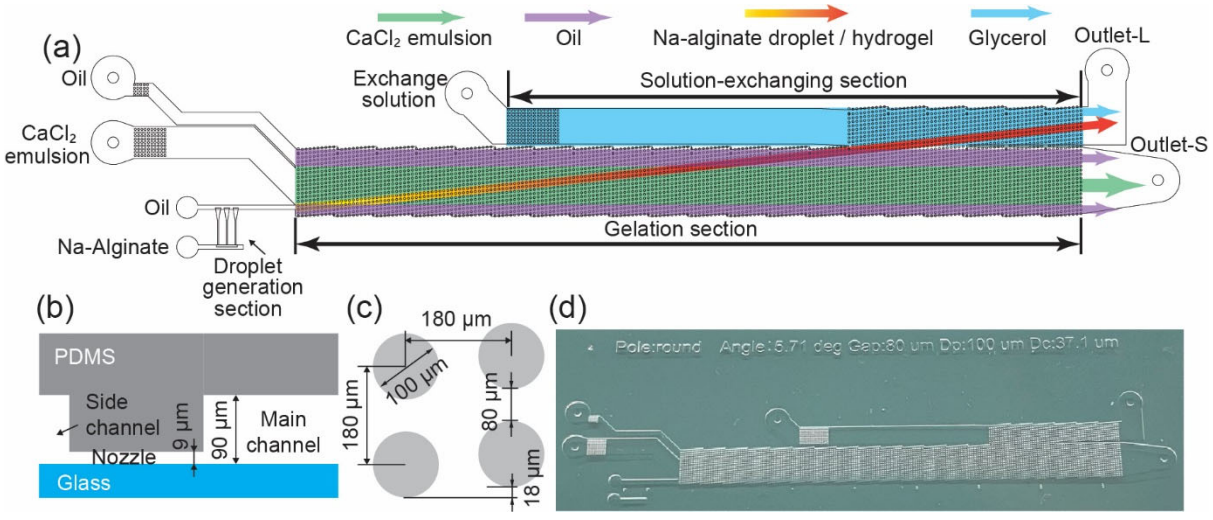

Fig. 4.4 (a) Schematic illustrations of the microfluidic devices. Droplets are formed at the three nozzles in the upstream region. As they migrate through the DLD array, the main droplets pass through the $CaCl_2$ emulsion for gelation, continue into the glycerol solution, and are then collected. Size parameters of (b) the step-emulsification nozzle and (c) the DLD array. (d) A PDMS chip of the device.

4.2.2 Device fabrication

The microfluidic devices were fabricated using PDMS via standard soft lithography (**Fig. 4.4d**). The fabrication process involved photolithography of the SU-8 mold, casting of the PDMS replica, sealing onto a plain PDMS substrate, and hydrophilic surface modification, following the procedures outlined in **Chapter 2**. The SU-8 mold for the step-emulsification section on a silicon wafer has a height of 9 μm. The height of the DLD section and other channels is 90 μm.

4.2.3 Chemicals

An oleic acid containing 1 wt% surfactant (SY-Glyster 75) with the viscosity of ~38 mPa·s was prepared for the continuous phase. A 3 wt% Na-alginate aqueous solution with the viscosity of ~1500 mPa·s was prepared for the dispersed phase. A 30 wt% $CaCl_2$ aqueous solution and an oleic acid containing 0.1 wt% surfactant (SY-Glyster 75) were prepared to produce the $CaCl_2$ emulsion. An 80 wt% glycerol aqueous solution was prepared for the exchange solution. The production information of the chemicals is presented in **Appendix A.2.2**. The chemicals used are listed in **Table 4-2**.

Table 4-2 Chemicals used.

Continuous phase	Oleic acid
Dispersed phase	3 wt.% Na-alginate aqueous solution
Exchanging solution	80 wt.% Glycerol
Emulsion	
Water phase	30 wt.% $CaCl_2$ aqueous solution
Oil phase	Oleic acid with 0.1 wt.% SY-Glyster 75

4.2.4 Equipment

The agents contained in syringes are driven into the device by syringe pumps, as listed in **Table 4-3**. A microscope equipped with a high-speed camera is used to observe droplet

formation and migration. The droplets are analyzed using ImageJ software. The production information of the equipment is presented in **Appendix A.3**.

Table 4-3 Syringes and syringe pumps.

Syringe	Contents
Gas-tight glass (0.5 mL)	Na-alginate solution
Gas-tight glass (10 mL) x 3	Oleic acid x 2
	$CaCl_2$ emulsion
Plastic (50 mL)	Glycerol solution
Syringe pumps	Legato 180 x 2
	Legato 200
	KDS 210 x 2

4.2.5 Preparation of $CaCl_2$ emulsion

The water-in-oil emulsion containing small $CaCl_2$ solution droplets was produced using a homogenizer (T10 basic ULTRA-TURRAX, IKA, Germany). A mixture of 15 g $CaCl_2$ aqueous solution and 42 g oleic acid with 0.1 wt.% surfactant was placed in a disposable cup. The mixture was homogenized at 30,000 rpm for 3 minutes, resulting in emulsions with diameters of 2–6 μm (n = 100).

4.3 Results and discussion

4.3.1 Droplet formation in step emulsification nozzles

The formation of Na-alginate droplets at the step-emulsification nozzles was initially investigated. The flow rates of the Na-alginate solution, oleic acid (as the continuous phase), pure oleic acid, and glycerol solution were set at 0.001 mL/h, 1.5 mL/h, 3.0 mL/h, and 1.0 mL/h, respectively. The emulsion was not introduced until a stable formation of Na-alginate droplets was observed. Droplets were generated one by one at the three nozzles, with a total generation rate of only 4 drops/s (**Fig. 4.5a**). The mean diameter of the droplets before entering the DLD array was approximately 68 μm, with a CV of 8.5% (**Fig. 4.5b**), indicating suboptimal monodispersity.

Compared to the droplet formation in step-emulsification nozzles discussed in previous chapters, the formation in these nozzles exhibited notable differences. A long neck between the tongue-shaped tip and the dispersed phase was observed before droplet break-up, and droplets detached inside the straight channel rather than at the nozzle tips. Additionally, it was noted that the third nozzle produced smaller droplets, further compromising monodispersity. This discrepancy may be due to the low flow rate of the dispersed phase through the nozzle, whose entrance was clogged by undesired rubbish.

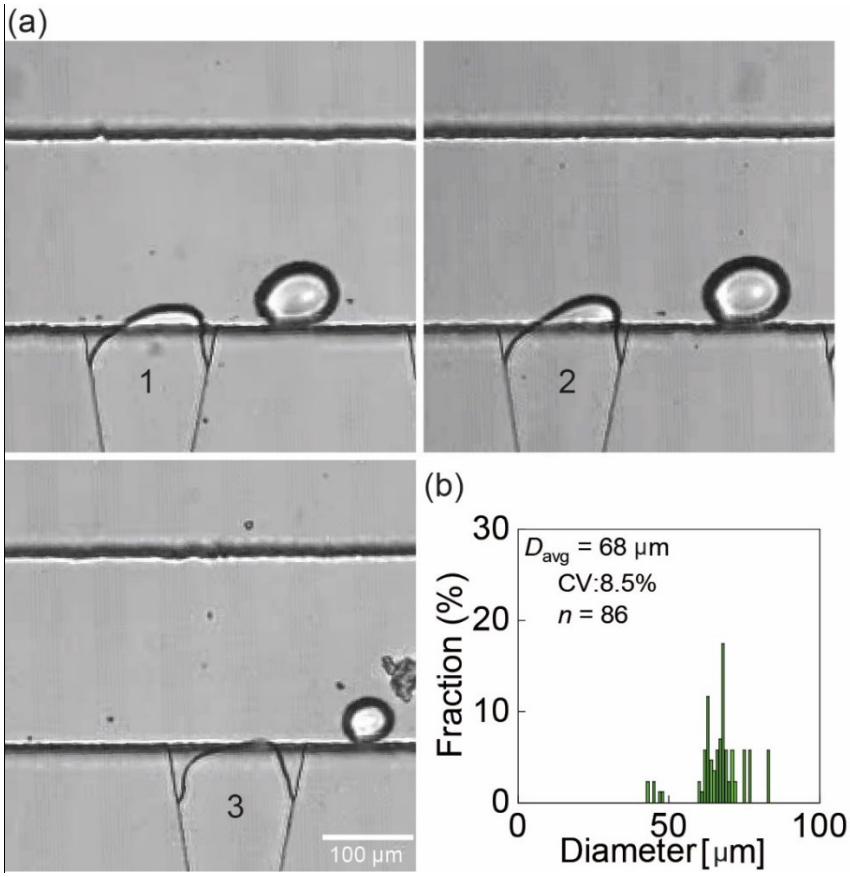

Fig. 4.5 (a) Formation of droplets at the step-emulsification nozzles. Nozzle 1 and 2 produced droplets of similar size, while Nozzle 3 produced smaller droplets. (b) Size distribution of the droplets. The droplets have a mean diameter of 68 μm and the CV of 8.5%.

4.3.2 Migration and gelation of droplets

After entering the DLD array near the sidewall, the main droplets migrated with bump mode through the pillars based on their sizes. The flow rate of the $CaCl_2$ emulsion was set at 2.0 mL/h. With the flow rate conditions, the 1st – 3rd and 13th – 17th gaps were filled with the oil stream, while the $CaCl_2$ emulsion flowed through the 4th – 12th gaps. The droplets firstly flowed in the oil stream laterally through the DLD gaps (**Fig. 4.6a**). Subsequently, the droplets out of the oil stream flowed into the emulsion stream for the gelation (**Fig. 4.6b**). After flowing in the emulsion for ~ 2 seconds, in the midstream region, we observed that droplets flowed out of the emulsion and migrated in the pure oil stream (**Fig. 4.6c**). Then, the droplets entered the DLD array in the solution-exchanging region and flowed towards the outlet-L. Clog of the hydrogels in the DLD array was also observed (**Fig. 4.6c**). The migration of the Na-alginate

droplets and the Ca-alginate hydrogel particles were also demonstrated in the magnified views. As shown in **Fig. 4.6d** and **Fig. 4.6e**, the migration of the alginate droplet in the emulsion and the hydrogel was observed. Meanwhile, droplets much larger than the hydrogel particles were also observed. These droplets might be the coalescence of the $CaCl_2$ droplets in the emulsion (**Fig. 4.6f**).

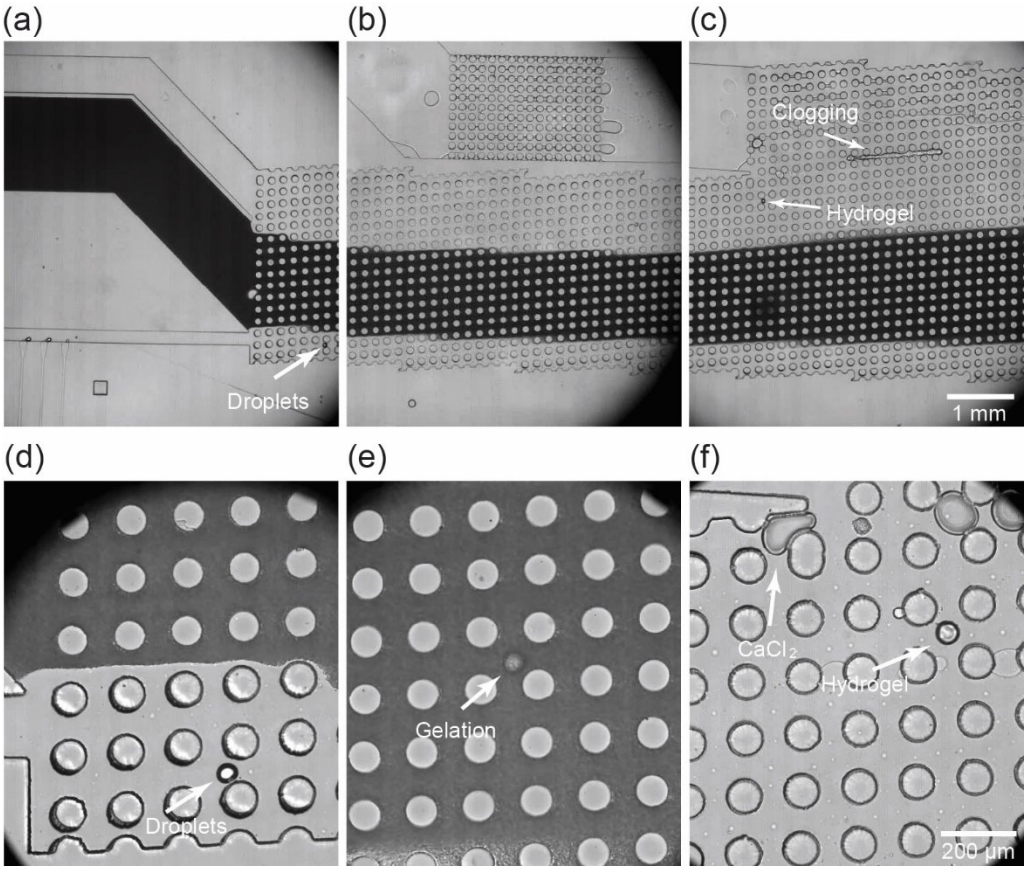

Fig. 4.6 (a) Migration of the Na-alginate droplet in the continuous phase in the upstream region. (b) The alginate droplets flowing in the $CaCl_2$ emulsion. (c) Hydrogel particles and hydrogel clogging after exiting the emulsion stream. Magnified views of (d) the Na-alginate droplet before entering the emulsion, (e) Gelation of the Na-alginate droplet, and (f) A hydrogel particle and coalescence of $CaCl_2$ droplets exiting the emulsion.

4.3.3 Characterization of hydrogel particles

The hydrogel particles, gelled by the $CaCl_2$ emulsion via the DLD array, were collected in an empty petri dish for size measurement (**Fig. 4.7a**). No $CaCl_2$ emulsion, which appears black under the monochrome high-speed camera, was observed in the collected sample, confirming

successful solution exchange via the DLD array. The collected hydrogel particles were polydisperse, with diameters ranging from 29 to 126 μm and a CV of 25.3% (n = 183, **Fig. 4.7b**). The larger hydrogels may result from the coalescence of Na-alginate droplets or hydrogels, while the smaller hydrogels could be due to the break of coalesced droplets before complete gelation. The shapes of the hydrogel particles, influenced by the surfactant concentration in the emulsion and the fraction of the $CaCl_2$ aqueous solution[21], were also shown in **Fig. 4.7**. Most hydrogel particles were round or elliptical with distinct boundaries, though a small fraction exhibited distorted shapes or formed large gel blocks of multiple particles without clear boundaries (**Fig. 4.7a**). Elliptical-shaped hydrogel particles suggest insufficient gelation within the DLD array, possibly due to the instability in the $CaCl_2$ emulsion.

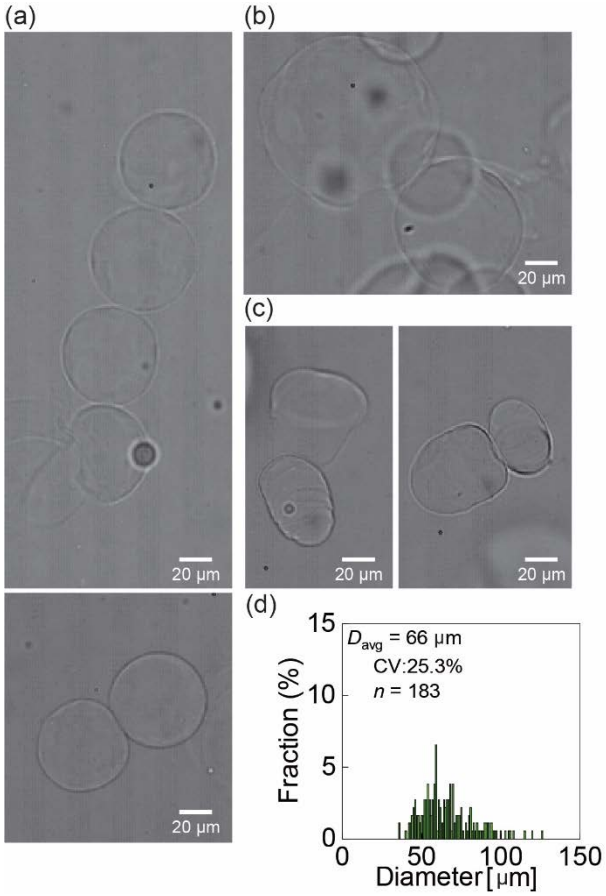

Fig. 4.7 (a) Monodisperse Ca-alginate hydrogel particles with a mean diameter of ~ 66 μm. (b) Large hydrogel particles. (c) Elliptical hydrogel particles. (d) Size distribution of the hydrogel particles, showing a mean diameter of ~ 66 μm and a CV of 25.3%.

4.3.4 Discussion

This study demonstrated a method for producing pure Ca-alginate hydrogel particles via on-chip gelation and solution exchange in DLD micropillar arrays. Similar to the device in **Chapter 5**, the DLD arrays in this study functioned as both a separator for sorting the droplets and a reactor for the gelation of the Na-alginate droplets. This approach enables the production of pure Ca-alginate hydrogel particles without the need for off-chip washing, simplifying the process. However, the hydrogel particles were found to be polydisperse with various shapes, limiting their applicability. To address this issue, an improvement could be made: increasing the surfactant concentration in the emulsion to maintain a stable and even distribution of small $CaCl_2$ droplets in the DLD array.

4.4 Conclusion

This chapter demonstrated an advanced on-chip approach to produce pure Ca-alginate hydrogel particles using DLD micropillar arrays. The device, equipped with three step-emulsification nozzles and DLD micropillar arrays with a D_c of 37 μm, successfully generated Na-alginate droplets with a mean diameter of 68 μm in the upstream region. After entering the DLD micropillar array, these droplets, having a diameter larger than D_c, sequentially migrated across streams of continuous phase, $CaCl_2$ emulsion, and pure oil. Following solution exchange within the DLD array, the Ca-alginate hydrogel particles suspended in the glycerol aqueous solution were collected. The hydrogel particles were polydisperse (CV: 25.3%), indicating a need for further improvement. Nevertheless, this study proposed a simple advanced approach for the production of pure alginate hydrogel particles via on-chip reaction in DLD micropillar arrays, using a single microfluidic device. We believe this approach holds promise for the continuous production of hydrogels and various other polymers.

References

[1] O. Smidsrød, G. Skja. Alginate as immobilization matrix for cells. *Trends Biotechnol.*, **1990**, 8, 71–78.

[2] K. Y. Lee, D. J. Mooney. Alginate: properties and biomedical applications. *Prog. Polym. Sci.*, **2012**, 37, 106–126.

[3] R. Parhi. Cross-linked hydrogel for pharmaceutical applications: a review. *Adv. Pharm. Bull.*, **2017**, 7, 515–530.

[4] M. Szekalska, A. Puciłowska, E. Szymańska, P. Ciosek, K. Winnicka. Alginate: current use and future perspectives in pharmaceutical and biomedical applications. *Int. J. Polym. Sci.*, **2016**, 2016, 7697031.

[5] Y. Cao, H. Cong, B. Yu, Y. Shen. A review on the synthesis and development of alginate hydrogels for wound therapy. *J. Mater. Chem. B*, **2023**, 11, 2801–2829.

[6] M. Zhang, X. Zhao. Alginate hydrogel dressings for advanced wound management. *Int. J. Biol. Macromol.*, **2020**, 162, 1414–1428.

[7] T. Andersen, P. Auk-Emblem, M. Dornish. 3D cell culture in alginate hydrogels. *Microarrays*, **2015**, 4, 133–161.

[8] S. M. Kang, J. H. Lee, Y. S. Huh, S. Takayama. Alginate microencapsulation for three-dimensional in vitro cell culture. *ACS Biomater. Sci. Eng.*, **2020**, 7, 2864–2879.

[9] S. H. Ching, N. Bansal, B. Bhandari. Alginate gel particles–A review of production techniques and physical properties. *Crit. Rev. Food Sci. Nutr.*, **2017**, 57, 1133–1152.

[10] B. B. Lee, P. Ravindra, E. S. Chan. Size and shape of calcium alginate beads produced by extrusion dripping. *Chem. Eng. Technol.*, **2013**, 36, 1627–1642.

[11] S. Lević, I. P. Lijaković, V. Đorđević, V. Rac, V. Rakić, T. Š. Knudsen, V. Pavlovi, B. Bugarski, V. Nedović. Characterization of sodium alginate/d-limonene emulsions and respective calcium alginate/d-limonene beads produced by electrostatic extrusion. *Food Hydrocoll.*, **2015**, 45, 111–123.

[12] H. Bokkhim, N. Bansal, L. Grøndahl, B. Bhandari. Characterization of alginate–lactoferrin beads prepared by extrusion gelation method. *Food Hydrocoll.*, **2016**, 53,

270–276.

[13] S. Haeberle, L. Naegele, R. Burger, F. V. Stetten, R. Zengerle, J. Ducree. Alginate bead fabrication and encapsulation of living cells under centrifugally induced artificial gravity conditions. *J. Microencapsul.*, **2008**, 25, 267–274.

[14] H. Onoe, K. Inamori, M. Takinoue, S. Takeuchi. Centrifuge-based cell encapsulation in hydrogel microbeads using sub-microliter sample solution. *RSC Adv.*, **2014**, 4, 30480–30484.

[15] S. M. Kang, G. W. Lee, Y. S. Huh. Centrifugal force-driven modular micronozzle system: generation of engineered alginate microspheres. *Sci. Rep.*, **2019**, 9, 12776.

[16] Y. Yeo, N. Baek, K. Park. Microencapsulation methods for delivery of protein drugs. *Biotechnol. Bioprocess Eng.*, **2001**, 6, 213–230.

[17] K. K. Kwok, M. J. Groves, D. J. Burgess. Production of 5–15 μm diameter alginate-polylysine microcapsules by an air-atomization technique. *Pharm. Res.*, **1991**, 8, 341–344.

[18] S. M. Abraham, R. F. Vieth, D. J. Burgess. Novel technology for the preparation of sterile alginate-poly-l-lysine microcapsules in a bioreactor. *Pharm. Dev. Technol.*, **1996**, 1, 63–68.

[19] C. Zhang, R. Grossier, N. Candoni, S. Veesler. Preparation of alginate hydrogel microparticles by gelation introducing cross-linkers using droplet-based microfluidics: a review of methods. *Biomater. Res.*, **2021**, 25, 41.

[20] A. Moreira, J. Carneiro, J. B. M. Campos, J. M. Miranda. Production of hydrogel microparticles in microfluidic devices: a review. *Microfluid. Nanofluid.*, **2021**, 25, 1–24.

[21] Z. Wei, S. Wang, J. Hirvonen, H. A. Santos, W. Li. Microfluidics fabrication of micrometer-sized hydrogels with precisely controlled geometries for biomedical applications. *Adv. Healthc. Mater.*, **2022**, 11, 2200846.

[22] C. B. Goy, R. E. Chaile, R. E. Madrid. Microfluidics and hydrogel: A powerful combination. *React. Funct. Polym.*, **2019**, 145, 104314.

[23] L. Nan, H. Zhang, D. A. Weitz, H. C. Shum. Development and future of droplet microfluidics. *Lab Chip*, **2024**, 24, 1135–1153.

[24] P. Zhu, L. Wang. Passive and active droplet generation with microfluidics: a review. *Lab*

Chip, **2017**, 17, 34–75.

[25] W. Han, X. Chen. A review on microdroplet generation in microfluidics *J. Braz. Soc.* **2021**, 43, 247.

[26] S. Akbari, T. Pirbodaghi. Microfluidic encapsulation of cells in alginate particles via an improved internal gelation approach. *Microfluid. Nanofluid.*, **2014**, 16, 773–777.

[27] N. Paiboon, S. Surassmo, U. R. Ruktanonchai, M. Kappl, A. Soottitantawat. Internal gelation of alginate microparticle prepared by emulsification and microfluidic method: Effect of Ca-EDTA as a calcium source. *Food Hydrocoll.*, **2023**, 141, 108712.

[28] C. M. Bitar, K. E. Markwick, D. Treľová, Z. Kroneková, M. Pelach, C. M. Selerier, J. Dietrich, I. Lacík, C. A. Hoesli. Development of a microchannel emulsification process for pancreatic beta cell encapsulation. *Biotechnol. Prog.*, **2019**, 35, e2851.

[29] Y. Liu, N. Tottori, T. Nisisako. Microfluidic synthesis of highly spherical calcium alginate hydrogels based on external gelation using an emulsion reactant. *Sens. Actuators B: Chem.*, **2019**, 283, 802–809.

[30] S. Sugiura, T. Oda, Y. Izumida, Y. Aoyagi, M. Satake, A. Ochiai, N. Ohkohchi, M. Nakajima. Size control of calcium alginate beads containing living cells using micro-nozzle array. *Biomaterials*, **2005**, 26, 3327–3331.

[31] L. Capretto, S. Mazzitelli, C. Balestra, A. Tosi, C. Nastruzzi. Effect of the gelation process on the production of alginate microbeads by microfluidic chip technology. *Lab Chip*, **2008**, 8, 617–621.

[32] A. M. Chuah, T. Kuroiwa, I. Kobayashi, X. Zhang, M. Nakajima. Preparation of uniformly sized alginate microspheres using the novel combined methods of microchannel emulsification and external gelation. *Colloids Surf. A Physicochem. Eng. Asp.*, **2009**, 351, 9–17.

[33] N. Tottori, Y. Liu, T. Nisisako. Functional particles design using deterministic lateral displacement. *Proc. Micro Total Anal. Syst.* **2018**, 4, 2181–2182.

[34] K. J. Morton, K. Loutherback, D. W. Inglis, O. K. Tsui, J. C. Sturm, S. Y. Chou, R. H. Austin. Crossing microfluidic streamlines to lyse, label and wash cells. *Lab Chip*, **2008**, 8, 1448–1453.

[35] 鳥取直友，西迫貴志　マイクロピラーアレイを用いたハイドロゲル微粒子の生成と溶液置換.　2019 年度精密工学会秋季大会講演論文集，**2019**, 279–280.

[36] 鳥取直友，西迫貴志　マイクロピラーアレイを用いたアルギン酸カルシウムゲル粒子の連続生成. 化学とマイクロ・ナノシステム学会第 40 回研究会，**2019**, 4P14.

[37] N. Tottori, T. Nisisako. Continuous generation of cell-laden microgels through deterministic lateral displacement arrays. *Proc. Micro Total Anal. Syst.* **2020**, 4, 108–109.

Chapter 5

Mitigation of droplet accumulation through pillar-assisted nozzle design

5.1 Introduction

5.1.1 Droplet accumulation near step emulsification nozzles

In **Chapter 2**, various microfluidic methods for droplet production were introduced, with a general explanation of the droplet formation mechanisms within the droplet makers. In shear-induced methods such as co-flow, cross-flow, and flow-focusing geometries, the continuous phase applies the shear force on the dispersed phase as it enters the junction, causing the liquid tip of the dispersed phase to break up, forming droplets. Additionally, the continuous phase transports the generated droplets toward the outlet. In contrast, in step emulsification, droplets form due to the gradient of Laplace pressure, which is primarily governed by the geometry of the droplet maker[1,2]. Here, the continuous phase is typically responsible for cleaning the droplet formation area and carrying the droplets out of the device[2].

Chapter 2 also highlighted the issue of droplet coalescence, which occurs due to the accumulation of droplets (> 4220 drops/mm^3) in the downstream region of the step-emulsification nozzles. The droplets tend to stack near the nozzle exits, leading to dense accumulation and eventual coalescence, which compromises the monodispersity of the product However, previous research on step emulsification has rarely addressed droplet interactions, including accumulation and coalescence[3,4]. Nakajima et al. first introduced microchannel (step) emulsification in 1997[5], and later, Sugiura et al. identified the production of larger droplets caused by dropletstacking[3]. In emulsification processes, applying high pressure to the dispersed phase often leads to a shortage of the continuous phase, which hampers droplet transport towards the exit, disturbs the continuous phase, and ultimately results in larger droplet formation and continuous flow of the dispersed phase (**Fig. 5.1a**). Additionally, Mittal et al. observed collisions between droplets during step

emulsification could lead to either the formation of smaller droplets or coalescence[4]. Their study on the dynamics of step emulsification revealed two possible outcomes of droplet collisions. A head-on collision between a formed droplet and the growing tip of the dispersed phase can induce tip fragmentation, resulting in smaller droplets. Conversely, in the regime where large droplets are generated, a glancing collision between a droplet and the growing tip can stretch the neck between the tongue-shaped tip and the disperse phase (**Fig. 5.1b**).

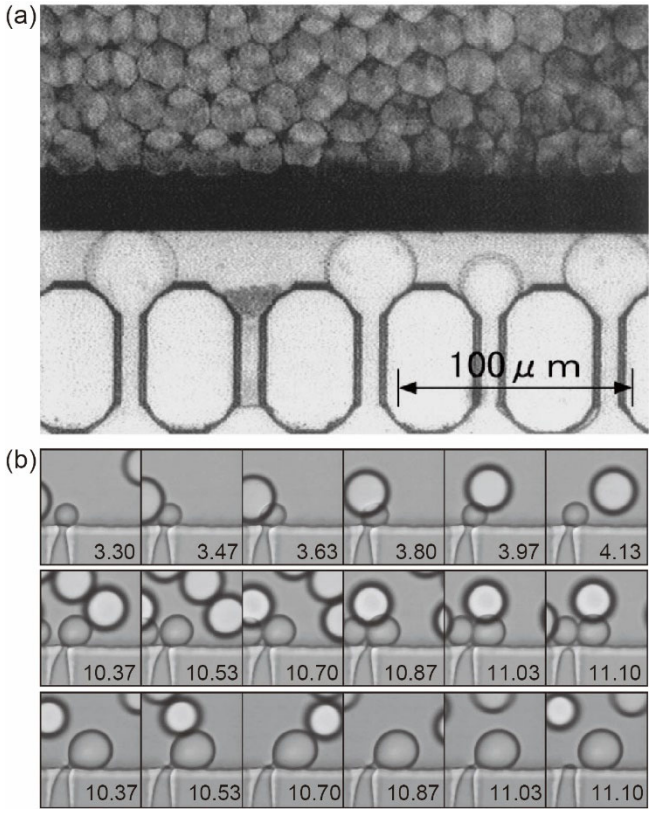

Fig. 5.1 (a) Accumulation of droplets near the step-emulsification nozzles, leading to the formation of large droplets[3]. (b) Time sequence showing the formation of a large droplet in 11.10 ms after a glancing collision between a flowing droplet and the growing tip of the dispersed phase[4]. (a) Reproduced with permission from Elsevier. (b) Reproduced with permission from American Institute of Physics.

5.1.2 Improvement of droplet accumulation

Droplet accumulation near the nozzles can lead to undesirable outcomes, such as polydisperse products and even continuous flow of the dispersed phase. Despite its significance, research specifically addressing the issue of droplet accumulation remains

limited. Several centrifugal step emulsification devices have been proposed, which produced the droplets without droplet accumulation near the step emulsifiers[6–9]. For example, Schuler et al. reported a production of water droplets via centrifugal step emulsification nozzles on a disk (**Fig. 5.2a**), where the water driven by the centrifugal force flowed across the nozzles and formed droplets in the fluorinated oil[6]. Due to the density difference, the buoyancy lifted the water emulsions, cleaning the area near the nozzles. The utilization of buoyancy to improve the accumulation of droplets in step emulsification was also demonstrated by Stolovicki et al., who reported a polydimethylsiloxane (PDMS) volcano device with 135 step-emulsification nozzles connected to the end of a binary tree-shaped channel for supplying pure water as the dispersed phase (**Fig. 5.2b**)[10]. The device was submerged in oil with the nozzle tips pointing upward. Since HFE 7500, a denser oil phase, was used, the water droplets generated were buoyant and naturally floated to the surface of the oil pool. However, this buoyancy-based method requires the use of a dispersed phase with a lower-density than the continuous phase, which restricts the choice of liquids.

Nongravity-based approaches to improve the droplet accumulation have also been reported. A slope-based method, which has the nozzles ending in collector with a sloping roof, was proposed by Dangla et al.[11]. After the formation at the ends of the nozzles, which have a minimum height of the collector, the droplets migrated spontaneously towards the center of the collector (**Fig.5.3a**). In addition, a recent study demonstrated the horizontal step emulsifiers with the ends along a vertical slit[12]. The droplets formed at the nozzles were driven away these nozzles by the continuous phase through the slit (**Fig.5.3b**).

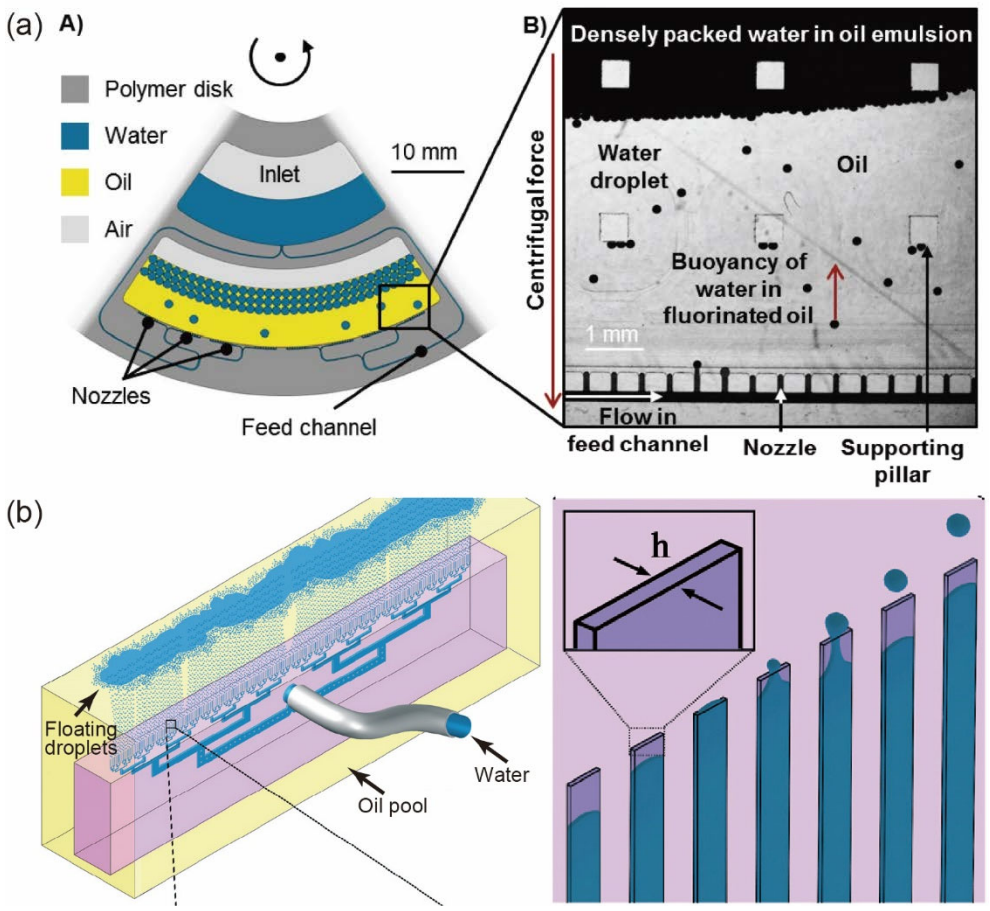

Fig. 5.2 (a) Schematic illustration of centrifugal step emulsifiers, and the droplet migration away the nozzles[6]. (b) Schematic illustration of a volcano device containing 135 step-emulsification nozzles. The nozzle part is submerged in oil with the nozzle tips oriented upward. The generated droplets rise to the oil surface due to buoyancy[10]. (a) Reproduced with permission from Multidisciplinary Digital Publishing Institute. (b) Reproduced with permission from The Royal Society of Chemistry.

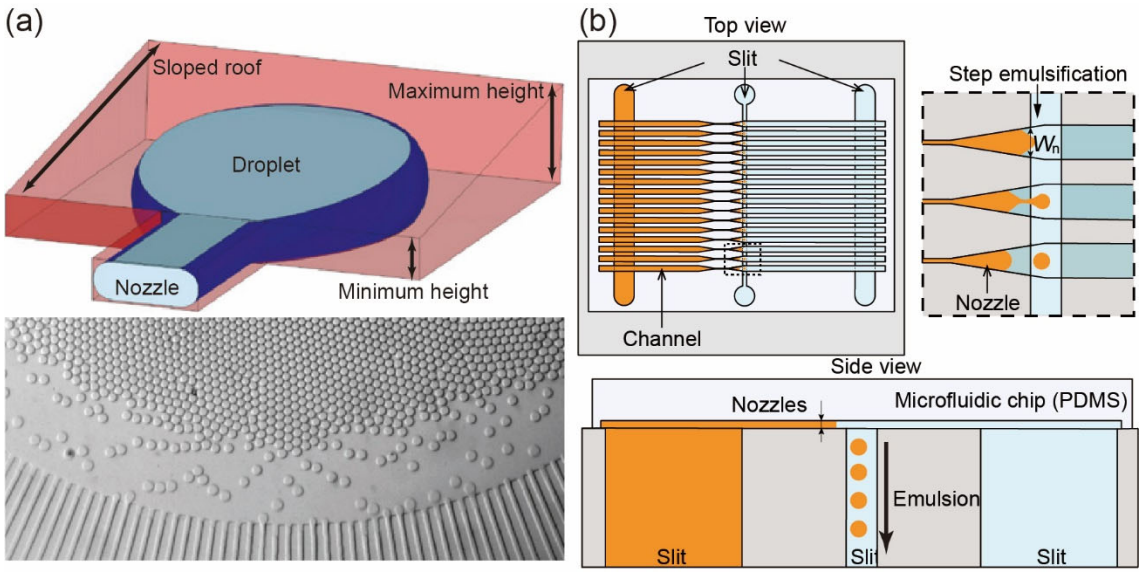

Fig. 5.3 (a) Schematic illustration of nozzle with a sloped roof of the collector, and the formed droplets away from the nozzles[11]. (b) Schematic illustration of the step emulsification nozzles along a slit. The generated emulsions were driven away the nozzles by the continuous phase[12]. (a) Reproduced with permission from National Academy of Sciences, USA. (b) Reproduced with permission from American Chemical Society.

5.1.3 Objective

In this chapter, microfluidic devices having parallel arranged step-emulsification nozzles and a DLD micropillar array are presented as a solution for inhibiting droplet accumulation. The step emulsification nozzles are positioned along the side of the main channel, while the DLD micropillar array is situated within the main channel, with the nozzle tips aligned in the DLD region. The formation of main and satellite droplets at the step emulsification nozzles is first examined. Next, the migration of these droplets through different paths within the DLD micropillar array, based on their sizes, is analyzed. Finally, the extent of droplet accumulation near the step emulsification nozzles is evaluated.

5.1.4 Outline of this chapter

Section 5.1 Introduction

Introduces the problem of droplet accumulation in step emulsification devices.

Section 5.2 Materials and methods

Describes the microfluidic devices used, their fabrication, and the peripheral equipment involved in this study.

Section 5.3 Results and discussion

Presents the results of the droplet generation and the migration of main and satellite droplets, followed by an analysis of droplet accumulation near the step emulsification nozzles.

Section 5.4 Conclusion

Summarizes the key findings of this chapter.

5.2 Materials and methods

5.2.1 Device design and mechanism

Two devices (Device-1 and Device-2) were designed, each combining step-emulsification nozzles and DLD micropillar array (**Fig. 5.4**). Both devices have two upstream inlets for the dispersed and continuous phases. The devices incorporate 100 step-emulsification nozzles arranged perpendicular to the main channel. Unlike the devices discussed in **Chapter 2**, where DLD micropillars were positioned downstream of the step emulsification nozzles, the DLD micropillars in this chapter are aligned along the main channel parallel to the nozzle array. The outlets located downstream of the DLD micropillar array are open for collecting the droplet suspension (**Fig. 5.4a** and **5.4b**).

The step emulsification nozzles in both devices have triangular ends, with a length of 0.8 mm and a depth of 14 μm, connected to the side of the main channel. The pitch between the nozzles is 300 μm. The width of the triangular end increases from 35 μm to 140 μm over a length of 300 μm at an angle of 9.8° (**Fig. 5.4c**).

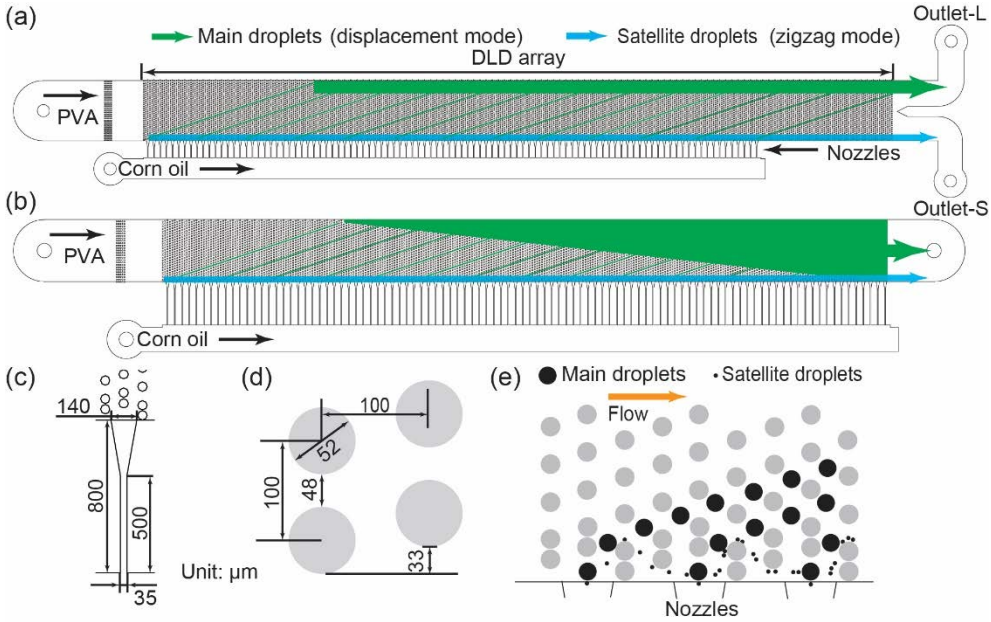

Fig. 5.4 Schematic illustrations of the microfluidic devices used: (a) Device-1 and (b)Device-2. (c) Dimensions of a step-emulsification nozzle. (d) Dimensions of a rhombic DLD cell within the pillar array. (e) Schematic depiction of droplet trajectories through the DLD gaps, where the main droplets follow a displacement mode, and the satellite droplets move in a zigzag mode.

The DLD micropillar arrays in the two devices differ in their arrangement. In Device-1, the DLD micropillar array, with a height of 109 μm, starts at the same position as the step-emulsification nozzle array in the direction of flow. The array consists of 122 repeated DLD regions extending towards the outlet. Each DLD region contains 29 row gaps perpendicular to the flow and 3 pillar columns aligned with the flow direction. The centers of the third column in the first 100 DLD regions correspond to the centers of the first to 100th step-emulsification nozzles. The remaining 22 DLD regions allow sufficient displacement of the main droplets (**Fig. 5.4a**). The micropillars have a diameter of 52 μm, with a gap of 48 μm, resulting in a pitch of 100 μm between adjacent pillars. These micropillars are arranged in rhombic unit cells, with a vertical shift of 33 μm between horizontally adjacent pillar columns, resulting in a critical diameter(D_c) of 40 μm for the DLD array (**Fig. 5.4d**). The gap sizes close to the DLD boundary were also modified as introduced in **Chapter 1**. The modified gap sizes are shown in **Table 5-1**, of which G_{ns} and G_{nl} are the gap size of n-th gap close to the walls with and without nozzles, respectively.

Table 4-1 Sizes of the gaps close to DLD boundary.

Gap #	G_{ns} (μm)	G_{nl} (μm)
1	28	62
2	39	55
3	48	48

Device-2 has a staggered DLD micropillar array within the main channel (**Fig. 5.4b**). This array also consists of 100 DLD regions, each corresponding to one of the 100 step-emulsification nozzles. In the first 25 regions, each DLD column has 26 micropillars, filling the main channel vertically. Beyond this point, the number of micropillars per column decreases by three for every additional region. For example, the columns in the 26th to 28th regions have 25 micropillars, while those in the 29th to 31st regions have 24 micropillars, and so on. The final six regions (95th to 100th) each contain only one pillar per column. This arrangement results in a stair-step pattern within the micropillar array. The size parameters

of the micropillars in Device-2 are identical to those in Device-1.

In both Device-1 and Device-2, the water and oil phases are introduced separately through the inlets. Once the oil phase fills the nozzles, main droplets with uniform size, along with the break-off of satellite droplets, are formed at the nozzles in a dripping regime. The droplets then flow along the continuous phase stream and enter the DLD region downstream. In Device-1, the main droplets (diameter $D > D_c$) migrate laterally through the gaps between the pillars in displacement mode towards the sidewall. In Device-2, the main droplets ($D > D_c$) are expected to exhibit similar bump-mode behavior; however, due to the stair-step arrangement of the micropillars, these droplets migrate to the ends of the pillar columns, resulting in a stair-step pattern of droplet arrangement. In the vertical direction to the flow, the droplets displaced by Device-1 are displaced to the region near the sidewall, while in Device-2, the droplets are expected to displaced through the whole channel (**Fig. 5.4e**).

5.2.2 Device fabrication

The PDMS devices were fabricated using standard soft lithography techniques. The process involved photolithography of the SU-8 mold, casting the PDMS replica, sealing it onto a slide glass, and performing hydrophilic surface modification. This process is similar to the one described in **Chapter 2**. The SU-8 mold for the step-emulsification section, created on a silicon wafer, had a height of 16 μm, while the DLD section and other channels had a height of 109 μm. After casting the PDMS replica, the chip was permanently bonded to a glass slide and immediately subjected to hydrophilic surface treatment.

5.2.3 Chemicals

The chemicals used in the experiments are listed in **Table 5-1**.

Table 5-1 Chemicals used.

Chemical	
Continuous phase	2 wt% polyvinyl alcohol
Dispersed phase	Corn oil

5.2.4 Equipment

The solutions were introduced into the device using syringe pumps, as detailed in **Table 5-2**. Droplet formation and migration were observed using a microscope equipped with a high-speed camera. The droplet count was analyzed using ImageJ software.

Table 5-2 Equipment used.

Syringe Type	Contents
Gas-tight glass (volume: 1 mL)	Corn oil
Plastic (volume: 50 mL)	PVA solution
Syringe pumps	Legato 180
	KDS 210

5.2.5 CFD simulation

Computational fluid dynamics (CFD) simulations were performed using Fluent software (Fluent 19.0; Ansys, Canonsburg, PA, USA) to visualize the flow streams in the mainchannel. The simulation settings are summarized in **Table 5-3**.

Table 5-3 CFD simulation setting.

Parameter	Value
Grid cell number	662,955
Maximum face size	3.35 mm
Boundary condition	Stationary, no slip
Liquid	Water
Density	998.2 kg/m^3
Dynamic viscosity	1.003 mPa s

5.3 Results and discussion

5.3.1 Droplet formation in side-arrayed step emulsification nozzles

In this section, the formation of main and satellite droplets in the step-emulsification nozzles arrayed alongside the DLD micropillar array is examined. With oil phase (Q_d) and water phase (Q_c) flow rates set at 0.2 mL/h and 10 mL/h, respectively, uniform droplet formation at the nozzle edges in the dripping regime was observed. At an upstream nozzle (Nozzle 2), droplet necking occurred at the nozzle tip, with the resulting droplets entering the DLD micropillar array from the sidewall (**Fig. 5.5a**). At a downstream nozzle (Nozzle 100), unlike the droplet formation observed in **Chapters 2** and **3**, droplets generated upstream did not flow near this nozzle. Instead, droplets formed at this nozzle entered the DLD micropillar array, similarly to those formed upstream (**Fig. 5.5b**). Although droplet detachment from the dispersed phase occurred close to the micropillars, the overall droplet formation process remained consistent with the previously described mechanism. The characteristic growth of the tongue-shaped tip of the oil phase and the backflow of the water phase after droplet pinching were observed, indicating that the micropillars did not interfere with the step-emulsification process.

The formation of satellite droplets was also examined using magnified views (**Fig. 5.5**). The satellite droplets exhibited the same break-off process and migration behavior within the DLD micropillar array as previously demonstrated. Despite some micropillars being positioned near the step-emulsification nozzles, the satellite droplets, significantly smaller than the critical diameter D_c of the DLD array, migrated in a zigzag mode along the sidewall, as expected. The back-and-forward motion of satellite droplets within the nozzles, caused by the backflow of the water phase, was also observed. In addition, the fabricated micropillars were not in a perfect cylinder-shape, and the pillars close to the nozzles were connecting. However, the main droplets flowed in bump mode as expected, indicating that the separation performance was not affected by the fabrication defects.

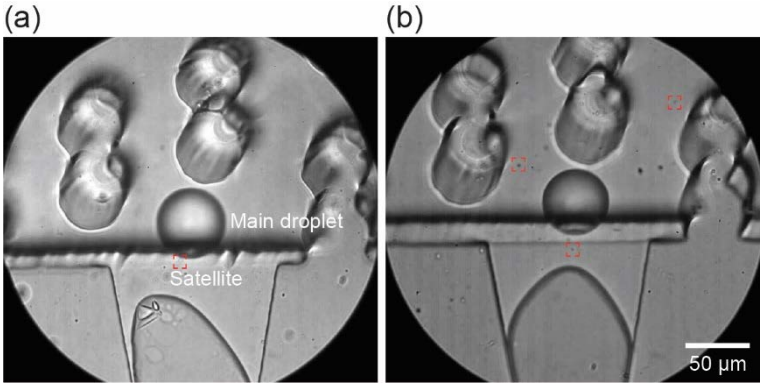

Fig. 5.5 Magnified view of droplet formation in Device-1. Main and satellite droplets break off from the oil phase at the edges of (a) the 2nd nozzle in the upstream region, and (b) the 100th region in the downstream region. No droplet accumulation or coalescence was observed.

5.3.2 Migration of droplets in Device-1

The main and satellite droplets migrated through the micropillar array along different paths based on their sizes immediately after forming at the nozzles. The migration of the main droplets at flow rates Q_d of 0.2 mL/h and Q_c of 10 mL/h is shown in **Fig. 5.6**. Under these flow conditions, the Reynolds number (Re) in the main channel was approximately 1.0, confirming laminar flow among the micropillars. The main droplets, with D_{avg} of ~53 μm, migrated toward the sidewall in displacement mode through the gaps between the pillars. No droplet accumulation and coalescence was observed near the nozzle tips.

The migration of the main droplets was analyzed in the upstream, midstream, and downstream regions of the device. The fractions of droplets passing through each vertical DLD gap in the 20th, 60th, and 100th DLD regions - corresponding to the positions of the respective nozzles - were recorded. In the 20th DLD region, the main droplets flowed uniformly through gaps 1–19 (**Fig. 5.6a**). In the 60th DLD region, corresponding to the midstream, the droplets migrated through all DLD gaps; however, 45% of the droplets passed through gap 29 near the sidewall, while the fractions for other gaps ranged from 1% to 6%. This difference was due to the significant lateral displacement of droplets generated upstream, which directed them toward the sidewall (**Fig. 5.6b**). In the 100th DLD region, a

substantial fraction of the main droplets (64.9%) flowed near the sidewall through gaps 24–29, resulting in a noticeable accumulation caused by the high droplet count and their displacement. Conversely, the fractions of the droplets passing through gaps 1–6 near the step-emulsification nozzles in the 100th DLD region were minimal (< 1%), indicating no significant accumulation near the nozzle tips (**Fig. 5.6c**). Additionally, in the upstream and midstream regions, the main droplets migrated in displacement mode with an expected migration angle of 18.4°, as the DLD micropillars effectively prevented localized droplet accumulation and reduced droplet interactions.

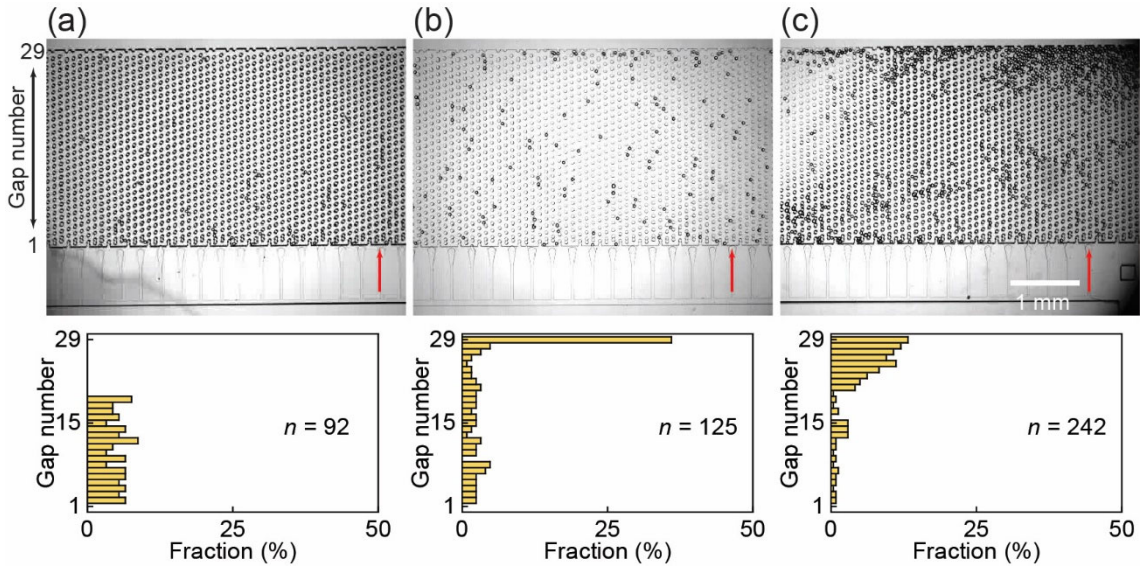

Fig. 5.6 Spatial distribution of main droplets flowing through the DLD pillar arrays after formation in Device-1. Droplet distributions in the (a) 20th DLD section (upstream), (b) 60th DLD section (midstream), and (c) 100th DLD (downstream) were recorded (indicated by red arrows).

The migration of satellite droplets through the DLD gaps was also observed. In **Fig 5.5**, satellite droplets entered the DLD micropillar array immediately after formation and migrated along the step emulsification nozzle array in a zigzag mode. In both the 20th and 100th nozzles corresponding to the upstream and downstream regions, the satellite droplets remained near the nozzles, with their numbers increasing from the upstream to the downstream regions.

5.3.3 Migration of droplets in Device-2

The migration of main and satellite droplets through the micropillar array in Device-2 was similarly governed by their sizes immediately after formation in the step emulsification nozzles. With Q_d of 0.2 mL/h and Q_c of 10 mL/h, the Re in the main channel remained approximately 1.0, consistent with the conditions observed in Device-1.

The migration behavior of the main droplets is shown in **Fig. 5.7**. The main droplets, with D_{avg} of ~53 μm, migrated across the DLD micropillar array in displacement mode, with no observable accumulation or coalescence near the nozzle tips. The migration of the main droplets was analyzed in the upstream, midstream, and downstream regions of the device. The vertical distance of the droplets from the step-emulsification nozzles in the 20th, 60th, and 100th DLD regions – corresponding to the positions of the respective nozzles - was recorded. In the 20th DLD region, the main droplets were uniformly distributed across a vertical distance of 0–1.6 mm (**Fig. 5.7a**). In the 60th DLD region, corresponding to the midstream region, droplets were distributed across a distance of 0–2.0 mm. Similar to Device-1, 63% of the droplets were concentrated within the 1.4–2.0 mm range, while the remaining 37% were spread across other areas. However, unlike in Device-1, the droplets closest to the sidewall (1.8–2.0 mm) did not exhibit the highest fraction. This difference is attributed to the stair-step arrangement of the DLD micropillar array, whose pillar columns ended at region with varying distance from the sidewall, and therefore directed the droplets to positions at varying distances from the sidewall (**Fig. 5.7b**). In the 100th DLD region, where only a single column of micropillars was present, the majority of main droplets (91%) remained close to the step-emulsification nozzles, within a distance of 0–0.6 mm, while a smaller fraction was distributed across the 0.6–2.0 mm range (**Fig. 5.7c**).

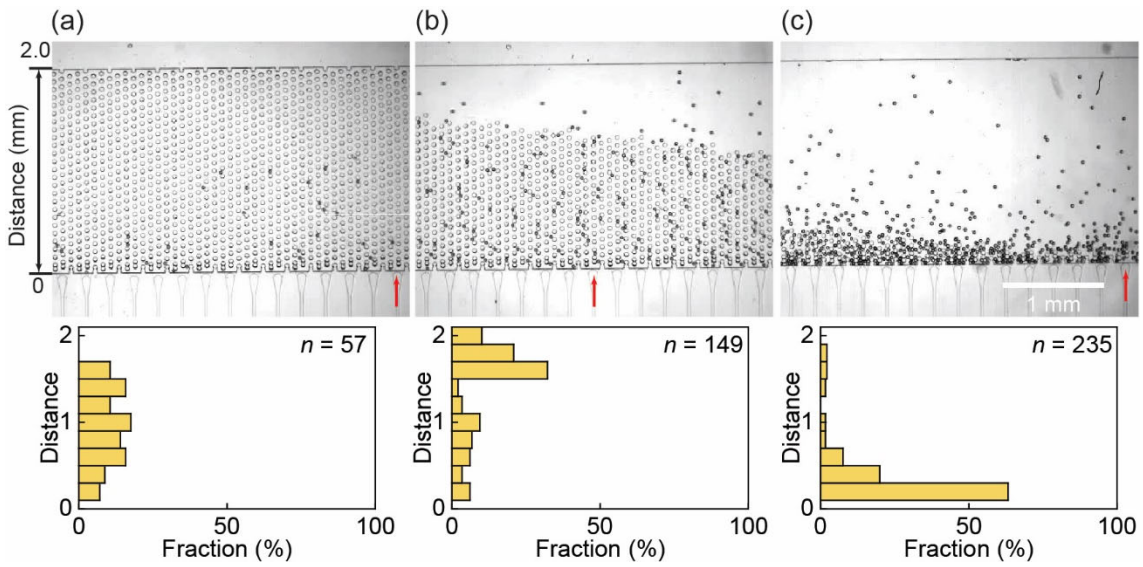

Fig. 5.7 Spatial distribution of main droplets flowing through the DLD pillar arrays after formation in Device-2. Droplet distributions in the (a) 20th DLD section (upstream), (b) 60th DLD section (midstream), and (c) 100th DLD section (downstream) were recorded (indicated by red arrows).

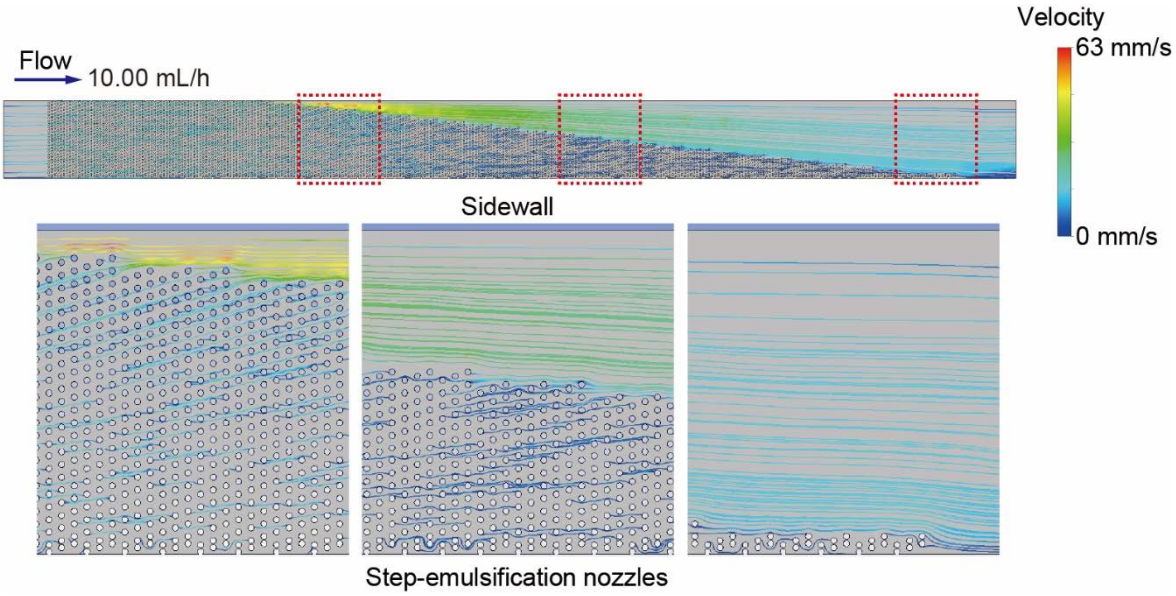

Fig. 5.8 Streamlines in the main channel. Regions in the dashed red squares are shown in the magnified views. The streamlines exiting the micropillar array bend toward the side containing the step-emulsification nozzles.

The unexpected results were likely caused by the distorted flow streams in the main channel, resulting from the stair-step arrangement of the DLD micropillar array. To further

investigate the flow behavior, a CFD fluid simulation was performed using water at a flow rate of 10 mL/h through the model with the DLD micropillar array. The streamline profile in the main channel is shown in **Fig. 5.8**. The streamlines exiting the DLD micropillar array were not parallel to the sidewall but instead bent toward the side containing the step-emulsification nozzles. These simulation results align with the experimental observations, confirming the oblique flow of droplet toward the nozzle side.

5.3.4 Discussion

The two devices demonstrated in this chapter offer several advantages over the droplet-separation devices with serially arranged step-emulsification nozzles and DLD pillar arrays presented in earlier chapters. First, the issue of clogging and coalescence due to droplet accumulation near the step-emulsification nozzles was resolved by positioning the nozzle ends along the sidewall of the DLD micropillar array. This arrangement allows the main droplets produced by the step-emulsification nozzles to be displaced vertically away from the nozzles immediately upon entering the DLD micropillar array, creating sufficient space near each nozzle for continuous droplet generation. Consequently, this design enables more efficient droplet production using step emulsification. Second, unlike the devices described in the previous chapters, which featured serially arranged nozzles and DLD micropillar arrays, the connection of the nozzle ends to the sidewall of the DLD micropillar array significantly reduces the overall device length, allowing fabrication on a smaller wafer.

While the proposed devices effectively address droplet accumulation and coalescence near the step-emulsification nozzles, some limitations remain. In Device-1, displaced droplets accumulated in the downstream region near the sidewall of the DLD array. To mitigate this issue, Device-2 was introduced with a stair-step DLD micropillar array to distribute the main droplets evenly across the entire vertical extent of the main channel. However, the stair-step DLD array led to uneven fluid distribution in the main channel, causing the displaced main droplets to migrate back toward the region near the step-emulsification nozzles, resulting in accumulation in the downstream region.

To overcome this limitation, two potential solutions are proposed. The first involves

incorporating an additional stair-step micropillar array downstream of the DLD region. This array, without pillar shifts, would occupy the vacant area currently lacking a DLD array, compensating for the resistance to fluid flow in the upstream region (**Fig. 5.9a** and **c**). The second approach involves dividing the region without micropillars into several sections using walls. Once the main droplets are displaced from the DLD array at varying distances, they will enter these separated regions, limiting their return to the nozzle area and thereby preventing droplet accumulation (**Fig. 5.9b** and **d**).

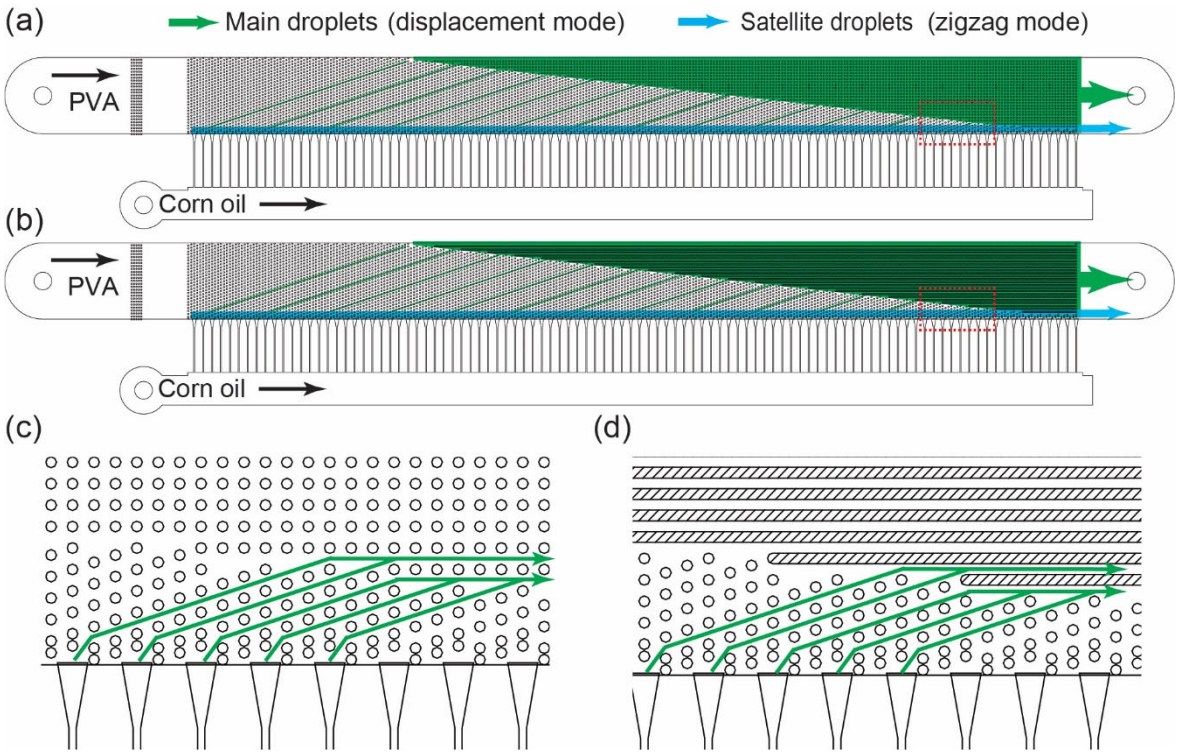

Fig. 5.9 Methods to improve droplet migration in the channel. (a) A device having both a DLD micropillar array and a normal pillar array without pillar shift. (b) A device with a DLD micropillar array and dividing walls at the end of the DLD region. (c) Magnified view of the section in (a), showing droplets migrating straight through the normal pillar array without returning to the nozzles. (d) Magnified view of the section in (b), illustrating how walls guide droplets toward the outlet after migration through the DLD array.

5.4 Conclusion

This chapter presented an approach aimed at inhibiting droplet accumulation near the ends of the step-emulsification nozzles by displacing the main droplets toward the sidewall. Device-1, having 100 step emulsification nozzles and a DLD micropillar array with a D_c of 40 μm, was first investigated to verify continuous droplet generation at the nozzles and their subsequent migration through different paths within the DLD micropillar array. Main droplets with a mean diameter of approximately 53 μm were effectively displaced across the DLD array immediately after formation, and no main droplets were observed flowing near the step-emulsification nozzles after entering the DLD array.

Building on these findings, Device-2, equipped with a stair-step DLD micropillar array designed to distribute the main droplets across different areas of the main channel, was evaluated. In the step-emulsification section with 100 nozzles, Device-2 exhibited similar droplet formation behavior as Device-1. The main droplets migrated through the DLD array and reached the end of the micropillar array at varying distances from the sidewall. However, most of the main droplets then flowed along the end of the DLD array and flowed back toward the nozzles in the downstream region. Although the migration pattern of the main droplets in Device-2 did not align with our expectations, both devices successfully displaced the main droplets away from the step-emulsification nozzles.

The proposed devices offer a promising configuration for conventional step emulsifiers, addressing the issues of droplet accumulation and coalescence, thereby improving overall performance.

References

[1] Z. Shi, X. Lai, C. Sun, X. Zhang, L. Zhang, Z. Pu, D. Li. Step emulsification in microfluidic droplet generation: mechanisms and structures. *Chem. Comm.*, **2020**, 56, 9056–9066.

[2] Z. Liu, C. Duan, S. Jiang, C. Zhu, Y. Ma, T. Fu. Microfluidic step emulsification techniques based on spontaneous transformation mechanism: A review. *J. Ind. and Eng. Chem.*, **2020**, 92, 18–40.

[3] S. Sugiura, M Nakajima, J. Tong, H. Nabetani, M. Seki. Preparation of monodispersed solid lipid microspheres using a microchannel emulsification technique. *J. Colloid Interface Sci.*, **2000**, 227, 95–103.

[4] N. Mittal, C. Cohen, J. Bibette, N. Bremond. Dynamics of step-emulsification: From a single to a collection of emulsion droplet generators. *Phys. Fluids*, **2014**, 26, 082109.

[5] T. Kawakatsu, Y. Kikuchi, M. Nakajima. Regular-sized cell creation in microchannel emulsification by visual microprocessing method. *J. Am. Oil Chem. Soc.*, **1997**, 74, 317–321.

[6] F. Schuler, N. Paust, R. Zengerle, F. Von Stetten. Centrifugal step emulsification can produce water in oil emulsions with extremely high internal volume fractions. *Micromachines*, **2015**, 6, 1180–1188.

[7] F. Schuler, F. Schwemmer, M. Trotter, S. Wadle, R. Zengerle, F. von Stetten, N. Paust. Centrifugal step emulsification applied for absolute quantification of nucleic acids by digital droplet RPA. *Lab Chip*, **2015**, 15, 2759–2766.

[8] D. C. Shin, Y. Morimoto, J. Sawayama, S. Miura, S. Takeuchi. Centrifuge-based step emulsification device for simple and fast generation of monodisperse picoliter droplets. *Sens. Actuator B Chem.*, **2019**, 301, 127164.

[9] M. Schulz, S. Probst, S. Calabrese, A. R. Homann, N. Borst, M. Weiss, F. von Stetten, R. Zengerle, N. Paust. Versatile tool for droplet generation in standard reaction tubes by centrifugal step emulsification. *Molecules*, **2020**, 25, 1914.

[10] E. Stolovicki, R. Ziblat, D. A. Weitz. Throughput enhancement of parallel step

emulsifier devices by shear-free and efficient nozzle clearance. *Lab Chip*, **2018**, 18, 132–138.

[11] R. Dangla, S. C. Kayi, C. N. Baroud. Droplet microfluidics driven by gradients of confinement. *Proc. Natl. Acad. Sci. USA*, **2013**, 110, 853–858.

[12] C. Zheng, S. Masui, Y. Kanno, T. Nisisako. Microfluidic step emulsification with parallel nozzles on a vertical slit. *Ind. Eng. Chem. Res.*, **2024**, 63, 10226–10233.

Chapter 6

Scalable droplet processing via module parallelization

6.1 Introduction

6.1.1 Scale-up droplet processing in step emulsification

Mass-production for various materials is an essential part of droplet microfluidics, which has been intensely investigated[1–3]. A common approach for mass-production of droplets is scaling-up of droplet-makers. As introduced in **Chapter 2**, step emulsification is a useful method for scale-up production of droplets because they are very robust to flow rate fluctuations, and a scale-up design of step emulsification nozzles has been addressed[4–15]. One typical design is the "cross-flow" setup, where the continuous phase flows vertically over an array of parallel nozzles to collect the formed droplets[6]. A microfluidic device integrating 11,900 through holes in 14 arrays for the mass-production of droplets has been reported (**Fig. 6.1a**)[7]. Moreover, a device made from silicon with dry-etched "straight-through" nozzles has achieved high-density parallelization[8]. This silicon-based design was further developed, and a square plate having 211,248 nozzles distributed in 4 sections was demonstrated for the production of monodisperse oil emulsions. (**Fig. 6.1b**)[10].

Parallel step emulsifiers applied in the production of various functional microparticles have also been demonstrated [12]. For example, a step emulsification device with terrace type nozzles was reported for the production of water-in-oil-in-water (W/O/W) double emulsions. In this study, pre-mixed water-in-oil emulsions were used as the dispersed phase, and infused into the device, which has 360 nozzles arranged in 4 arrays (**Fig. 6.2a**)[13]. Additionally, the production of chitosan-based hydrogel microparticles using device with multiple arrays of step emulsification nozzles (**Fig. 6.2b**)[14]. This device has 1,070 nozzles arranged in 10 arrays for the production of the precursor water-in-oil emulsions, which were used for the off-chip gelation of chitosan hydrogel microparticles. In addition, this design has also been applied for the production of alginate-based hydrogel particles[15].

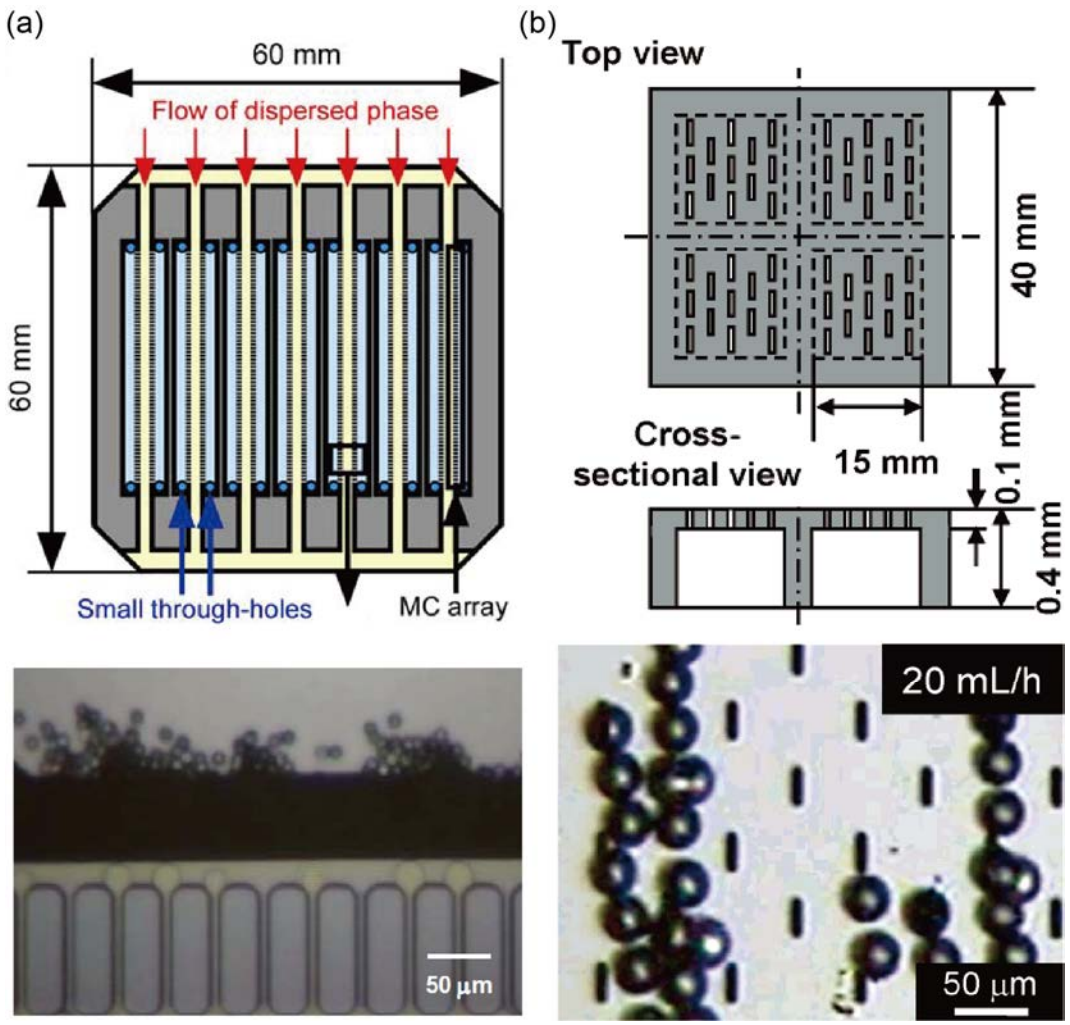

Fig. 6.1 Mass-production of droplets in parallel step emulsifiers. (a) Schematic illustration of a device having 11,900 through holes in 14 arrays for the production of droplets. And the image of droplet formation at the ends of the through holes[7]. (b) Schematic illustration of a design with 211,248 nozzles distributed in 4 sections. And the image of droplet formation at the nozzles[10]. (a) Reproduced with permission from Springer. (b) Reproduced with permission from American Chemical Society.

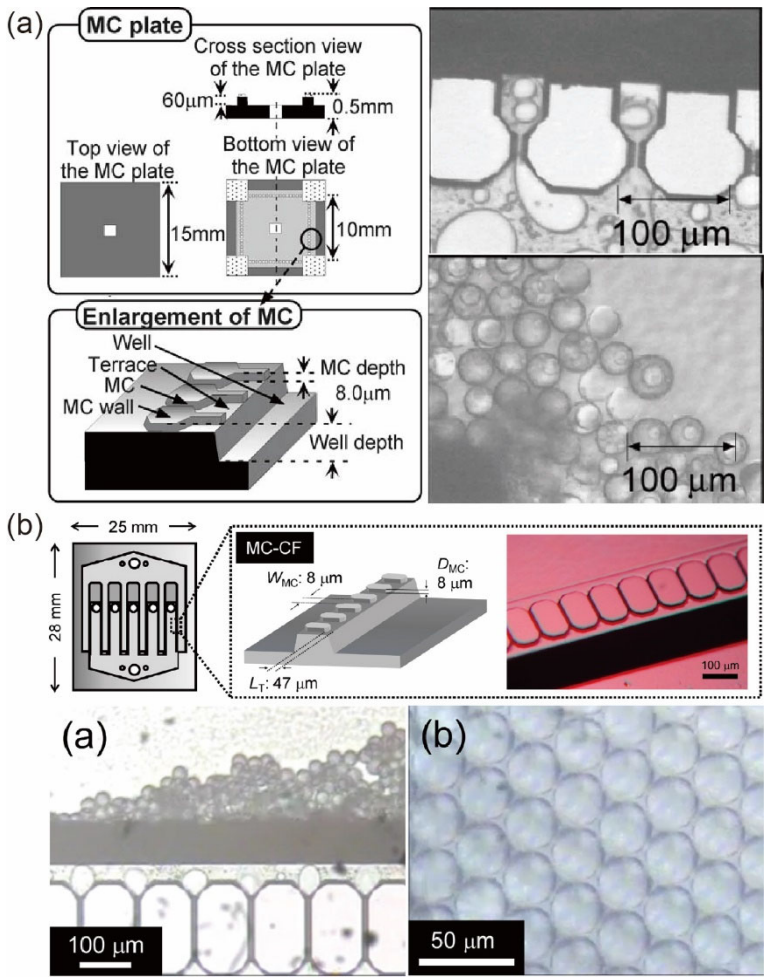

Fig. 6.2 Mass-production of functional particles via step emulsifiers. (a) A schematic illustration of a terrace type step emulsification device with 360 nozzles for the production of double emulsions. Formation and the collection of the produced double emulsions[13]. (b) A device with 1,070 step emulsifiers in 10 arrays for the production of chitosan-based hydrogel microparticles[14]. (a) Reproduced with permission from Elsevier. (b) Reproduced with permission from Elsevier.

6.1.2 Scale-up processing of satellite-free droplets

As introduced in **Chapter 2**, the droplet production via step emulsification faces the challenge of satellite droplets. The microfluidic separation of satellite droplets using carious approach like bifurcating channel and deterministic lateral displacement (DLD) has been demonstrated by several studies[16–20]. Among these previous studies, a device for the mass-production of satellite droplets using DLD has been reported by Tottori et al.[20]. This study

proposed a device having eight parallel arranged modules, which consists of a flow-focusing droplet-maker and a DLD micropillar array, and achieved a throughput of the satellite-free droplets of 0.2 mL/h (**Fig. 6.3**).

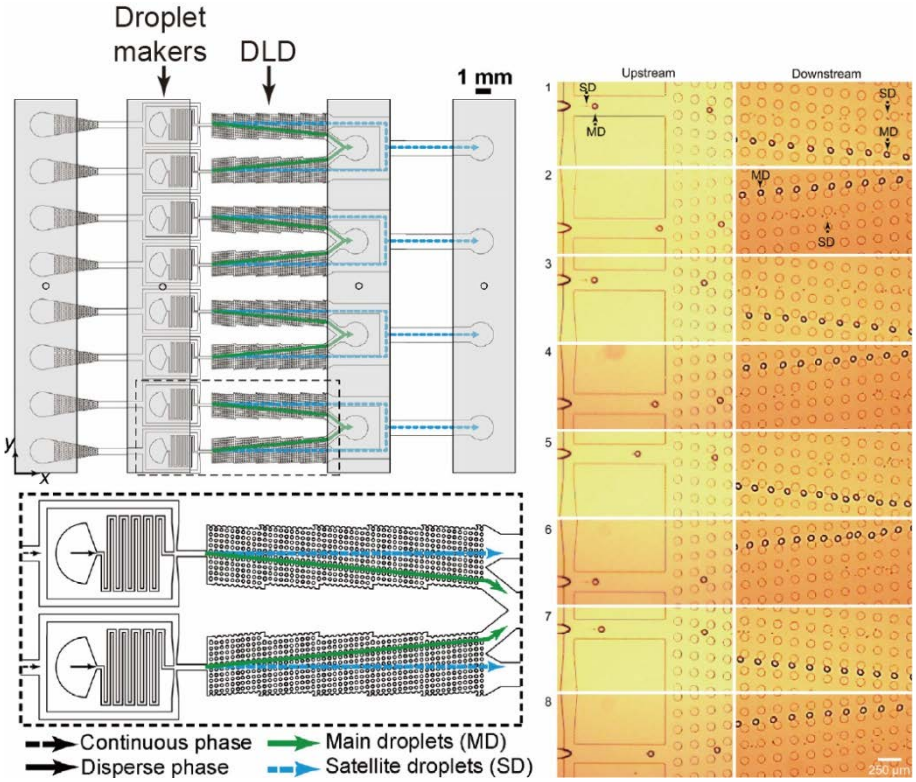

Fig. 6.3 Mass-production of satellite-free droplets in eight parallel modules with flow-focusing droplet-maker and DLD micropillar array. The droplets were generated and separated in all eight modules[20]. Reproduced with permission from Elsevier.

In **Chapter 2**, the production of satellite-free droplets via a single module of cross-flow type step-emulsification nozzles and DLD arrays was demonstrated. Monodisperse droplets with a throughput of 0.2 mL/h were generated by 60 nozzles. However, the study of **Chapter 2** used only a single droplet generation module, and the potential for droplet mass production including further increasing the number of modules had not yet been developed.

6.1.3 Objective

This chapter explores an integrated system designed for the large-scale production of satellite-free droplets. The system consists of ten parallel modules, each combining step emulsification and deterministic lateral displacement (DLD). Liquid is supplied to each module

through a ladder-like structure, enabling the generation of satellite-free droplets using a step emulsifier arranged in a millipede configuration. The uniform distribution of fluids across all modules was confirmed through 3D flow simulations. Experimental validation demonstrated the generation of uniform-sized main droplets and the efficient separation of main and satellite droplets via DLD arrays in all ten modules.

6.1.4 Outline of this chapter

Section 6.1 Introduction

Introduces the structural designs used for large-scale droplet processing.

Section 6.2 Materials and methods

Describes the microfluidic devices, their fabrication processes, and the peripheral equipment utilized in this study.

Section 6.3 Results and discussion

Presents the results of the 3D fluid flow simulations, along with the generation and separation of main droplets.

Section 6.4 Conclusion

Summarizes the main conclusions drawn from this chapter.

6.2 Materials and methods

6.2.1 Device design and mechanism

A microfluidic device was designed, comprising two main parts: an upper section with four chambers designated to introduce liquid and collect droplets, and a lower section containing ten modules, where step emulsifiers and deterministic lateral displacement (DLD) separators are arranged (**Fig. 6.4a**). The two parts were assembled and sealed with a glass slide. Each chamber in the upper section (dimensions: 60 mm × 3 mm × 5 mm) features a central hole for introducing fluid or collecting droplets. The lower section consists of ten parallel modules, each with two inlets for the dispersed and continuous phases and two outlets for collecting the main and satellite droplets. The inlets and outlets are interconnected via the chambers. The layout of each module is symmetric, with a central channel for the dispersed phase flanked by two arrays of 50 step emulsifiers (100 in total per module). Downstream of the main channel, two DLD arrays are positioned, leading to the outlets where the main and satellite droplets are collected (**Fig. 6.4b**).

The design of the step emulsifiers is similar to that described in **Chapter 2**, and the size parameters are listed in **Table 6-1**.

Table 6-1 Size parameters of the step emulsifier.

Pitch distance	200 μm
Length	1 mm
Depth	18 μm (**Fig. 6.4f, g, and h**)
Open angle of the nozzle	9.8° (**Fig. 6.4e**)
Open width	140 μm (**Fig. 6.4e**)
Minimum width	25 μm (**Fig. 6.4e**)
Length of the nozzle	333 μm (**Fig. 6.4e**)

The design of the DLD micropillar arrays is also similar to the one presented in **Chapter 2**. The size parameters are provided in **Table 6-2**. The critical diameter (D_c) of this device, calculated using equation (1), was designed to be 47 μm.

$$D_c = 1.4 \times G \times (\Delta\lambda/\lambda)^{0.48} \quad (6\text{-}1)$$

Table 6-2 Size parameters of the DLD array.

DLD region	
Number of columns	5 (**Fig. 6.4d**)
Number of gaps	10 (**Fig. 6.4d**)
Number of DLD regions	20
DLD cell	
Diameter of pillar	77 μm (**Fig. 6.4c**)
Size of gap (G)	73 μm (**Fig. 6.4c**)
Pitch between pillars (λ)	150 μm (**Fig. 6.4c**)
Shift of the pillar ($\Delta\lambda$)	30 μm (**Fig. 6.4c**)
Critical diameter (D_c)	47 μm

The gap sizes close to the DLD boundary were also midified as introduced in **Chapter 1**. The modified gap sizes are shown in **Table 6-3**, of which G_{ns} and G_{nl} are the gap size of n-th gap close to the walls with and without nozzles, respectively.

Table 6-3 Sizes of the gaps close to DLD boundary.

Gap #	G_{ns} (μm)	G_{nl} (μm)
1	33	98
2	46	92
3	57	86
4	65	80
5	73	73

Water and oil were introduced separately through the inlets in the upper section, filling the inlet chambers before flowing down into the ten modules in the lower section. Once in the center channel, the oil phase entered the emulsifiers, generating monodisperse droplets and

satellite droplets in the dripping regime. These droplets flowed through the main channel into the DLD section. In the DLD section, the main droplets (with diameters $D > D_c$) migrated in the displacement mode, while the smaller satellite droplets flowed in the zigzag mode. After passing through the DLD separator, the main droplets exited through outlet-L, and the satellite droplets exited through outlet-S, both of which were collected in the upper chambers.

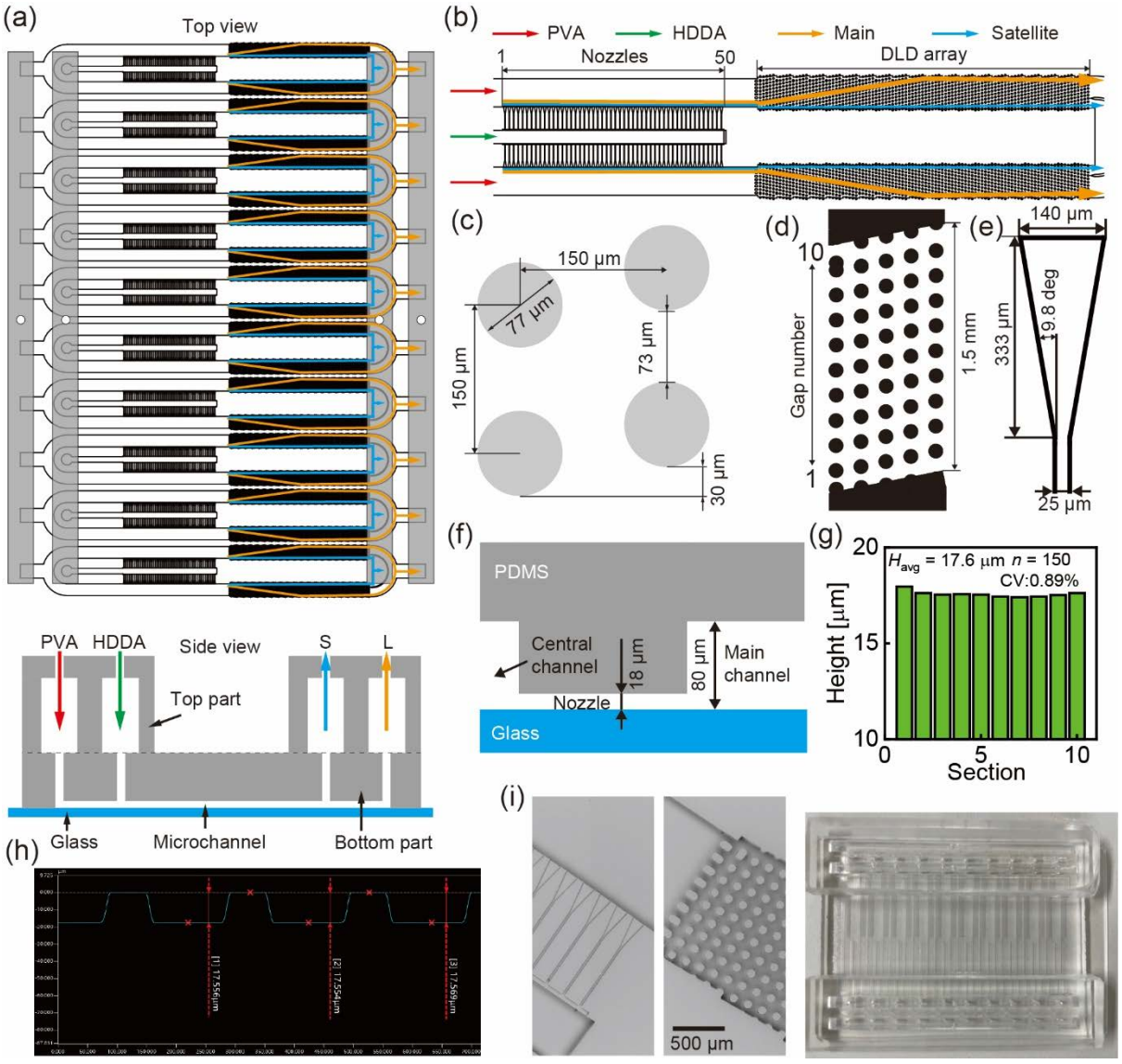

Fig. 6.4 A microfluidic device with 10 parallel step-emulsifiers and DLD modules for sorting main and satellite droplets. (a) Schematic top and side views of the whole device, and (b) a single module. (c) Unit of the DLD pillars. (d) Single region containing the 5-column DLD pillars. (e) Dimensions of the triangular end of the step-emulsification nozzle. (f) Schematic cross-section of a step-emulsification nozzle. (g) Height distribution of the PDMS nozzles across the 10 modules. (h) Height measurements of a portion of the PDMS step-emulsification nozzles, as measured by a laser microscope. (i) SEM images of the PDMS chip and an image of the device.

6.2.2 Device fabrication

The bottom part of the device was fabricated from PDMS through standard soft lithography. This process created an SU-8 mold with a height of 80 μm on a 4-inch diameter silicon wafer, followed by casting a PDMS replica, as described in detail in **Chapter 2**.

The upper part of the device was also cast using PDMS but from an acrylic mold. Four rectangular acrylic blocks (5 mm × 60 mm × 3 mm) were laser-cut from an acrylic board. These blocks were arranged and taped to a petri dish. After the PDMS chip was removed, four holes (1 mm in diameter) were punched to serve as inlets and outlets.

The PDMS device underwent the same sealing and hydrophilic treatment as described in **Chapter 2** (**Fig. 6.4i**). After the two parts were assembled and sealed by a glass slide, the device was treated with a superhydrophilic polymer (SPRA 202, Tokyo Ohka Kogyo, Kanagawa, Japan) to ensure proper wettability.

6.2.3 Chemicals and equipment

The 2 wt% aqueous polyvinyl alcohol (PVA) solution and 1,6-Hexanediol diacrylate (HDDA) used as the continuous and dispersed phases, respectively, are listed in **Table 6-3**. The syringes and syringe pumps used in the experiments are detailed in **Table 6-4**.

Table 6-3 Chemicals used.

Continuous phase	2 wt% aqueous PVA solution
Dispersed phase	HDDA

Table6-4 Equipment used.

Syringe	Contents
Gas-tight glass (volume: 10 mL)	aqueous PVA solution
Plastic (volume: 50 mL)	HDDA
Syringe pump	Legato 200 x 2

Droplet formation and migration were observed using a microscope equipped with a high-speed camera. Droplet counting and size distribution analysis were conducted using images processed through the software ImageJ (National Institute of Health, MD, USA).

6.2.4 CFD simulation

Computational fluid dynamics (CFD) simulations were implemented using Fluent software to analyze fluid flow distribution within the inlet chambers and DLD sections. The channels were modeled with tetrahedron-shaped grid cells using Ansys Meshing. The solid channel wall was set to be a stationary and no-slip boundary. A mass flow rates of the working liquid, the water liquid, were set at the inlets, while the pressure-outlet boundary was set to be a gauge pressure of 0 Pa. Details of the simulation models and working liquid are provided in **Table 6-5**.

A pressure-based solver for steady-state simulations with a viscous laminar flow model was chosen. The coupling of pressure-velocity was solved by the SIMPLE algorithm. For spatial discretization, a second-order upwind scheme was selected for the momentum equations. Residuals for continuity and momentum equations were monitored. While the residuals were stable below 10^{-3}, the solution was considered to be converged.

Table 6-5 Models and simulation conditions.

Model		
	Inlet chamber	DLD section
Grid cell number	~ 1 million	~ 0.8 million
Maximum face size	200 μm	5 μm
Liquid	Water	
Density	998.2 kg/m^3	
Dynamic viscosity	1.003 mPa s	

6.3 Results and discussion

6.3.1 CFD simulation

To examine the distribution of flow rates in 10 modules, 3D fluid flow simulations were conducted for both the inlet chamber and a single DLD module. These simulations were simplified using an equivalent electric circuit model. Initially, the inlet chamber (**Fig. 6.5a**) and the DLD pillar array (**Fig. 6.6a**) were modeled to compute the hydraulic resistance of each element. Since the flow distribution, dominated by the ratio of hydraulic resistances, does not depend on fluid viscosity, water was chosen as the model liquid. The electrical circuit model was then employed to predict the flow distribution from the inlet chamber across the ten modules.

The inlet chamber model had a top via hole acting as the inlet (1 mm in diameter, 3 mm long), a rectangular cuboid-shaped channel (60 mm × 3 mm × 5 mm), and ten bottom via holes, serving as outlets (1 mm in diameter, 4 mm long; **Fig. 6.5a**). A flow rate of 50 mL/h was applied at the inlet, and the flow distribution through the ten outlets, open to atmospheric pressure, was calculated. **Fig. 6.5b** illustrates the fluid velocity in the vertical cross-section, showing a uniform and low velocity throughout the horizontal chamber and at the ten outlets. **Fig. 6.5c** presents the flow rate distribution and velocity profile at the ten outlets. The average flow rate was 5.00 mL/h with a CV of 2.0%, indicating a uniform distribution of fluid, with the parabolic velocity profiles reflecting Hagen-Poiseuille flow characteristics.

With increasing the inlet flow rate from 10 to 50 mL/h, the CV of the outlet flow rates only changed slightly, from 2.0% to 2.4%, indicating a consistent flow distribution. This suggests that the hydraulic resistance of the ten vertical outlets was much greater than the horizontal elements in the chamber. Thus, the 3D model (**Fig. 6.5a**) could be simplified into an equivalent electric circuit with ten parallel resistors ($r_{1–10}$) of nearly identical values.

Fig. 6.5d shows the average outlet flow rate (Q_{avg}) versus the pressure drop (ΔP) for inlet flow rates ranging from 10 to 50 mL/h. As Q_{avg} increased from 1.0 to 5.0 mL/h, ΔP linearly increased from 0.44 to 2.26 Pa. This linear relationship is consistent with Hagen-Poiseuille's law ($\Delta P = Q_{avg}R$), where R is the hydraulic resistance. The hydraulic resistance of the ten outlets ($r_{1–10}$), based on the pressure drop for each outlet flow rate, ranged from 1.57 to 1.66 GPa·s/m³,

with an average resistance (r_{avg}) of 1.62 GPa·s/m³.

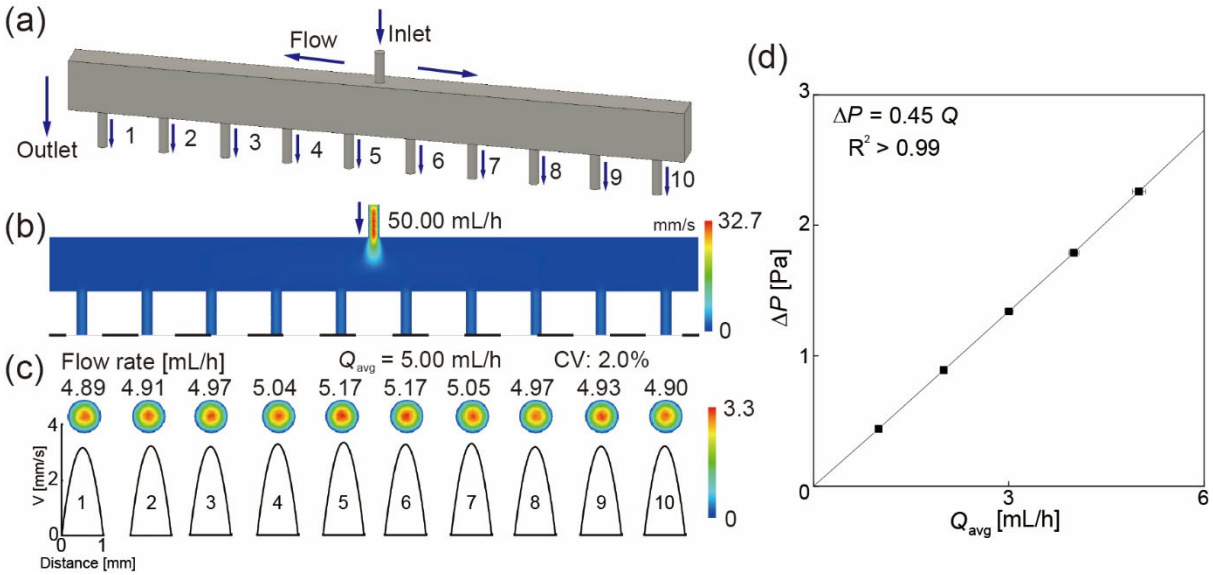

Fig. 6.5 (a) 3D fluid flow simulation of the inlet chamber. (b) Velocity distribution in the vertical cross-section of the inlet chamber. (c) Velocity distribution and profile in the middle of the ten outlets. The input flow rate was 50 mL/h. (d) Pressure drop versus average outlet flow rates, with the hydraulic resistance of the inlet chamber being 0.45 GPa·s/m^3.

The hydraulic resistance of a DLD section comprising five columns and ten rows (**Fig. 6.6a**) was similarly calculated. Varied flow rates (0.5 to 2.5 mL/h) were applied, with the outlet exposed to atmospheric pressure. As the flow rate increased, the pressure drop (ΔP) also increased linearly, ranging from 3.07 to 15.34 Pa. The hydraulic resistance of a single DLD section (R_0) was calculated as 2.21 × 10¹ GPa·s/m³ (**Fig. 6.6b**). For a DLD micropillar array with 20 repeated sections, the total hydraulic resistance (R_D) was found to be 4.42 × 10² GPa·s/m³, which is twenty times the resistance of a single DLD section (R_0) (**Fig. 6.6c**).

The hydraulic resistance of the channel without pillars (R_c) can be obtained using the equation[13]:

$$R_c = \frac{12\eta L}{h^3 w}\left(1 - \frac{192h}{\pi^5 w}\right)^{-1} \quad (6\text{-}2)$$

where η is the fluid viscosity, L is the channel length, and w and h are the channel width and height, respectively, with $w > h$. Using η = 1 mPa·s, L = 17.8 mm, w = 1.275 mm, and h = 80 μm, R_c was calculated to be 3.41 × 10¹ GPa·s/m³.

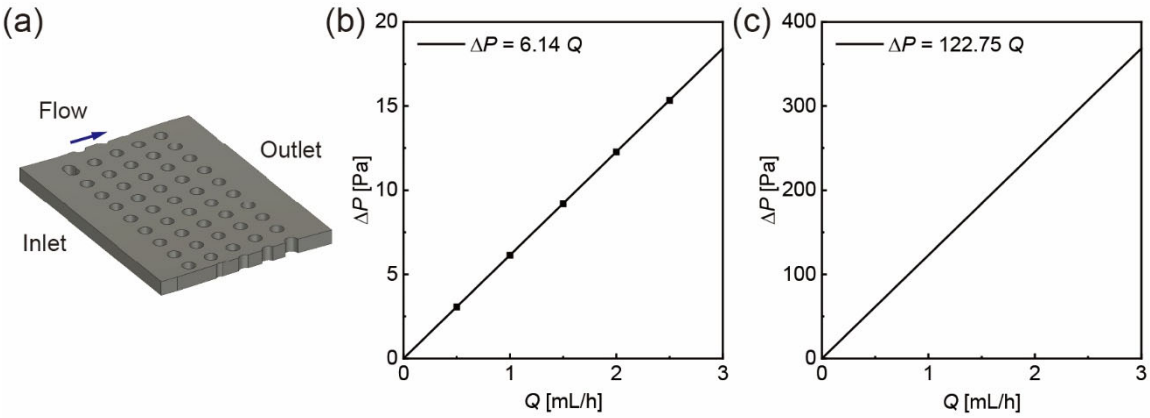

Fig. 6.6 (a) 3D fluid flow simulation of a DLD section. (b) Pressure drop versus flow rate for the DLD section, with a calculate hydraulic resistance of 2.21×10^{1} GPa·s/m^3. (c) Pressure drop versus flow rate for the DLD array with 20 sections, where the hydraulic resistance was 4.42×10^{2} GPa·s/m^3.

To evaluate the flow rate distribution in 10 modules, a simplified model was used, regarding the upper chambers and 10 lower modules as an equivalent parallel electronic circuit (**Fig. 6.7**). Channels for the dispersed phase were excluded because of their small volume fraction (5.7%). The downstream channels from the DLD region were simplified into a single outlet, with half the hydraulic resistance of the inlet chamber ($r_{1–10}$). The hydraulic resistance of 10 modules was modeled in parallel. In each module, the inlet chamber ($r_{1–10}$), the microfluidic channel (with and without DLD pillars, $0.5R_C + 0.5R_D$), and the outlet chamber ($0.5r_{1–10}$) were serially arranged. The flow rate ratio between two DLD modules (m-th and n-th) was calculated using the following equation:

$$\frac{Q_m}{Q_n} = \frac{r_n+0.5R_C+0.5R_D+0.5r_n}{r_m+0.5R_C+0.5R_D+0.5r_m} = \frac{1+\frac{3r_n}{R_C+R_D}}{1+\frac{3r_m}{R_C+R_D}} \quad (6\text{-}3)$$

Since the inlet chamber has much lower hydraulic resistance than the microfluidic channels (with and without DLD pillars, $R_C + R_D = 294\ r_{avg}$), the flow rate ratio Q_n/Q_1 varied by less than 0.06% across the ten modules (**Table 6-6**). Compared with the flow rate distribution with CV of 2.0% calculated in the model having only an inlet chamber, the distribution calculated by this simplified model, which had the channels through the whole device (inlet chamber, microchannels, outlet chambers), was considered to be closer to the real situation and had

smaller value. This proved the uniform flow distribution across all modules through numerical simulation and theoretical modeling.

Table 6-6 Flow rate ratio across modules.

Module #	100 * Q_n/Q_1 (%)	Module #	100 * Q_n/Q_1 (%)
1	100	6	100.06
2	100.01	7	100.03
3	100.01	8	100.02
4	100.03	9	100.01
5	100.06	10	100.00

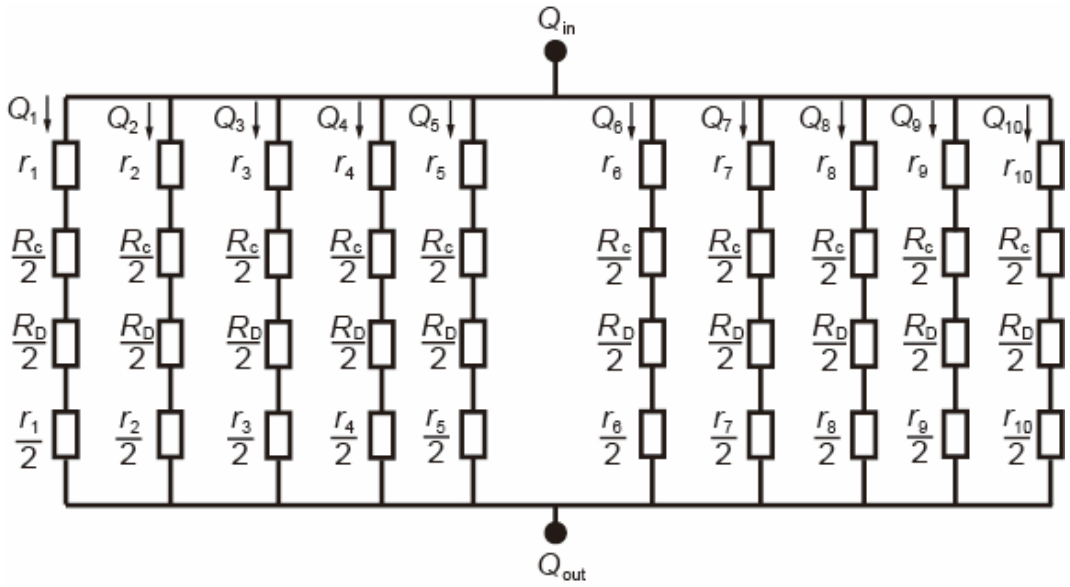

Fig. 6.7 Schematic of hydraulic resistance model in the inlet chamber and step-emulsification/ DLD modules. R_C represents the resistance of the straight microfluidic channel, R_D denotes the resistance of the DLD section, and $r_{1–10}$ represents the resistance of the inlet chamber. $Q_{1–10}$ indicates the flow rates in each module.

6.3.2 Droplet formation in parallel modules

This section outlines the droplet formation process using parallel step-emulsification nozzles in 10 modules. To evaluate the performance of this chapter with **Chapter 2**, the same continuous phase (PVA solution) and dispersed phase (HDDA) were utilized. After confirming

the generation of both main and satellite droplets at the step emulsifiers in all modules, droplet size and generation frequency in all modules were measured. In addition, the flow rates of HDDA across the modules were calculated and analyzed.

Prior to starting the experiment, the entire channel system was filled with a PVA solution to create a liquid environment. HDDA was then introduced into the inlet chamber at the top and flowed into the ten modules. The fluid from the inlet chamber remained stable throughout the process. With the continuous phase flow rate (Q_c) set to 50.0 mL/h and dispersed phase flow rate (Q_d) set to 3.0 mL/h, droplets with a narrow size distribution were generated in the dripping regime across all modules (**Figs. 6.8** and **6.9a**).

Out of the 1,000 step-emulsification nozzles across all modules, 986 nozzles (98.6%) functioned as expected, producing droplets, while 14 nozzles (1.4%) became clogged and did not form droplets. The main droplets had an average diameter of 66 μm, with a CV of 3.1% (n = 1999) (**Figs. 6.9b** and **6.9c**). Across the ten modules, the main droplets exhibited high monodispersity, with average diameters ranging from 65 to 67 μm. No coalescence of droplets was observed near the nozzles.

The droplet production rate (F) was measured for each module, yielding an average rate of 539.5 ± 28.6 drops/s (n = 10) per module, with a total of 5,395 drops/s for the entire device (**Fig. 6.9b**). The throughput of the dispersed phase was determined by multiplying the droplet size by the production rate in each module, which had a variation of 7.3%. (**Fig. 6.9c**). Although the flow rates were typically lower in the outer modules and higher in the central ones, modules 7 and 8 displayed unexpectedly higher flow rates compared to modules 5 and 6, likely due to fabrication inconsistencies of the nozzle heights of the 10 modules, which have the man value of 18 μm with CV of 1.5% (n =10). However, these differences were not significant enough to impact the droplet sizes generated across 10 modules, highlighting the robustness of step emulsification against minor fluctuations in flow rates.

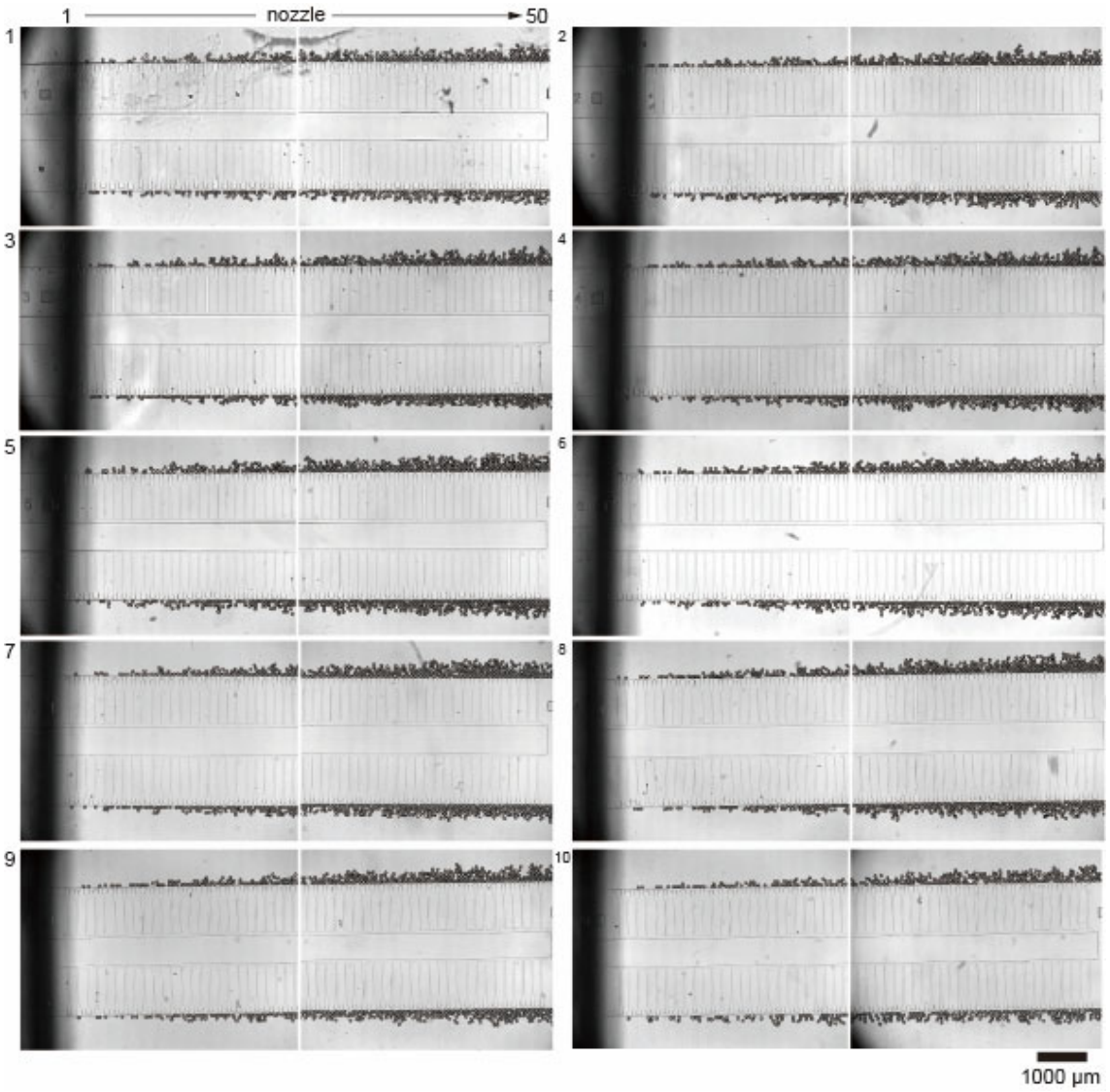

Fig. 6.8 Droplet formation in the ten modules at Q_d = 3.0 mL/h and Q_c = 50.0 mL/h.

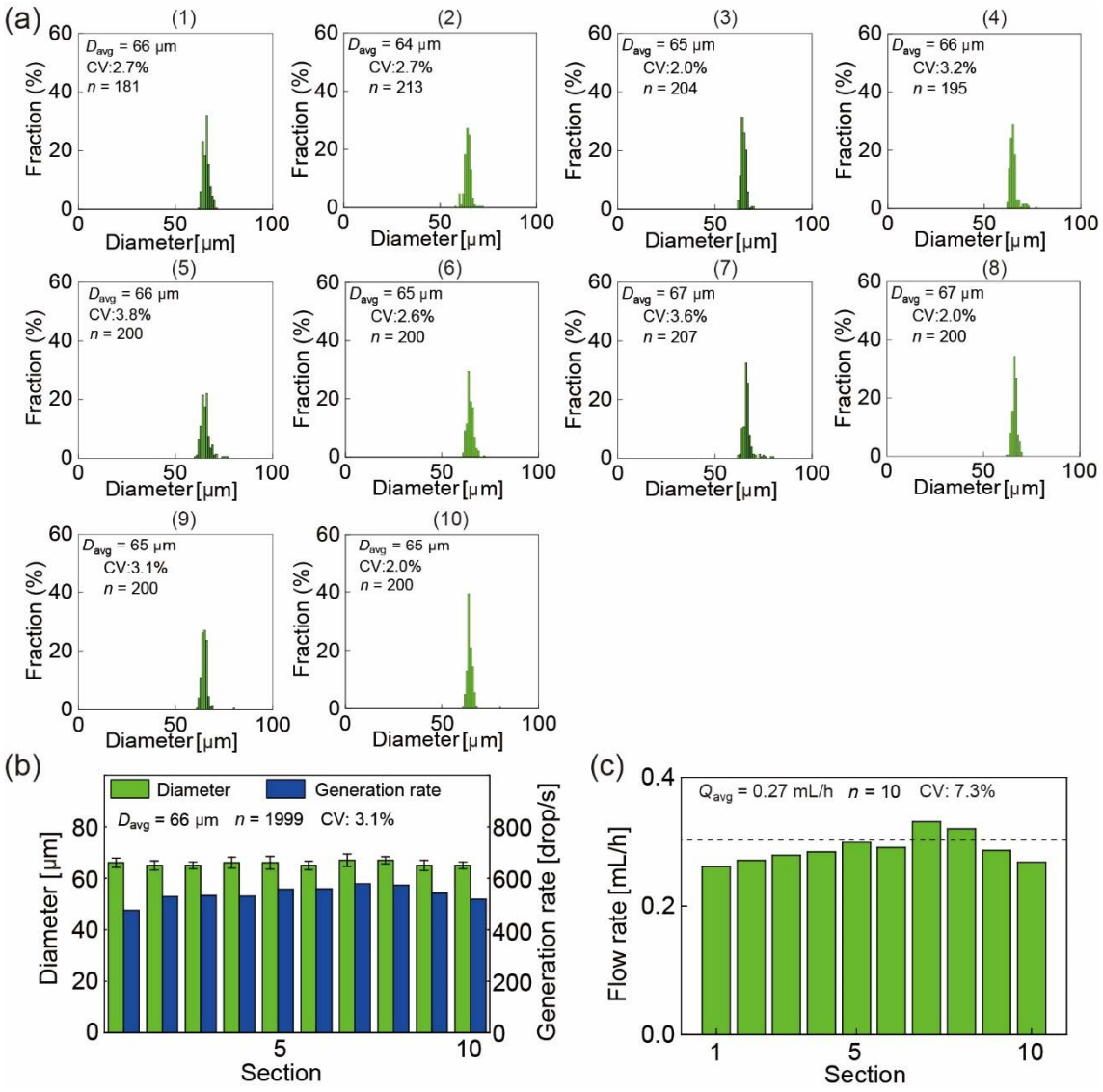

Fig. 6.9 (a) Size distribution of the main droplets across the ten modules. (b) Sizes and generation frequencies (*F*) of the main droplets. (c) Calculated flow rates of the dispersed phase in each module.

Satellite droplets were also observed and measured, with a mean diameter of 2.9 μm and a CV of 26.3% (**Fig. 6.10**).

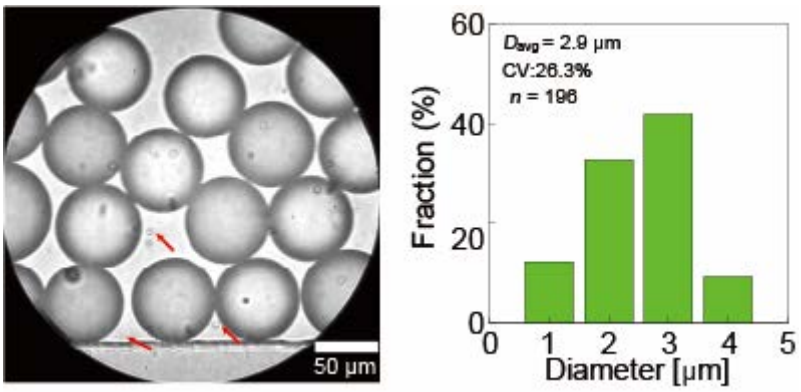

Fig. 6.10 Satellite droplets observed in the channel and their size distribution.

6.3.3 Separation of main and satellite droplets through DLD pillars

This section analyzes the movement of both main and satellite droplets through the parallel DLD regions, with a focus on how droplet size influences their migration. **Figure 6.11** shows the main droplets as they traverse the DLD arrays in 10 modules at flow rates of Q_c = 50.0 mL/h and Q_d = 3.0 mL/h. After the formation at the nozzles, the main droplets, averaging around 66 μm in diameter, mainly traveled along the central wall and entered the adjacent DLD region in each module. At these flow rates, there was minimal accumulation of droplets at the DLD entrance, and no deformation or coalescence was observed within the modules.

The main droplets started migrating towards the sidewall in displacement mode (**Figs. 6.11** and **6.12**), continuing slightly wider gaps (gaps 3–10) in the midstream region. Downstream the channels, they flowed across gaps 4–10 and into outlet-L. Roughly 60% of the droplets deviated from their expected path due to collisions with closely spaced droplets, similar to observations in **Chapter 2**. A small percentage (0.4%) of the main droplets passed through gaps 1–3 into outlet-S, while the majority (99.6%) followed the displacement mode as expected.

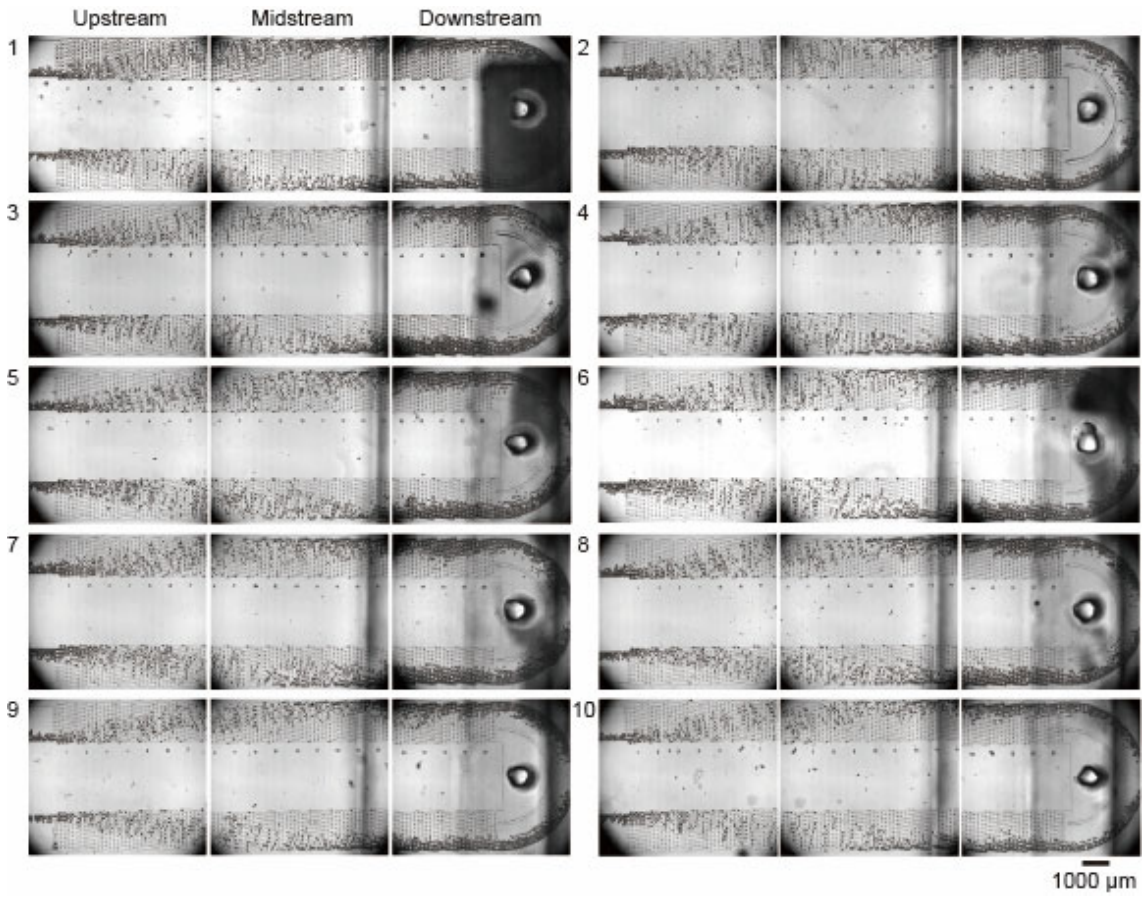

Fig. 6.11 Main droplets moving across the DLD arrays in displacement mode at Q_d = 3.0 mL/h and Q_c = 50.0 mL/h.

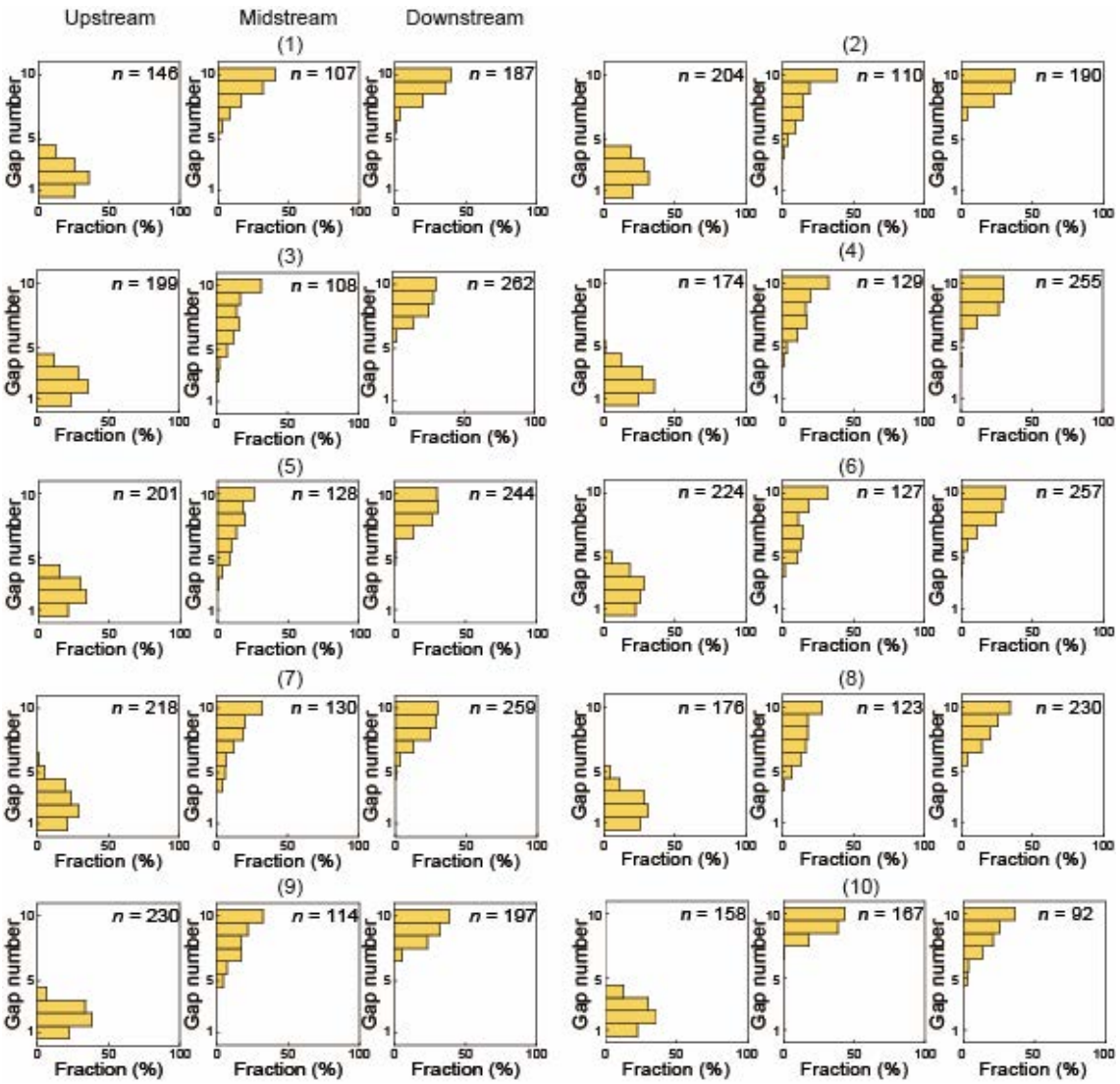

Fig. 6.12 Spatial distribution of droplets across the ten modules.

The satellite droplets within 10 DLD regions was also examined (**Fig. 6.13**). After flowing into the DLD region (gaps 1–2), the satellite droplets followed the flow in a zigzag path as they moved along the central wall in the midstream region. The satellite droplets continued this pattern through the downstream region and were collected at outlet-S.

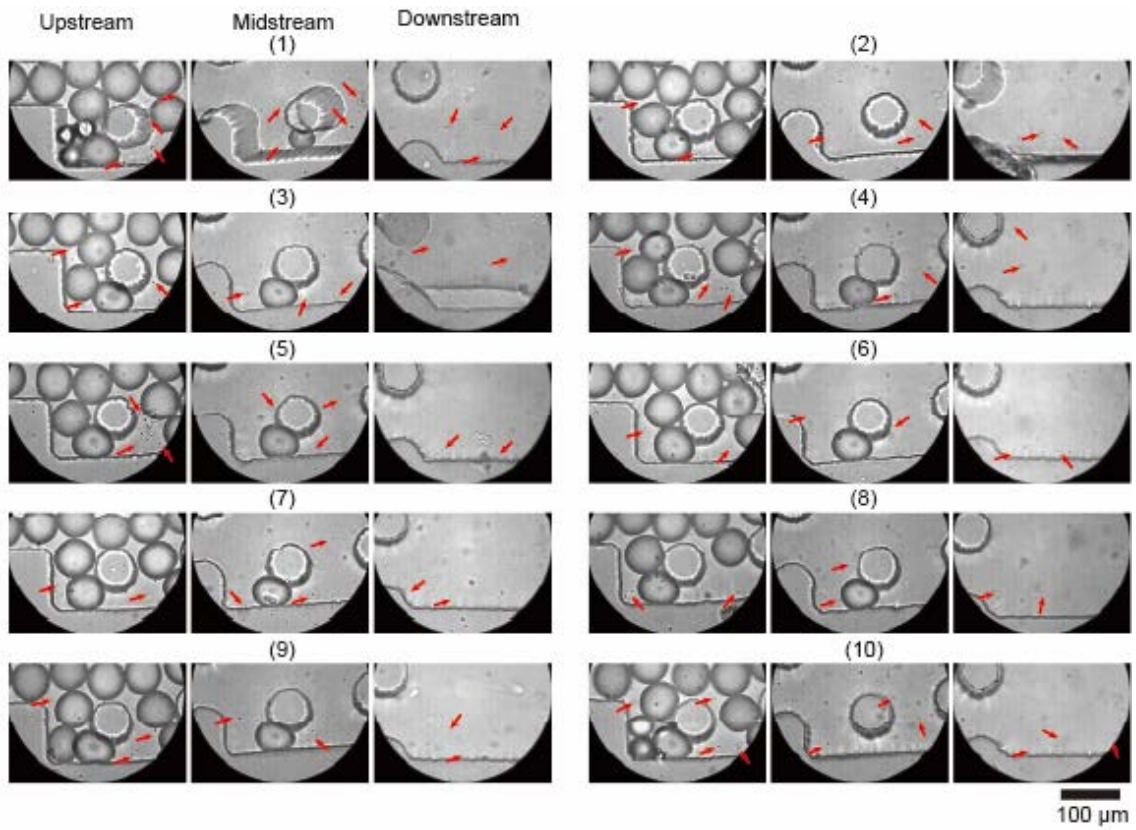

Fig. 6.13 Satellite droplets moving through the DLD gaps in ten modules at Q_d = 3.0 mL/h and Q_c = 50.0 mL/h.

After separating the main and satellite droplets, their sizes were measured at the outlets of all modules (**Figs. 6.14** and **6.15a**). The main droplets had a mean diameter of 66 μm with a CV of 2.2%, meeting earlier measurements (**Fig. 6.15b**). Similarly, the satellite droplets had a mean diameter of 2.8 μm with a CV of 25.8%, matching prior measurements (**Fig. 6.15c**). These findings confirm the successful separation in all modules, achieving 100% purity of the main droplets with minimal volume loss. In this parallel array configuration with DLD pillars, the satellite droplets (diameter < D_c) followed a distinct pathway, allowing for efficient separation and a high throughput of 3.0 mL/h.

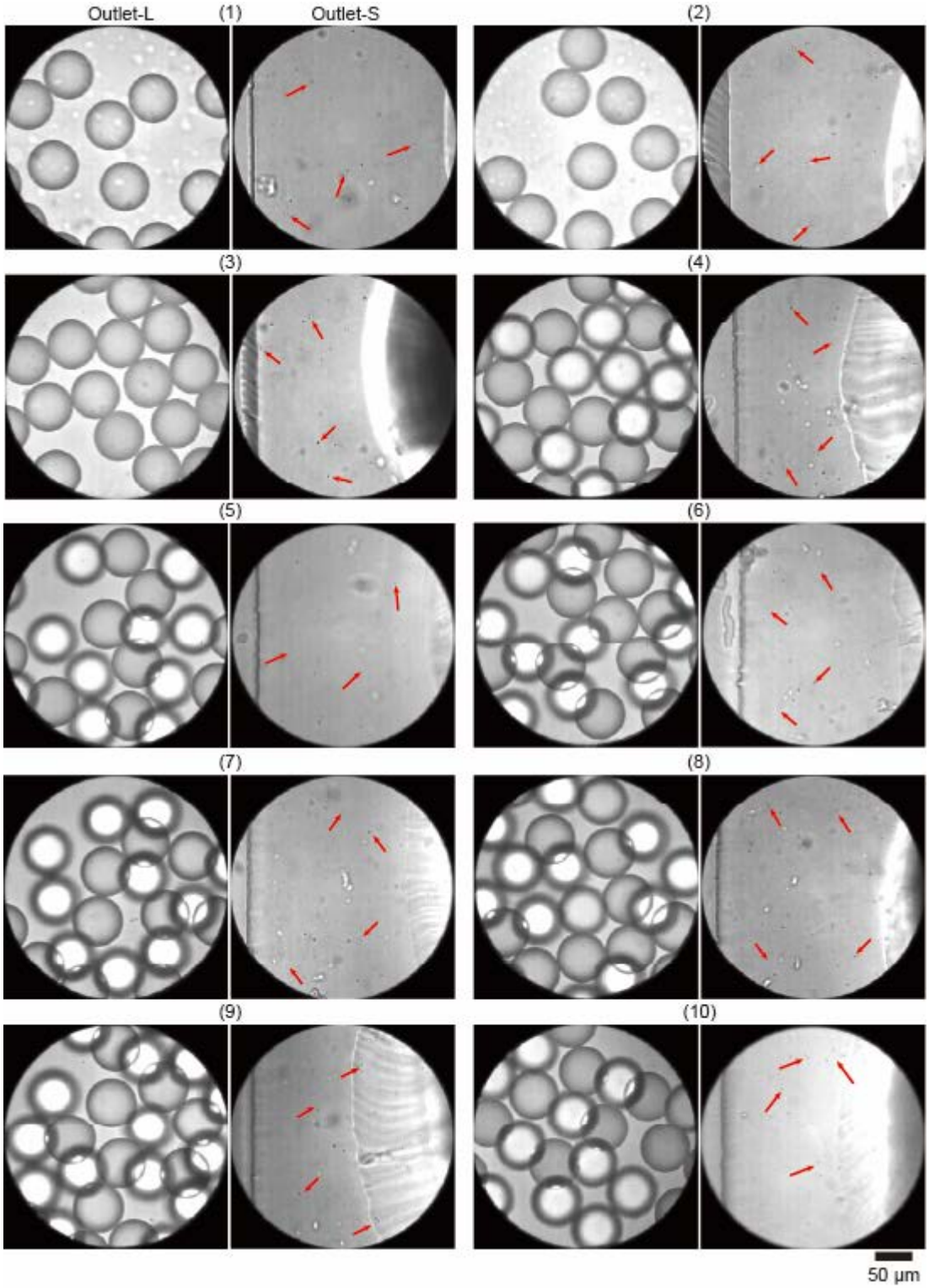

Fig. 6.14 DLD-separated droplets near the two outlet reservoirs in the ten modules. Satellite droplets are indicated by red arrows.

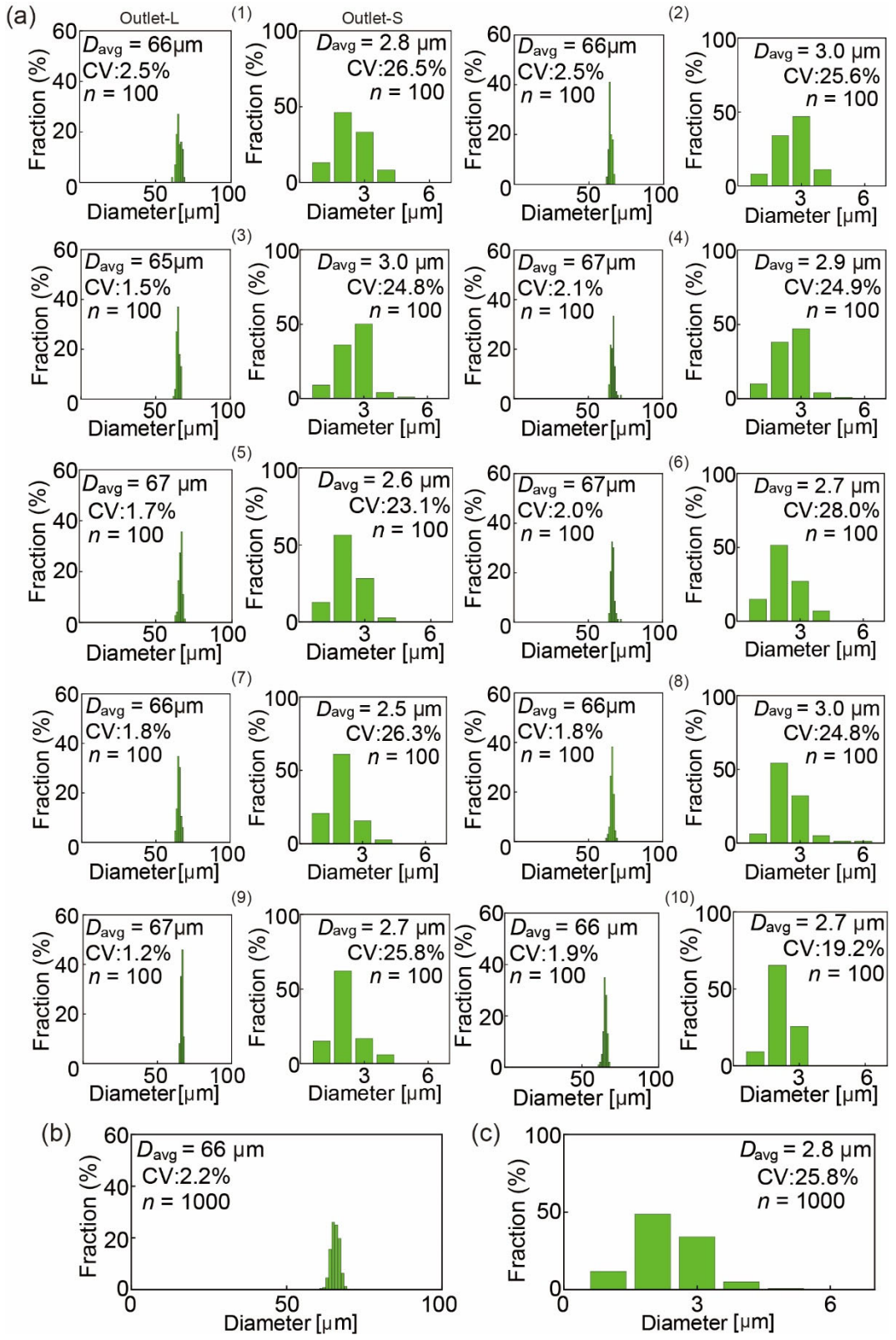

Fig. 6.15 (a) Main droplets flowing into outlet-L and their size distributions in each module. (b) Size distribution of the collected main droplets. (c) Size distribution of the collected satellite droplets.

This chapter represents an improved device over previous designs by expanding from a single module with 60 step-emulsification nozzles and a DLD array to a system with 1,000 step-emulsification nozzles arranged in parallel. This enhancement significantly increased the droplet generation rate to 5,395 drops per second and achieved a throughput of 3.0 mL/h, compared to the 408 drops per second and 0.2 mL/h in the single-module configuration. This new design increased throughput volume by 15 times compared to earlier studies using the same materials. In addition, the throughput of this study (3.0 mL/h) was greatly increased compared with the satellite-free droplets via integration of shear-driven method and DLD in single module (0.05 mL/h) and 8 parallel modules (0.2 mL/h) (**Table 6-7**). Furthermore, the step emulsification process, which is resilient to flow rate fluctuations, allowed parallelization of a greater number of nozzles within a single module and enabled the inclusion of more modules within the same device footprint (76 mm × 52 mm).

Table 6-7 DLD-based droplet production

Droplet formation	Parallelization	Throughput (mL/h)	Production
Shear-driven method	1	0.05	Satellite-free main droplets
	8	0.2	
Step emulsification	60	0.2	
	1000	3.0	
Step emulsification	60	1.3	Main droplets

Despite the higher throughput of satellite-free droplets, a small fraction (0.4%) of the main droplets deviated from the intended path due to droplet collisions. Two strategies are suggested to address this issue. First, enlarging the bifurcated channels could enhance the recovery of main droplets that do not fully displace. Second, a higher DLD array may reduce droplet density, minimizing deviations caused by collisions. Implementing these changes could improve the device's performance and broaden its applications for various droplet manipulation tasks.

Unlike the large-scale designs focused on producing mass quantities of droplets, this device is specifically designed for the mass-production of satellite-free droplets. While monodispersity of the main droplets is comparable to designs ignoring satellite droplets, the throughput of this device is currently lower. However, throughput could be induced by adding

more nozzles and modules within a larger footprint. Stacking or parallelizing multiple devices offers a promising strategy for high-throughput production of satellite-free droplets.

6.4 Conclusion

This research presented a new method to improve the generation and yield of satellite-free droplets by utilizing a parallel configuration that integrates step emulsification with Deterministic Lateral Displacement (DLD) for droplet formation and separation. By incorporating inlet reservoirs in the top layer, a consistent fluid supply was maintained, allowing uniform droplet generation across all ten modules. The DLD arrays effectively separated monodisperse main droplets, which had an average diameter of around 66 μm, a coefficient of variation (CV) of 2.2%, 100% purity, and a recovery rate of 99.6%. This approach increased the production rate to 3.0 mL/h, significantly higher than the 0.2 mL/h achieved with a single-module device. The high yield and purity achieved through this method highlight its potential for large-scale industrial applications that demand the production of satellite-free droplets.

References

[1] H. H. Jeong, D. Issadore, D. Lee. Recent developments in scale-up of microfluidic emulsion generation via parallelization. *Korean J. Chem. Eng.*, **2016**, 33, 1757–1766.

[2] J. Wu, S. Yadavali, D. Lee, D. A. Issadore. Scaling up the throughput of microfluidic droplet-based materials synthesis: A review of recent progress and outlook. *Appl. Phys. Rev.*, **2021**, 8, 031304.

[3] L. Ma, X. Zhao, J. Hou, L. Huang, Y. Yao, Z. Ding, J. Wei, N. Hao. Droplet microfluidic devices: working principles, fabrication methods, and scale-up applications. *Small Methods*, **2023**, 2301406.

[4] Z. Shi, X. Lai, C. Sun, X. Zhang, L. Zhang, Z. Pu, D. Li. Step emulsification in microfluidic droplet generation: mechanisms and structures. *Chem. Comm*., **2020**, 56, 9056–9066.

[5] Z. Liu, C. Duan, S. Jiang, C. Zhu, Y. Ma, T. Fu. Microfluidic step emulsification techniques based on spontaneous transformation mechanism: A review. *J. Ind. and Eng. Chem*., **2020**, 92, 18–40.

[6] T. Kawakatsu, H. Komori, M. Nakajima, Y. Kikuchi, T. Yonemoto. Production of monodispersed oil-in-water emulsion using crossflow-type silicon microchannel plate. *J. Chem. Eng. Jpn.*, **1999**, 32, 241–244.

[7] I. Kobayashi, Y. Wada, K. Uemura, M. Nakajima. Microchannel emulsification for mass production of uniform fine droplets: integration of microchannel arrays on a chip. *Microfluid. Nanofluidics*, **2010**, 8, 255–262.

[8] I. Kobayashi, M. A. Neves, Y. Wada, K. Uemura, M. Nakajima. Large microchannel emulsification device for producing monodisperse fine droplets. *Procedia Food Sci.*, **2011**, 1, 109–115.

[9] I. Kobayashi, S. Mukataka, M. Nakajima. Novel asymmetric through-hole array microfabricated on a silicon plate for formulating monodisperse emulsions. *Langmuir*, **2005**, 21, 7629–7632.

[10] I. Kobayashi, S. Mukataka, M. Nakajima. Production of monodisperse oil-in-water

emulsions using a large silicon straight-through microchannel plate. *Ind. Eng. Chem. Res.*, **2005**, 44, 5852–5856.

[11] C. Zheng, S. Masui, Y. Kanno, T. Nisisako. Microfluidic step emulsification with parallel nozzles on a vertical slit. *Ind. Eng. Chem. Res.*, **2024**, 63, 10226–10233.

[12] A. Ofner, D. G. Moore, P. A. Rühs, P. Schwendimann, M. Eggersdorfer, E. Amstad, D. A. Weitz, A. R. Studart. High-throughput step emulsification for the production of functional materials using a glass microfluidic device. *Macromol. Chemi. Phys.*, **2017**, 218, 1600472.

[13] S. Sugiura, M. Nakajima, K. Yamamoto, S. Iwamoto, T. Oda, M. Satake, M. Seki. Preparation characteristics of water-in-oil-in-water multiple emulsions using microchannel emulsification. *J. Colloid Interface Sci.*, **2004**, 270, 221–228.

[14] T. Kuroiwa, H. Takada, A. Shogen, K. Saito, I. Kobayashi, K. Uemura, A. Kanazawa. Cross-linkable chitosan-based hydrogel microbeads with pH-responsive adsorption properties for organic dyes prepared using size-tunable microchannel emulsification technique. *Colloid Surf. A: Physicochem. Eng. Asp.*, **2017**, 514, 69–78.

[15] A. M. Chuah, T. Kuroiwa, I. Kobayashi, X. Zhang, M. Nakajima. Preparation of uniformly sized alginate microspheres using the novel combined methods of microchannel emulsification and external gelation. *Colloid Surf. A: Physicochem. Eng. Asp.*, 2009, 351, 9–17.

[16] T. Nisisako, T. Torii, T. Higuchi. Separation of satellite droplets using branch microchannel configuration. *Proc. Micro Total Anal. Syst.* **2004**, 2, 312–314.

[17] C. H. Yang, Y. S. Lin, K. S. Huang, Y. C. Huang, E. C. Wang, J. Y. Jhong, C. Y. Kuo. Microfluidic emulsification and sorting assisted preparation of monodisperse chitosan microparticles. *Lab Chip*, **2009**, 9, 145–150.

[18] Y. C. Tan, A. P. Lee. Microfluidic separation of satellite droplets as the basis of a monodispersed micron and submicron emulsification system. *Lab Chip*, **2005**, 5, 1178–1183.

[19] N. Tottori, T. Hatsuzawa, T. Nisisako. Separation of main and satellite droplets in a deterministic lateral displacement microfluidic device. *RSC adv.*, **2017**, 7, 35516–35524.

[20] N. Tottori, T. Nisisako. High-throughput production of satellite-free droplets through a parallelized microfluidic deterministic lateral displacement device. *Sen. Actuators B:*

Chemical, **2018**, 260, 918–926.

Chapter 7
Conclusion and outlook

7.1 Conclusion

In this thesis, a series of microfluidic devices were developed, integrating step emulsification and deterministic lateral displacement (DLD) to improve droplet production and separation. The key outcomes from each chapter are summarized below:

Chapter 1: Introduction

This chapter provided an overview of microfluidic methods for droplet formation and particle separation, particularly focusing on step emulsification and DLD. The chapter also outlined the objectives, and structure of the thesis, leading into the subsequent chapters.

Chapter 2: Separation of main and satellite droplets

A novel microfluidic device integrating step emulsification and DLD was demonstrated for the production of satellite-free droplets. Monodisperse droplets were formed via 60 parallel step emulsification nozzles, and satellite droplets were successfully separated with 100% purity using the DLD micropillar array. Key conclusions include:

(1) Monodisperse droplets with a mean diameter of 58 μm and a coefficient of variation (CV) of 2.8% were generated at dispersed phase flow rates of 0.2 mL/h or less, without coalescence.

(2) The DLD array achieved 100% purity in separating main droplets from satellite droplets.

Chapter 3: Post-formation fluorescent labeling of main droplets

The device described in **Chapter 2** was adapted for the advanced processing of post-formation fluorescent labeling of satellite-free droplets by introducing fluorescent nanoparticles into the droplet stream. The main droplets, formed via step emulsification,

were successfully modified by the nanoparticles, and the final polymerized microspheres exhibited fluorescence. Key conclusions include:

(1) Stable production of monodisperse droplets (mean diameter: 50 μm, CV: 3.9%) was achieved even in the presence of fluorescent nanoparticles.

(2) By controlling the flow rates of the nanoparticle-containing nanoparticle stream and the continuous phase, modified droplets were collected via outlet L, while satellite droplets and excess nanoparticles were removed via outlet S.

(3) The precursor droplets and the photopolymerized microspheres (mean diameter 47 μm, CV: 3.9%) exhibited fluorescence, confirming successful modification.

Chapter 4: In-situ external gelation for alginate hydrogel particle synthesis

The step emulsification and DLD system was used for the advanced processing of alginate hydrogel particles. Na-alginate droplets were formed at the step emulsification nozzles and underwent emulsion-based external gelation within the DLD array, resulting in Ca-alginate hydrogels. Key conclusions include:

(1) Na-alginate droplets (mean diameter: 68 μm, CV: 8.5%) were formed at the step emulsification nozzles in a jetting regime.

(2) Ca-alginate hydrogel particles were successfully formed and collected via outlet L, although the gelation process was incomplete.

(3) The final hydrogel particles had a mean diameter of 66 μm with a CV of 25.3%, indicating that the gelation was insufficient for uniform particle formation.

Chapter 5: Mitigation of droplet accumulation through pillar-assisted nozzle design

To address the issue of droplet accumulation near the ends of the step emulsification nozzles, a new design was proposed. The step emulsification array (100 parallel nozzles) was coupled with a DLD array, allowing the immediate lateral migration of droplets upon formation. A second design with stair-like arranged micropillars was also tested to distribute droplets over a wider area. Key conclusions include:

(1) Stable droplet formation was observed with the step emulsification nozzles integrated into the DLD array.

(2) No droplet accumulation near the nozzles was observed, as droplets migrated laterally away immediately after formation.

(3) The stair-like micropillar arrangement resulted in varied droplet migration distances, but droplets near the ends of the DLD array were carried along by the flow, as confirmed by 3D fluid flow simulations.

Chapter 6: Scalable droplet processing via module parallelization

To increase production efficiency, a device with 10 modules of step emulsification nozzles and DLD arrays was developed. The device featured two layers, with the upper layer managing fluid distribution and the lower layer housing the modules for droplet formation and separation. Key conclusions include:

(1) 3D fluid flow simulations confirmed the uniform distribution of liquid across the 10 modules.

(2) Monodisperse droplet formation and satellite droplet separation were achieved in all 10 modules, with main droplets having a mean diameter of 66 μm and a CV of 2.2%.

(3) The throughput of satellite-free droplets was increased to 3.0 mL/h, significantly higher than the output (0.2 mL/h) reported in **Chapter 2**.

7.2 Outlook

The results of this thesis demonstrate the successful integration of step emulsification and DLD for the production and separation of satellite-free droplets and microparticles. The designs introduced in this work offer potential for scaling up droplet-based microfluidic processes with high throughput and purity. However, several areas for further research and development remain.

(1) Processing of smaller droplets

In **Chapters 2** and **6**, satellite droplets with an average diameter of ~3 μm and a CV over 20% were observed. These satellite droplets could be collected as smaller droplets. Their sizes can be further reduced by using step emulsification nozzles with smaller heights (e.g., 1 μm). Additionally, employing multiple DLD arrays[1] could improve the monodispersity of collected droplets by sorting them based on size.

(2) Highly spherical and monodisperse alginate hydrogels

In **Chapter 4**, alginate hydrogel microparticles with large size distribution due to the insufficient gelation were produced. This issue can be improved by using more stable ionic emulsions. In addition, compared with the production using flow-focusing channel and DLD proposed by Tottori et al.[2], the contact between Na-alginate droplets forming at different nozzles resulted in coalescence. The design proposed in **Chapter 5**, which eliminated the droplet contact immediately after formation, can be used to solve the coalescence issue.

(3) Mass-production of particles

As demonstrated in **Chapter 3** and **4**, the coupling of step emulsification and DLD enables the production of fluorescent microspheres and alginate hydrogels. This approach can also be adapted to the device presented in **Chapter 6**. By adding an inlet chamber to introduce a liquid containing fluorescent nanoparticles or ionic emulsions, mass production

of fluorescent microspheres and alginate hydrogels could be achieved. Moreover, other functional materials, such as magnetic-responsive particles, could be produced using similar techniques.

(4) Improvement of droplet accumulation

In **Chapter 5**, two designs for improving the accumulation of droplets near the sidewall without nozzle array were proposed. Both of the designs are expected to tune the streamlines to be parallel with the sidewall, which carry the droplets out of the microchannel without flowing back to the nozzle array.

(5) Mass-production of satellite-free droplets

As described in **Chapter 6**, a microfluidic device with 10 modules was developed, achieving a throughput of 3.0 mL/h. However, the number of modules can be further increased to enhance yield. For instance, the number of parallel modules on a larger footprint or stacking multiple layers of parallel modules could significantly increase the throughput.

(6) Double emulsions

Double emulsions can be produced by using two step emulsification stages. As shown in previous studies, emulsions formed in the first step are directed to the second for further processing[3,4]. The devices described in **Chapters 2** and **6** could be modified to integrate an additional step emulsification and DLD system for the production of satellite-free double emulsions.

(7) Fluorescent and magnetic responsive hydrogel particles

Previous studies have reported the production of fluorescent and magnetic-responsive hydrogel particles in microchannels[5]. Building on the devices introduced in **Chapters 3** and **4**, the production of such particles could be achieved by integrating $CaCl_2$-based external gelation with surface coating techniques using fluorescent and Fe_3O_4 nanoparticles within a DLD array.

(8) Production of functional particles

In **Chapter 3**, fluorescent microspheres were produced involving via the coalescence of fluorescent nanoparticles and the monomer droplets while the droplets crossed the nanoparticle stream. Crossing the reagent and material streams in DLD can be further used to produce particles like surface modified microgels and drug-loaded droplets[5].

(9) Device optimization

In comparison to the device described in **Chapter 2**, which had 10 columns of micropillars in the DLD section, the device in **Chapter 5** featured only 5 columns, resulting in shorter device length for the same displacement distances of large droplets. The DLD array can be optimized further to enable efficient separation with a reduced device footprint. Additionally, reducing the pitch between adjacent step emulsification nozzles could increase the number of parallel nozzles, thereby improving throughput for mass production.

This research lays the groundwork for advanced microfluidic systems capable of producing high-quality, satellite-free droplets and particles, with significant potential in both academic and industrial settings.

References

[1] N. Tottori, T. Hatsuzawa, T. Nisisako. Separation of main and satellite droplets in a deterministic lateral displacement microfluidic device. *RSC adv.*, **2017**, 7, 35516–35524.

[2] N. Tottori, Y. Liu, T. Nisisako. Functional particles design using deterministic lateral displacement. *Proc. Micro Total Anal. Syst.* **2018**, 4, 2181–2182.

[3] A. Ofner, I. Mattich, M. Hagander, A. Dutto, H. Seybold, P. A. Rühs, A. R. Studart. Controlled massive encapsulation via tandem step emulsification in glass. *Adv. Funct. Mater.*, **2019**, 29, 1806821.

[4] M. L. Eggersdorfer, W. Zheng, S. Nawar, C. Mercandetti, A. Ofner, I. Leibacher, S. Koehler, D. A. Weitz. Tandem emulsification for high-throughput production of double emulsions. *Lab Chip*, **2017**, 17, 936–942.

[5] Y. Liu. Microfluidic emulsion-based synthesis of functional calcium-alginate hydrogel particles and their application. Tokyo Institute of Technology, **2022**.

Appendix

A.1 Microfabrication

A.1.1 Polydimethylsiloxane (PDMS) chip

The fabrication process of the PDMS device was depicted in detail in **Fig. A.1**.

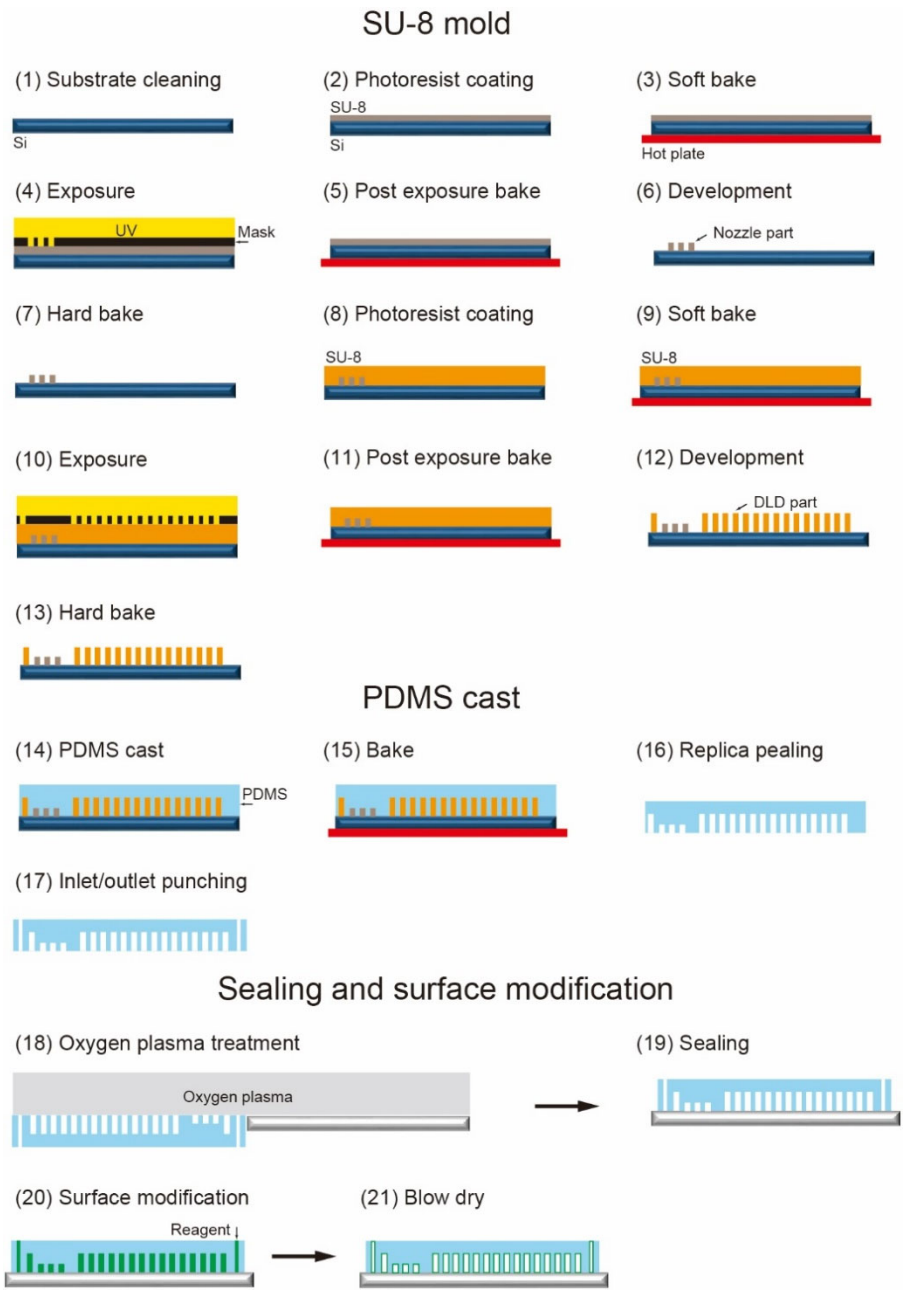

Fig. A.1 Schematic illustration of PDMS device fabrication.

(1) Substrate cleaning

The silicon wafer was washed serially with acetone (> 99%; Fujifilm Wako Pure Chemical, Osaka, Japan), ethanol (> 99.5%; Fujifilm Wako Pure Chemical, Osaka, Japan), and pure water by an ultrasonic machine (2510; Branson, MO, USA) for 5 min. After that, the wafer was dried on the hot plate.

(2) Photoresist coating

A negative photoresist SU-8 (Nippon Chemical Industrial, Tokyo, Japan) was homogeneously coated on the silicon wafer by spin coater (MS-B100; Mikasa, Tokyo, Japan) for the fabrication of the step emulsification nozzles. The types of the SU-8 used in each chapter and parameters of spin coating are shown in **Table A-1**. For a better adhesion between the photo-mask and silicon wafer during the exposure process, the photoresist around the wafer edge was manually removed.

Table A-1 Parameters of the spin coating.

Chapter	SU-8	Rotation speed (rpm)	Time (s)
2 3	3025	4500	30
4	3025	3000	30
5	3005	450	40
6	3005	350	40

(3) Soft bake

To evaporate the extra solvent, the silicon wafer was put on the hot plate at 65 ℃ for around 1 min and 95 ℃ for around 3 min. The entire heating process must be kept shielded from light. After that, the silicon wafer was cooled down to room temperature.

(4) Exposure

The silicon wafer coated with SU-8 photoresist and the film mask (thickness: 0.175 mm; resolution: 25400 dpi; Unno Giken, Tokyo, Japan) taped on a glass plate are fixed on the mask aligner (MA-10; Misaka) for the UV exposure with total energy around 200 mJ/cm^2.

(5) Post exposure bake

The silicon wafer was put on the hot baker at 65 ℃ for around 1 min and 95 ℃ for around 5 min after UV exposure.

(6) Development

The silicon wafer was soaked in the SU-8 developer (Nippon Chemical Industrial) and waved manually for 5 min. The isopropyl alcohol (Fujifilm Wako Pure Chemical, Osaka, Japan) is used to clean the extra SU-8 developer on the wafer.

(7) Hard bake

The wafer was put on the hot plate at 150 ℃ for around 20 min for hardening.

(8) Photoresist coating

The negative photoresist SU-8 was coated on the silicon wafer with 1st SU-8 layer for the fabrication of the DLD part and the other channels. The types of the SU-8 used in each chapter and parameters of spin coating are shown in **Table A-2**.

Table A-2 Parameters of the spin coating

Chapter	SU-8	Rotation speed (rpm)	Time (s)
2 3	3050	1200	30
4	3050	1600	30
5	3050	1400	30
6	3050	1600	30

(9) Soft bake

The silicon wafer was put on the hot plate at 65 ℃ for around 5 min and 95 ℃ for around 45 min. The entire heating process must be kept shielded from light. After that, the silicon wafer was cooled down to room temperature.

(10) Exposure

The same step as (4) was implemented.

(11) Post exposure bake

The same step as (5) was implemented.

(12) Development

The silicon wafer was soaked in the SU-8 developer and waved manually for 15 min. The isopropyl alcohol is used to clean the extra SU-8 developer on the wafer.

(13) Hard bake

The same step as (7) was implemented.

(14) PDMS cast

The PDMS base (SILPOT 184 Silicon Elastomer Base; DuPont Toray Specialty Materials K.K., Tokyo, Japan) and curing agent (SILPOT 184 Silicon Elastomer Curing agent; DuPont Toray Specialty Materials K.K.) are mixed manually at the ratio of 10:1 w/w. The mixture is put inside the vacuum desiccator (MVD-100; AS-ONE, Osaka, Japan) until no bubble was observed. Then, the PDMS mixture is poured onto the SU-8 mold taped in a plastic petri dish.

(15) Bake

The petri dish containing the SU-8 mold and the PDMS liquid was put on the hot plate at 80 ℃ for 1 hour for curing.

(16) Replica pealing

The hard PDMS layer can be manually peeled from the SU-8 mold. The useless part (containing no micro-patterns) could be easily cut out.

(17) Inlet/outlet punching

The holes for the inlets and outlets were opened using a punch tool (diameter of 1 mm; BPP-10F; Kai Industries, Gifu, Japan).

(18) Oxygen plasma treatment

The oxygen plasma treatment was used to achieve an irreversible bonding between the PDMS chip and the slide glass (S1111 for **Chapters 2**, **3**, **4**, and **5**; S9111 for **Chapter 6**; Matsunami Glass, Osaka, Japan). The PDMS chip and the slide glass were treated by the oxygen plasma using the plasma equipment (for devices of **Chapters 2** and **3**; BP-1; Samco Inc., Kyoto, Japan; for devices of **Chapters 5** and **6**s PDC-32Gs Harrick Plasma, NY, USA). The conditions of the treatment including the PDMS-PDMS sealing of **Chapters 4** and **6** are shown in **Table A-3**.

Table A-3 The conditions of plasma treatment.

Equipment	BP-1	PDC-32G
Power (W)	20	18
Chamber pressure (Torr)	1	0.3
Time (s)	30	40 (PDMS-Glass) 60 (PDMS-PDMS)

(19) Sealing

The treated PDMS replica and slide glass were assembled together manually.

(20) Hydrophilic modification

Immediately after the sealing, the hydrophilic reagent (SPRA 202; Tokyo Ohka Kogyo, Kanagawa, Japan) contained in a syringe (1001 TLL, Hamilton Company, NV, USA) was infused manually into the device. After the channels were filled with the reagent, the surfaces were treated for 1 min. Then, pure water was infused by the same syringe to remove the extra reagent.

(21) Blow dry

The air was infused into the devices by the same syringe as (20) to remove the rinsing water.

A.1.2 Acrylic mold

Four rectangular acrylic blocks (5 mm × 60 mm × 3 mm) were cut from an acrylic board by a laser processing machine (Epilog Fusion Pro 36; Tokyo, Japan). These acrylic blocks were taped on the bottom of a plastic petri dish to cast the PDMS chip for the upper part of **Chapter 6**.

A.2 Chemicals

A.2.1 Washing liquids

Aceton (>99%; Fujifilm Wako Pure Chemical, Osaka, Japan), and ethanol (>99.5%; Fujifilm Wako Pure Chemical) were used to wash the silicon substrate and the produced polymeric microspheres.

A.2.2 Droplet/particle formation

(1) Continuous phase

An aqueous polyvinyl alcohol (PVA; GL-03; *M*w ~ 20000 g/mol; 87–89% hydrolyzed; Mitsubishi Chemical, Tokyo, Japan) having a viscosity of 1.75 mPa·s and a density of 1.00 g/cm^3 was used as the continuous phase of **Chapters 2**, **3**, **5**, and **6**. An oleic acid (Fujifilm Wako Pure Chemical) added by a surfactant (1 wt%; SY-Glyster CRS-75; Sakamoto Yakuhin Kogyo, Osaka, Japan) was used as the continuous phase of **Chapter 4**.

(2) Dispersed phase

A 1,6-hexanediol diacrylate (HDDA; Shin-Nakamura Kagaku, Tokyo, Japan) added by 2-hydroxy-2-methylpropiophenone (Darocur 1173; BASF, Tokyo, Japan) with a fraction of 1 wt% was used as the dispersed phase of **Chapters 2** and **3**. The pure HDDA was used as the dispersed phase of **Chapter 6**. A corn oil (Fujifilm Wako Pure Chemical) was used as the dispersed phase of **Chapter 5**. A 3 wt% aqueous Na-alginate (Fujifilm Wako Pure Chemical) solution was prepared as the dispersed phase of **Chapter 4**.

(3) Other phase

A 2 wt% aqueous PVA solution containing the fluorescent nanoparticles (0.06 wt%; #24051-10; 300 nm; Polysciences, PA, USA) was used to prepare fluorescent HDDA droplets of **Chapter 3**. A 30 wt% aqueous $CaCl_2$ (Fujifilm Wako Pure Chemical) solution, and the oleic acid added by the surfactant (0.1 wt%; SY-Glyster CRS-75) were mixed with a ratio of 5:14 w/w as the emulsion for the gelation of Ca-alginate of **Chapter 4**. An 80 wt%

aqueous glycerol (Fujifilm Wako Pure Chemical) solution was used for the solution exchange of **Chapter 4**.

A.3 Peripheral equipment

A.3.1 Experimental setup

Syringes filled with the liquids were driven by the syringe pumps (KDS 210; KDS Legato 180; and KDS Legato 200; KD Scientific Inc., PA, USA). The microfluidic device was fixed on the holder of an invert optical microscope (IX-73, Olympus, Tokyo, Japan). A high-speed video camera (FASTCAM mini ax50; Photron, Tokyo, Japan) was combined for flow observation (**Fig. A.2**).

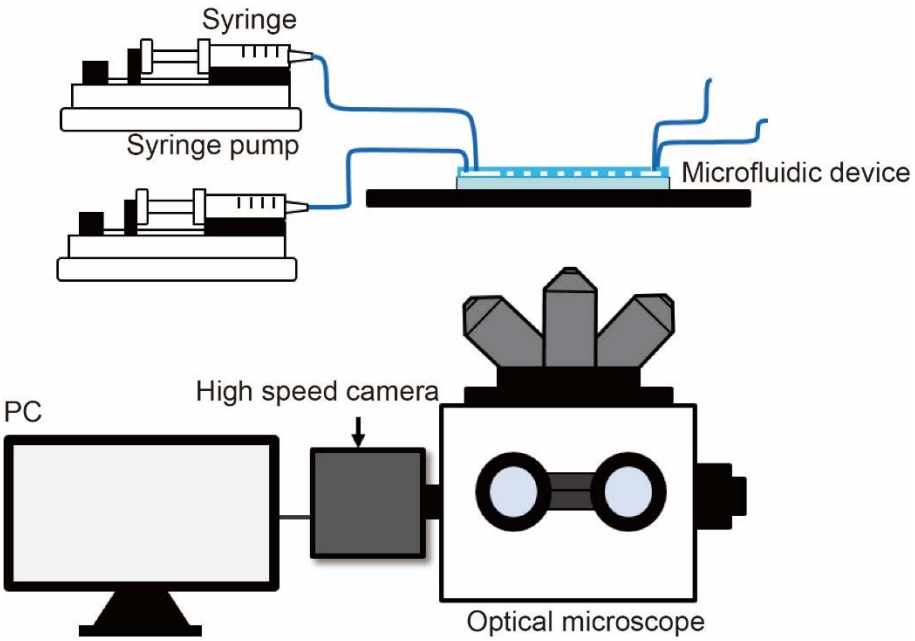

Fig. A.2 Schematic illustration of an experimental setup.

A.3.2 Peripheral equipment of microchannel

Polyethylene tubes (0.5 mm i.d., 1.0 mm o.d.; Hibiki #3; Kunii, Tokyo, Japan) were used for introducing and collecting liquids in all experiments. In particular, Teflon tube (0.5 mm i.d., 1.59 mm o.d; FLON Industry, Tokyo, Japan) linking the syringe through a connector (screw size: No. 1/4-28UNF; FLON Industry, Tokyo, Japan) was used for introducing the aqueous Na-alginate solution in **Chapter 4**.

A.3.3 Fluid infusion system

(1) Syringes and needle

Gastight glass syringe (1750 TLL, 1001 TLL, and 1010TLL; Hamilton Company, NV, USA) and disposal syringes (SS-50ESZ; Terumo, Tokyo, Japan), and needle (SNA-22G-C; Musashi Engineering, Tokyo, Japan) for connecting the tubes were used (**Fig. A.3)**.

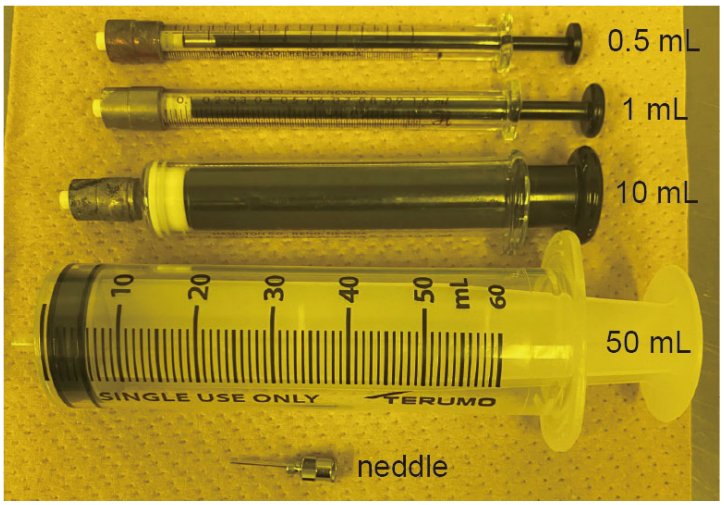

Fig. A.3 Syringe used in this thesis.

(2) Syringe pump

Syringe pumps (KDS 210; KDS Legato 180; and KDS Legato 200; KD Scientific Inc., PA, USA) were used to infuse the fluid. The specifications are shown in **Table A-4**.

Table A-4 The specifications of syringe pumps.

	KDS 200	KDS Legato 180	KDS Legato 200
Pump type	Push	Push	Push
Syringes	10 μl ~ 140 ml	0.5 μl ~ 10 ml	0.5 μl ~ 140 ml
Dimensions	28×23×14 cm	22.6×19.05×15 cm	16.51×25.4×27.94 cm
Weight	4 kg	2.66 kg	4.9 kg
Linear force	18 kg	13.6 kg	34 kg
Max. step rate	1600 /sec	26 μsec/μstep	26 μsec/μstep
Min. step rate	1 /100 secs	27.5 sec/μstep	27.5 sec/μstep
Max. pusher travel rate		71.55 mm/min	190.80 mm/min
Min. pusher travel rate		0.02 μm/min	0.36 μm/min
Advance per microstep	0.165 μm (1/16 step)		
Accuracy	±1 %	±0.35 %	±0.35 %
Reproducibility	±0.1 %	±0.05 %	±0.05 %

A.3.4 Observation system

(1) Optical microscope

An invert optical microscope (IX-73, Olympus, Tokyo, Japan) was used for observation (**Fig. A.4**). A light source (TH4-100, Olympus) and a mercury burner (BH2-RFL-T3, Olympus) were used for the observation under bright field and fluorescent field, respectively.

(2) High-speed camera

A high-speed video camera (Fastcam Mini AX50, Photron, Tokyo, Japan) was mounted on the optical microscope for flow observation.

(3) Laser scanning confocal microscope

A Laser scanning confocal microscope (LSCM; LSM780; Carl Zeiss Microscopy, Jena, Germany) at Open Facility Center (Institute of Science Tokyo) was used for the observation of the inner side of the fluorescence precursor droplets in **Chapter 4** (**Fig. A.5**).

(4) Image process software

Software ImageJ (National Institute of Health, MD, USA) was used to calculate the sizes of droplets and particles. Below is the calculation process:

while taking the pictures, the resolution of the high-speed camera was set as 1024×1024, and the pixel size is 20 μm × 20 μm. So, the actual length L (μm) of each pixel is according to the equation:

$$L = 20/(0.5 \times a) \tag{A-1}$$

0.5 is the ratio of adapter between the high-speed camera and microscope, a is the magnification of microscope lens.

Fig. A.4 Invert Optical microscope (IX-73, Olympus).

Fig. A.5 Laser scanning confocal microscope (LSM780, Carl Zeiss Microscopy) [1].

A.3.5 Other equipment

(1) Mechanical homogenizer

The reactant $CaCl_2$ emulsion in **Chapter 5** was prepared by a homogenizer (T10 basic ULTRA-TURRAX; IKA, Germany, **Fig. A.6**) at 30000 rpm for 3 min.

Fig. A.6 Mechanical homogenizer (T10 basic ULTRA-TURRAX).

(3) Filtration system

A glass mesh holder (Glass Type KG-25, ADVANTEC, Japan, **Fig. A.7**) was assembled with a nylon mesh (42 μm × 42 μm; Tokyo Screen, Tokyo, Japan) to separate microspheres in **Chapters 2** and **4**.

Fig. A.7 Glass mesh holder (Glass Type KG-25, ADVANTEC)

(5) Contact angle meter

The surface tension between two immiscible liquids was measured by a contact angle meter (B100; Asumi Giken, Tokyo, Japan, **Fig. A. 8**).

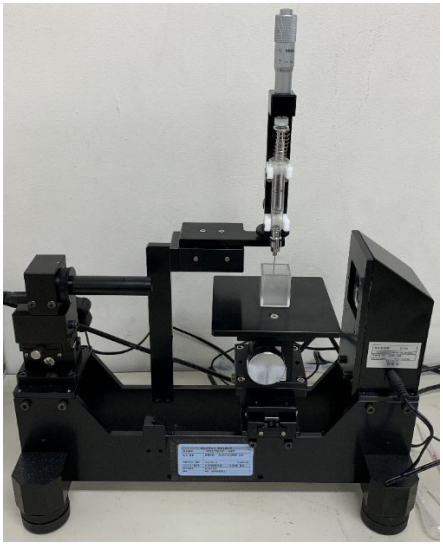

Fig. A. 8 Contact angle meter (B100, Asumi Giken)

(5) Scanning electron microscope

Scanning electron microscope (**Fig. A.9**; FlexSEM 1000; Hitachi High-Tech, Tokyo, Japan) at Open Facility Center (Institute of Science Tokyo) was used to observe the device and dried polymeric microspheres.

Fig. A.9 Scanning electron microscope (FlexSEM 1000, Hitachi High-Tech)

(7) Plasma kit

Two plasma equipment were used for the sealing (**Fig. A.10**; Left; BP-1; Samco Inc.; Right; PDC-32G; Harrick Plasma).

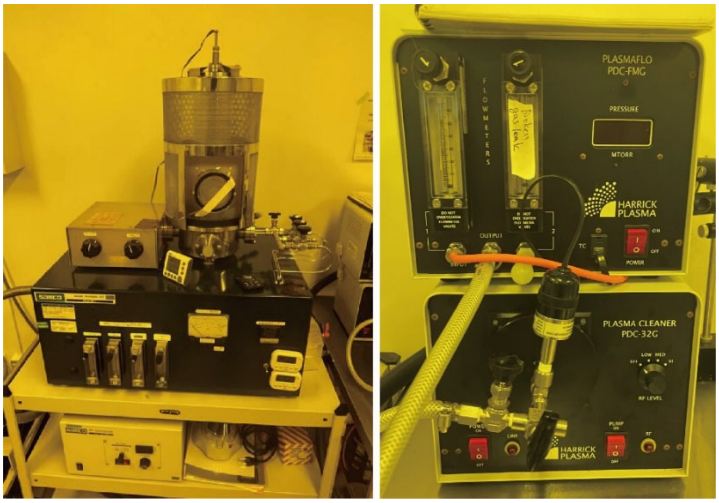

Fig. A.10 Equipment for oxygen plasma treatment (Left; BP-1, Samco Inc.; Right; PDC-32G).

(8) Height meter

The heights of the step emulsification nozzles and the main channels were measured by a 3D profilometer (**Fig. A.11a**; Dektak 150; Veeco, NY, USA) at Open Facility Center (Institute of Science Tokyo). A laser microscope (**Fig. A.11b**; VKX 3000; Keyence, Osaka, Japan) at Open Facility Center (Institute of Science Tokyo) was used to profile the step emulsification nozzles.

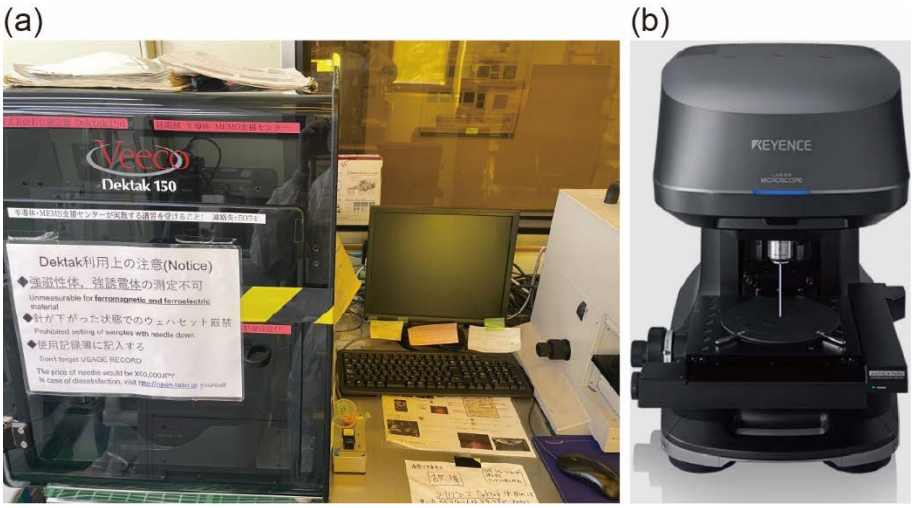

Fig. A.11 Equipment for height measurement (a) 3D profilometer (Dektak 150, Veeco). (b) A laser microscope (VKX 3000, Keyence)[2].

References

[1] Center for Integrative Biosciences, Institute of Science Tokyo.

https://www.cib.bio.titech.ac.jp/en/facilities/bioimaging-room/, September, **2024**.

[2] KEYENCE.

https://www.keyence.co.jp/, September, **2024**.

Acknowledgments

Completing a Ph.D. is a journey filled with challenges, opportunities for growth, and moments of immense learning. It is a culmination of years of dedication, perseverance, and the collective support of countless individuals. As I reach the end of this campus life, I would like to express my heartfelt gratitude to those who have played pivotal roles in making this achievement possible.

First and foremost, I am deeply indebted to my supervisor, professor Takasi Nisisako. Your guidance, wisdom, and unwavering support have been instrumental in shaping not only my research but also my approach to problem-solving and scientific inquiry. Your insightful feedback, encouragement, and patience during the most challenging periods of my research have been invaluable. You constantly pushed me to think critically and work rigorously, and for that, I am immensely grateful.

I would also like to extend my sincere thanks to Assistant Professor Yusuke Kanno. Your constructive criticism and thoughtful suggestions significantly enhanced the quality of my work. The time and effort you dedicated to reviewing my thesis have been crucial in helping me improve my work.

A special mention goes to my senior colleagues in the lab, Dr. Naotomo Tottori, Dr. Siyuan Xu, and Dr. Yingzhe Liu, and Dr. Shuzo Masui. Your expertise, patience, and willingness to share your knowledge made a significant impact on my research. Whether it was troubleshooting experiments, offering insightful advice, or simply encouraging me during challenging times, your mentorship played a crucial role in my development as a researcher. I am incredibly fortunate to have learned from you and will always be grateful for the time and effort you dedicated to helping me succeed.

I would also like to acknowledge the support from Open Facility of Institute of Science Tokyo for the design and processing.

Additionally, I would like to express my deep gratitude to the professors who offered invaluable advice and guidance during the preparation of this thesis and presentation:

Institute of Science Tokyo, Institute of Integrated Research, Prof. Kazuhiro Yoshida.

Institute of Science Tokyo, Institute of Integrated Research, Prof. Tadahiko Shinshi.

Institute of Science Tokyo, Institute of Integrated Research, Prof. Yasuko Yanagida.

Acknowledgments

Institute of Science Tokyo, Institute of Integrated Research, Assoc. Prof. Tadashi Ishida.

I also want to thank all the students of Nisisako lab for their help in daily life.

I would like to show my special thanks to my beloved parents. Your accompanies, consideration, patience, and confidence provided me with tremendous strength, supporting me completing over 20-year-journey in campus.

October 2024

Yokohama, Kanagawa, Japan

季 広沖（Guangchong JI）氏

業績調書

(2024 年 10 月 15 日現在)

1. 本博士論文に関連する業績

査読付学術論文（掲載済 2 編）

1) **Guangchong Ji**, Yusuke Kanno, and Takasi Nisisako, Microfluidic coupling of step emulsification and deterministic lateral displacement for producing satellite-free droplets and particles, ***Micromachines*** **14**, 622 (2023). **【第 2 章】**

2) **Guangchong Ji**, Shuzo Masui, Yusuke Kanno, and Takasi Nisisako, Upscaled production of satellite-free droplets: step emulsification with deterministic lateral displacement, ***Micromachines*** **15**, 908 (2024). **【第 6 章】**

国際学会発表（2 件）

1) ○**Guangchong Ji**, Yusuke Kanno, and Takasi Nisisako, Microfluidic synthesis of polymer particles using step emulsification and deterministic lateral displacement, *19th International Conference on Precision Engineering (ICPE2022)*, C086, Nara, Japan, November 28–December 2, 2022. (口頭発表，査読有) **【第 2 章】**

2) ○**Guangchong Ji**, Yusuke Kanno, and Takasi Nisisako, Synthesis of functional polymeric microspheres via step emulsification and deterministic lateral displacement, *26th International Conference on Miniaturized Systems for Chemistry and Life Sciences (MicroTAS2022)*, Hangzhou, China, October 23–27, 2022. (ポスター発表, 査読有) **【第 3 章】**

国内学会発表（3 件）

1) ○**Guangchong Ji**, Yusuke Kanno, and Takasi Nisisako, Inhibition of droplet clustering in step emulsification using deterministic lateral displacement, 2023 年度精密工学会春季大会学術講演会，東京, March 14–16, 2023. (口頭発表，査読なし) **【第 5 章】**

2) ○**Guangchong Ji**, Yusuke Kanno, and Takasi Nisisako, Microfluidic step emulsification and deterministic lateral displacement, 2022 年度精密工学会春季大会学術講演会，東京, March 15–17, 2022. (口頭発表，査読なし) **【第 2 章】**

3) ○**Guangchong Ji**, Yusuke Kanno, and Takasi Nisisako, On-chip production of alginate hydrogel microparticles using step emulsification and deterministic lateral displacement, 化学とマイクロ・ナノシステム学会 第 47 回研究会 (CHEMINAS 47), 1P38, p. 39, 東北大学川内キャンパス, 5/13–14, 2023. (ポスター発表，査読なし) **【第 4 章】**

研究助成

1) 2023 April, Cross the border! Tokyo Tech Pioneering Doctoral Research Project: Research Funds, 200,000 円.

2) 2022 April, Cross the border! Tokyo Tech Pioneering Doctoral Research Project: Research Funds, 400,000 円.

3) 2021 September, Cross the border! Tokyo Tech Pioneering Doctoral Research Project: Research Funds, 200,000 円.

2. 本博士論文に関連しない業績

修士論文

Guangchong Ji, Separation of lactic acid bacteria from commercially produced yogurt using a micropillar array, 東京工業大学機械系機械コース，2020 年 9 月

国際学会発表（2 件）

1) ○Yeyi Tang, **Guangchong Ji**, Yusuke Kanno, and Takasi Nisisako, Evaluating particle separation in a 3D-printed deterministic lateral displacement device, The 10th International Conference of Asian Society for Precision Engineering and Nanotechnology (ASPEN2023), p. 95, Hong Kong, November 21–24, 2023.

2) ○**Guangchong Ji**, Naotomo Tottori, and Takasi Nisisako, Lactic acid bacteria of different shapes flowing through deterministic lateral displacement microarrays, *The 18th International Conference on Precision Engineering (ICPE2020)*, G-1-3, November 24–26, 2020.（口頭，査読付）

国内学会発表（6 件，口頭，査読無）

1) ○Yeyi Tang, **Guangchong Ji**, Yusuke Kanno, and Takasi Nisisako, Formation and separation of large droplets in a 3D-printed microfluidic device，化学とマイクロ・ナノシステム学会第 47 回研究会（CHEMINS 47）, 1P36, p. 37，東北大学川内キャンパス，5/13–14 (2023).

2) ○Yeyi Tang, **Guangchong Ji**, Yusuke Kanno, and Takasi Nisisako, A 3D-printed microfluidic device for integrated droplet generation and sorting，2023 年度精密工学会春季大会学術講演, F06, pp. 593–594, 東京理科大学葛飾キャンパス, 3/14–16 (2023).

3) ○Chunqi Zheng, **Guangchong Ji**, Shuzo Masui, Yusuke Kanno, and Takasi Nisisako, Microfluidic step emulsification via parallel nozzles crossing a slit，2023 年度精密工学会春季大会学術講演会, F09, pp. 597–598，東京理科大学葛飾キャンパス，3/14–16

(2023).

4) ○**Guangchong Ji**, Naotomo Tottori, Takasi Nisisako, Deterministic lateral displacement separation of lactic acid bacteria from yogurt sample after vortexing, 2020 年度精密工学会春季大会学術講演会, C10, pp.159–160, 東京農工大学（東京）, 3/17–19 (2020).

5) ○**Guangchong Ji**, Naotomo Tottori, Takasi Nisisako, Isolation of lactic acid bacteria from yogurt using a deterministic lateral displacement array, 化学とマイクロ・ナノシステム学会第 40 回研究会, 4P22, p.176, アクトシティ浜松（浜松）, 11/19–21 (2019).

6) ○**Guangchong Ji**, Naotomo Tottori, Takasi Nisisako, Separation of lactic acid bacteria from yogurt through deterministic lateral displacement micropillar arrays, 2019 年度精密工学会秋季大会学術講演会, G32, pp. 294–295, 静岡大学浜松キャンパス（浜松）, 9/4–6 (2019).

以上